

ATOMISTIC SIMULATIONS ON THE INTERFACE BONDING BETWEEN  
ALUMINUM AND SILICON SURFACES

by

Levent Inci

A Thesis

Submitted to the Faculty of Graduate Studies and Research  
through Engineering Materials  
in Partial Fulfillment of the Requirements for  
the Degree of Master of Applied Science at the  
University of Windsor

Windsor, Ontario, Canada

2006

© 2006 Levent Inci



Library and  
Archives Canada

Bibliothèque et  
Archives Canada

Published Heritage  
Branch

Direction du  
Patrimoine de l'édition

395 Wellington Street  
Ottawa ON K1A 0N4  
Canada

395, rue Wellington  
Ottawa ON K1A 0N4  
Canada

*Your file* *Votre référence*  
*ISBN: 978-0-494-35960-0*  
*Our file* *Notre référence*  
*ISBN: 978-0-494-35960-0*

**NOTICE:**

The author has granted a non-exclusive license allowing Library and Archives Canada to reproduce, publish, archive, preserve, conserve, communicate to the public by telecommunication or on the Internet, loan, distribute and sell theses worldwide, for commercial or non-commercial purposes, in microform, paper, electronic and/or any other formats.

The author retains copyright ownership and moral rights in this thesis. Neither the thesis nor substantial extracts from it may be printed or otherwise reproduced without the author's permission.

**AVIS:**

L'auteur a accordé une licence non exclusive permettant à la Bibliothèque et Archives Canada de reproduire, publier, archiver, sauvegarder, conserver, transmettre au public par télécommunication ou par l'Internet, prêter, distribuer et vendre des thèses partout dans le monde, à des fins commerciales ou autres, sur support microforme, papier, électronique et/ou autres formats.

L'auteur conserve la propriété du droit d'auteur et des droits moraux qui protègent cette thèse. Ni la thèse ni des extraits substantiels de celle-ci ne doivent être imprimés ou autrement reproduits sans son autorisation.

---

In compliance with the Canadian Privacy Act some supporting forms may have been removed from this thesis.

Conformément à la loi canadienne sur la protection de la vie privée, quelques formulaires secondaires ont été enlevés de cette thèse.

While these forms may be included in the document page count, their removal does not represent any loss of content from the thesis.

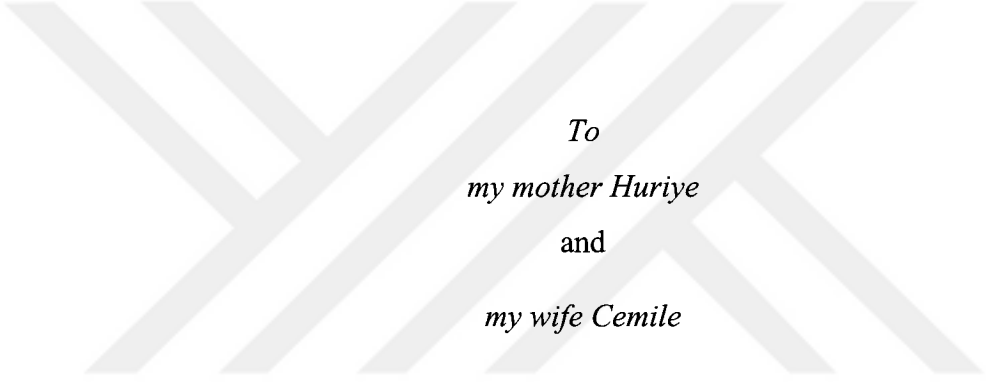
Bien que ces formulaires aient inclus dans la pagination, il n'y aura aucun contenu manquant.

  
**Canada**

## ABSTRACT

Although the near-surface deformation behaviour of Al-Si alloys is generally thought to depend on the characteristics of the interface between Al (matrix) and Si (second phase), little is known about its specific deformation and debonding mechanisms. In this study, molecular-dynamics (MD) simulations with the modified embedded atom method (MEAM) potential were utilized to investigate the Al-Si interfaces during room-temperature plastic deformation.

MD simulations were carried out on a three-dimensional Al-Si interface model using about  $1 \times 10^4$  atoms. The evolution of the subsurface microstructure of Al-Si system was investigated to develop a constitutive stress-strain relationship. A characteristic stick-slip behaviour was observed. Without vacancies, dislocations, and mechanical defects, the interfacial failure occurred over a finite strain increment and the interface failed at 8GPa stress with the strain of 14%. The results demonstrated that MEAM predictions were consistent with the finite element method predictions, at normalized small stress values the correlation is acceptable (%20).



*To  
my mother Huriye  
and  
my wife Cemile*

## ACKNOWLEDGEMENTS

This work would not have been possible without the support and encouragement of Dr. A. Alpas and Dr. V. Stoilov, for this I am very grateful. I would also like to thank the Department of MAME and my supervisors for financial support throughout my studies. Finally, thanks also to the members of our research group, especially to Erkan, whose friendship and interest have made this task enjoyable.



## TABLE OF CONTENTS

ABSTRACT.....	iii
DEDICATION.....	iv
ACKNOWLEDGEMENTS.....	v
LIST OF TABLES.....	viii
LIST OF FIGURES.....	ix
LIST OF SYMBOLS.....	xiii
LIST OF ABBREVIATIONS.....	xvi
<b>CHAPTER</b>	
<b>I. INTRODUCTION</b>	
1.1 Why Aluminum Silicon Alloys?.....	1
1.2 Focus of Research.....	2
1.3 Modeling the Interface.....	3
1.3.1 Molecular Dynamics.....	5
1.3.2 Density Functional Theory.....	7
1.3.3 Embedded Atom Method (EAM), Modified Embedded Atom Method (MEAM).....	8
1.4 Scope of this Thesis.....	9
<b>II. AL-SI INTERFACE</b>	
2.1 Introduction.....	10
2.2 Experimental Studies.....	12
2.3 Computer Simulations.....	15
<b>III. MOLECULAR DYNAMICS</b>	
3.1 Introduction.....	20
3.2 Interaction Potential.....	26
3.3 Integration Methods.....	28
3.3.1 Verlet Algorithm.....	29
3.4 Periodic Boundary Conditions and Cut off Radius.....	30
3.5 Neighbour List.....	32

<b>IV.</b>	<b>THE MODIFIED EMBEDDED ATOM METHOD</b>	
4.1	General Formulation of Embedded Atom Method (EAM).....	33
4.2	General Formulation of the Modified Embedded Atom Method (MEAM).....	37
<b>V.</b>	<b>PREVIOUS WORK</b>	
5.1	Introduction.....	43
5.2	Atomistic Simulations on the Tensile Debonding of an Aluminum–Silicon Interface .....	44
5.3	An Analysis of Decohesion along an Imperfect Interface .....	57
<b>VI.</b>	<b>SIMULATION</b>	
6.1	Introduction.....	64
6.2	Computational Aspects and MEAM Implementation.....	64
6.2.1	Setting Geometry .....	67
6.2.2	Program Organization .....	70
6.3	Al-Si Interface and Parameters .....	73
<b>VII.</b>	<b>RESULTS AND DISCUSSIONS</b>	
7.1	EAM Results .....	77
7.2	MEAM Results .....	82
<b>VIII.</b>	<b>CONCLUSIONS AND FUTURE WORK</b>	
8.1	Conclusions.....	91
8.2	Future Work .....	92
<b>APPENDICES</b>		
	The derivation of the forces.....	94
<b>REFERENCES.....</b>		<b>101</b>
<b>VITA AUCTORIS .....</b>		<b>105</b>

## LIST OF TABLES

TABLE 3.1 ESTABLISHED CONCEPTS FOR POTENTIAL ENERGY FUNCTIONS .....	28
TABLE 4.1 QUANTITIES USED FOR DETERMINATION OF THE FUNCTIONS $F(\rho)$ AND $Z(r)$ FOR Ni AND Pd, AND THEIR FITTED VALUES. LATTICE CONSTANT $A_0$ IN $\text{\AA}^0$ ; ELASTIC CONSTANTS $C_{11}$ , $C_{12}$ AND $C_{44}$ IN $10^{12}$ DYN/CM <sup>2</sup> ; SUBLIMATION ENERGY $E_s$ IN eV; VACANCY FORMATION ENERGY $E_{1V}^F$ IN eV; AND THE ENERGY DIFFERENCE BETWEEN BCC AND FCC PHASES IN eV [12].....	36
TABLE 6.1 AL AND SI PARAMETERS .....	76
TABLE 7.1 THE INPUT VALUES FOR THE FIRST SIMULATION (STRESSES ARE APPLIED TO THE TOP WALL) .....	77
TABLE 7.2 DIMENSIONAL VALUES OF INPUTS.....	78
TABLE 7.3 INFORMATION FOR THE SYSTEM (CURRENT TIME, KINETIC ENERGY, NUMBER OF ATOMS) AT TIMES DETERMINED BY STEP AVG.....	79
TABLE 7.4 THE INPUT VALUES FOR THE SECOND SIMULATION (STRESSES ARE APPLIED TO THE TOP WALL) .....	80
TABLE 7.5 INFORMATION FOR THE SYSTEM (CURRENT TIME, KINETIC ENERGY, NUMBER OF ATOMS) AT TIMES DETERMINED BY STEP AVG.....	82

## LIST OF FIGURES

<b>FIG. 1.1</b> VOID AND CRACK NUCLEATION AROUND THE SILICON PARTICLES UNDER THE CONTACT SURFACE (POLISHED, UNETCHED) [2] .....	3
<b>FIG. 1.2</b> SCHEMATIC DIAGRAM OF HOW SIMULATIONS WORK. ....	5
<b>FIG. 2.1</b> THE RELAXED STRUCTURE (TOTAL ENERGY MINIMIZED THROUGH A STATIC SIMULATION AT 0 K) OF THE ALUMINUM-SILICON INTERFACE WHERE $[100]_{\text{Si}} \parallel [100]_{\text{Al}}$ . THE MODEL IS PERIODIC IN THE $[010]$ AND $[001]$ DIRECTIONS, THE VIEWING DIRECTION IS THE (A) $[001]$ DIRECTION AND THE (B) $[100]$ DIRECTION [16].....	11
<b>FIG. 2.2</b> VOID AND CRACK NUCLEATION AROUND THE SILICON PARTICLES UNDER THE CONTACT SURFACE AND ON THE SURFACE (POLISHED, UNETCHED)[2]. ....	15
<b>FIG. 2.3</b> SCANNING ELECTRON MICROSCOPE (SEM) IMAGES OF THE FRACTURE SURFACE OF A CAST A356-T6 AL ALLOY SUBJECTED TO CYCLIC LOADING CONDITIONS. THE IMAGES DEMONSTRATE THAT PURE SILICON INCLUSIONS ARE OBSERVED TO BOTH (A) FRACTURE AND (B) DEBOND [28]. ....	17
<b>FIG. 2.4</b> XFEM SIMULATIONS OF CRACK PROPAGATION IN AL-SI: (A) NUCLEATION OF THE CRACK, (B) EVOLUTION OF THE CRACK[37].....	18
<b>FIG. 3.1</b> SCHEMATIC DIAGRAM OF A BASIC MD CODE. ....	22
<b>FIG. 3.2</b> TWO DIMENSIONAL VIEW OF A MD SIMULATIONS CELL USING PERIODIC BOUNDARY CONDITIONS. ....	31
<b>FIG. 3.3</b> CUTOFF RADIUS AND VERLET RADIUS FOR VERLET NEIGHBOUR LIST .....	32
<b>FIG. 4.1</b> ELLIPSE GEOMETRY FOR CALCULATING SCREENING PARAMETER, $S_{JK}$ . ....	41
<b>FIG. 5.1</b> REPRESENTATIVE AVERAGE-STRESS VERSUS TRUE-STRAIN RESPONSE OF THE $[100]_{\text{Si}} \parallel [100]_{\text{Al}}$ INTERFACE MODEL TO BOUNDARY VELOCITIES, $v_1$ , AT THE FAR ENDS	

OF THE BLOCKS IN THE [100] AND [-100] DIRECTIONS. THE MODEL IS PERIODIC IN THE [010] AND [001] DIRECTIONS [16].....	47
<b>FIG. 5.2</b> THE AVERAGE-STRESS VERSUS TRUE-STRAIN RESPONSE OF THE [100] <sub>Si</sub>   [100] <sub>Al</sub> INTERFACE MODEL UNDER VARIOUS CONDITIONS. THE MODEL IS PERIODIC IN THE [010] AND [001] DIRECTIONS [16].....	48
<b>FIG. 5.3</b> THE AVERAGE-STRESS VERSUS TRUE-STRAIN RESPONSE OF THE [100] <sub>Si</sub>   [100] <sub>Al</sub> INTERFACE MODEL COMPARED TO PURE SILICON AND ALUMINUM MEAM MODELS WITH THE SAME DIMENSIONS LOADED UNDER IDENTICAL CONDITIONS. ALL THREE MODELS ARE PERIODIC IN THE [010] AND [001] DIRECTIONS [16]..	49
<b>FIG. 5.4</b> (A) AVERAGE-STRESS VERSUS TRUE-STRAIN; (B) AVERAGE-STRESS VERSUS FAR-FIELD DISPLACEMENT; AND (C) AVERAGE-STRESS VERSUS LOCAL DISPLACEMENT FOR THE [100] <sub>Si</sub>   [100] <sub>Al</sub> INTERFACE MODEL FOR DIFFERENT LENGTHS IN THE [100] DIRECTION. THE MODEL IS PERIODIC IN THE [010] AND [001] DIRECTIONS [16]..	51
<b>FIG. 5.5</b> EFFECT OF AVERAGING VOLUME ON THE AVERAGE-STRESS VERSUS TRUE-STRAIN RESPONSE OF THE 80Å[100] <sub>Si</sub>   [100] <sub>Al</sub> INTERFACE MODEL. THE MODEL IS PERIODIC IN THE [010] AND [001] DIRECTIONS [16].....	53
<b>FIG. 5.6</b> STRESS DISTRIBUTION ALONG THE [100] DIRECTION FOR THE [100] <sub>Si</sub>   [100] <sub>Al</sub> INTERFACE MODEL. THE ATOMISTIC IMAGE CORRESPONDS DIRECTLY TO THE DIFFERENT POSITIONS INDICATED ALONG THE LOWER AXIS OF THE PLOT. THE MODEL IS PERIODIC IN THE [010] AND [001] DIRECTIONS AND THE STRESSES ARE AVERAGED IN THESE DIRECTIONS [16].....	56
<b>FIG. 5.7</b> (A) SCHEMATIC OF THE THREE DIFFERENT REFERENCE PLANES USED TO CALCULATE THE OPENING DISPLACEMENT IN THE MEAM SIMULATIONS. (B)	

TRACTION–DISPLACEMENT CURVES FOR THE 40Å MEAM MODEL AND DIFFERENT CONTINUUM-BASED COHESIVE LAWS [16].....	57
<b>FIG. 5.8</b> NORMAL TRACTION ACROSS THE INTERFACE AS A FUNCTION OF $U$ , WITH $U_c = 0$ FOR BOTH THE POLYNOMIAL POTENTIAL (5.5) AND THE EXPONENTIAL POTENTIAL (5.9) [34].....	61
<b>FIG. 5.9</b> STRESS-STRAIN CURVES FOR A PERFECT INTERFACE, $A/L = 0$ , FOR VARIOUS VALUES OF $L/\delta$ USING THE POLYNOMIAL POTENTIAL (5.5). THE REMAINING INTERFACE PARAMETERS AND THE MATERIAL PROPERTIES ARE SPECIFIED IN THE TEXT [34] .....	63
<b>FIG. 6.1</b> THE AL FCC STRUCTURE CREATED BY MATERIALS STUDIO SOFTWARE .....	68
<b>FIG. 6.2</b> THE SI DIAMOND STRUCTURE CREATED BY MATERIALS STUDIO SOFTWARE.....	68
<b>FIG. 6.3</b> DIFFERENT VIEWING DIRECTIONS OF AL-SI INTERFACE CREATED BY MATERIALS STUDIO SOFTWARE.....	69
<b>FIG. 6.4</b> FLOW CHART OF THE MAIN PROGRAM .....	70
<b>FIG. 6.5</b> FLOW CHART OF THE SINGLESTEP FUNCTION .....	72
<b>FIG. 6.6</b> AL-SI INTERFACE CREATED BY POW-RAY SOFTWARE .....	74
<b>FIG. 7.1</b> THE EVOLUTION OF THE ALSi INTERFACE UNDER NORMAL AND SHEAR STRESS APPLIED TO THE TOP WALL (40 Si AND 40 AL LAYERS) .....	78
<b>FIG. 7.2</b> THE EVOLUTION OF THE ALSi INTERFACE UNDER NORMAL AND SHEAR STRESS APPLIED TO THE TOP WALL (30 Si AND 40 AL LAYERS) .....	81
<b>FIG. 7.3</b> SPRING MODEL FOR MACROSCOPIC STICK SLIP .....	83
<b>FIG. 7.4</b> THE AVERAGED SHEAR STRESS AGAINST THE AVERAGED SHEAR STRAIN .....	85
<b>FIG. 7.5</b> THE STRESS-STRAIN RELATIONSHIPS WITHIN EACH OF THE AL, Si AND THE INTERFACE ALSi .....	86

**FIG. 7.6** THE FAR FIELD DISPLACEMENTS (AVERAGE DISPLACEMENT AT THE TOP 3 ATOMIC PLANES IN THE TOP SLAB) ..... 87

**FIG. 7.7** THE LOCAL DISPLACEMENTS (AVERAGE DISPLACEMENT AT  $\pm 3$  PLANES ATOMIC PLANES AT THE INTERFACE) ..... 88

**FIG. 7.8** COMPARISON OF THE MD SIMULATION RESULTS WITH THE FINITE ELEMENT METHOD RESULTS ..... 89



## LIST OF SYMBOLS

$a$	ACCELERATION
$B$	BULK MODULUS
$C_{ij}$	ELASTIC CONSTANTS
$D$	DIPOLE TENSOR VECTOR
$d$	AVERAGE DIAMETER
$E$	ENERGY
$E_s$	SUBLIMATION ENERGY
$E_c$	COHESIVE ENERGY
$E_v^F$	VACANCY FORMATION ENERGY
$E_{relax}$	LATTICE RELAXATION ENERGY
$f$	VOLUME FRACTION
$f_c$	CUTOFF FUNCTION
$F$	FORCE
$F_i$	EMBEDDING FUNCTION
$H$	HAMILTONIAN
$k_b$	BOLTZMAN CONSTANT
$K$	KINETIC ENERGY
$L$	LAGRANGIAN
$m$	MASS
$n$	A UNIT NORMAL VECTOR
$n_s$	NUMBER OF s ELECTRONS AT OUTER SHELL

$n_d$	NUMBER OF d ELECTRONS AT OUTER SHELL
$N$	NUMBER OF ATOMS
$q_j$	GENERALIZED COORDINATES
$\dot{q}_j$	GENERALIZED VELOCITIES
$P$	FRACTURE PROBABILITY
$p$	MOMENTUM
$r$	POSITION
$r_c$	CUTOFF RADIUS
$r_e$	NEAREST NEIGHBOUR DISTANCE
$r_v$	VERLET RADIUS
$S$	SCREENING FUNCTION
$t_i^{(j)}$	WEIGHT FACTORS FOR ATOMIC DENSITIES
$T$	TRACTION
$u$	DISPLACEMENT
$v$	VELOCITY
$V$	POTENTIAL ENERGY
$Z$	CHARGE OF THE ATOM
$Z_i$	NUMBER OF NEAREST NEIGHBOUR
$\beta$	DECAY FACTOS FOR ATOMIC DENSITIES
$\sigma$	STRESS
$\epsilon$	STRAIN
$\phi$	PAIR POTENTIAL
$\Omega$	ATOMIC VOLUME

$\rho$	ELECTRON DENSITY
$\nabla$	GRADIENT VECTOR OPERATOR
$\Delta t$	INFINITESIMAL TIME STEP



## LIST OF ABBREVIATIONS

DC	DIFRACTION CONTRAST
DFT	DENSITY FUNCTIONAL THEORY
EAM	EMBEDDED ATOM METHOD
EBSD	ELECTRON BACK-SCATTER DIFRACTION
FEM	FINITE ELEMENT METHOD
HR	HIGH RESOLUTION
MEAM	MODIFIED EMBEDDED ATOM METHOD
MC	MONTE CARLO
MD	MOLECULAR DYNAMICS
NMR	NUCLEAR MAGNETIC RESONANCE
NTV	CONSTANT NUMBER OF ATOMS, VOLUME AND TEMPERATURE
PBC	PERIODIC BOUNDARY CONDITIONS
SEM	SCANNING ELECTRON MICROSCOPE
TEM	TRANSMISSION ELECTRON MICROSCOPY
XFEM	EXTENDED FINITE ELEMENT METHOD

# CHAPTER I

## INTRODUCTION

Aluminum and its alloys are used in many industries to make millions of different products and are very important to the world economy. As a metal, aluminum is soft, which makes it easily machined and cast, lightweight, nontoxic and has excellent corrosion resistance and durability due to the protective oxide layer. Aluminum form alloys with many elements such as copper, zinc, magnesium, manganese and silicon. These aluminum alloys display a marked improvement in mechanical properties. Aluminum alloys are preferred in many critical components of the automobile and aircrafts industries due to their high strength to weight ratio.

In this chapter, aluminum silicon alloys, especially their interface and how to model them, are introduced and an overview of this thesis is given. Also some remarks are made about the molecular dynamics simulations and the way they are implemented

### 1.1 Why Aluminum Silicon Alloys?

Today, unique characteristics of aluminum silicon (Al-Si) alloys, namely having light weight, high strength, high toughness, excellent corrosion resistance and recycling capabilities make them the apparent choice of material by engineers for a variety of applications. Therefore, we are seeing more and more components manufactured from aluminum alloys appear in the automobiles such as engine cradles, front and rear suspension frames, drive shafts and wheels.

Silicon is the main alloying element; provides high fluidity and low shrinkage, which result in good castability and weldability. Also the low thermal expansion coefficient and the high hardness of the silicon particles for wear resistance are used in

pistons. The maximum amount of silicon in cast alloys is on the order of 22-24 wt. % Si, but as high as 40-50 wt. % Si can be achieved by powder metallurgy. The structure of the alloys can be hypoeutectic, hypereutectic, or eutectic. The properties of a specific alloy can be assigned to the individual physical properties of its main phase components (aluminum solid solution and silicon crystals) and to the volume fraction and morphology of these components [1].

Al-Si alloys are very important for the automotive industry as a result of their mechanical performance. Deformation and wear behaviour of these alloys has been the subject of many experimental and theoretical research studies. Understanding the debonding and fracture mechanisms of Al-Si is necessary for modeling the mechanical response of this material.

## 1.2 Focus of Research

The main interest in this thesis is the aluminum silicon interfaces. One of the most important aspects of composite materials is the understanding of the interface and interface structures. An interface between two different materials is classified as coherent, semi-coherent, or incoherent. In general, the lattice parameters of a bimaterial interface do not match, causing to a geometrical misfit. The interface is incoherent when all atoms near the interface do not have the same local atomic environment. Some atoms will be in a more favorable position than others will. Depending on the strength of the interaction some atoms will move to positions that are more favorable and the atomic structure near the interface. If the lattice parameters at the interface are equal, it is possible that all atoms have the same, favorable, local environment. In that case, the interface is coherent. In practice an interface is usually neither incoherent nor coherent,

but semicoherent. The interface in this case is characterized by regions in which coherence has increased, and by regions in which coherence has decreased [3]. Large ( $>1\mu\text{m}$ ) second phase particles in a matrix material usually have incoherent interfaces. Deformation characteristics of the interface have a strong influence on the mechanical properties of materials containing second phase particles under the contact surfaces. For example, Alpas and Zhang [2], in Fig. 1.1, investigated void and crack nucleation around the Si particles and concluded that the particle/aluminum interfaces are the preferential void nucleation sites.

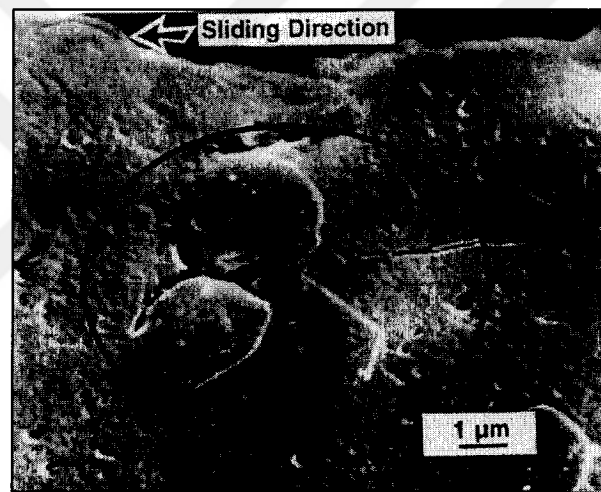


**Fig. 1.1** Void and crack nucleation around the silicon particles under the contact surface (polished, unetched) [2]

In order to understand the mechanical properties of Al-Si interfaces an atomistic model with reliable potential is necessary.

### 1.3 Modeling the Interface

The main techniques that can be used to model the interface and simulate its structure are i) Molecular Dynamics (MD), ii) Monte Carlo (MC) and iii) ab initio

methods. Experiments generally do not provide the molecular level information such that behaviour of molecules to the applied force and structure properties at such microscopic scales. Therefore simulations using these methods are required.

Monte Carlo (MC) methods are based on the use of random numbers and probability statistics to investigate problems in many diverse fields, from the simulation of complex physical phenomena such as radiation transport in the earth's atmosphere to such as the simulation of a Bingo game and regulating the flow of traffic [17, 60]. Solving equations describing the interactions between two atoms is fairly simple; however solving the same equations for hundreds or thousands of atoms is impossible. With the help of MC methods, a large system can be simulated in a number of random configurations, and that data can be utilized to describe the system as a whole.

Molecular dynamics (MD) is a computer simulation technique to predict the time evolution of a system of interacting particles (atoms, molecules, etc.) by numerically integrating Newton's equations of motion. Details are given in section 1.3.1. The additional concepts and techniques are required in the implementation of the main principle. For that reason, much work has been done to turn a simple principle into a useful tool to model an atomistic or a molecular system obtaining information about its equilibrium and non-equilibrium properties. In this thesis, MD simulations are used to model the interface of Al-Si alloys.

Fig. 1.2 indicates how computers simulations, theory and experiments work together to understand the material properties [3].

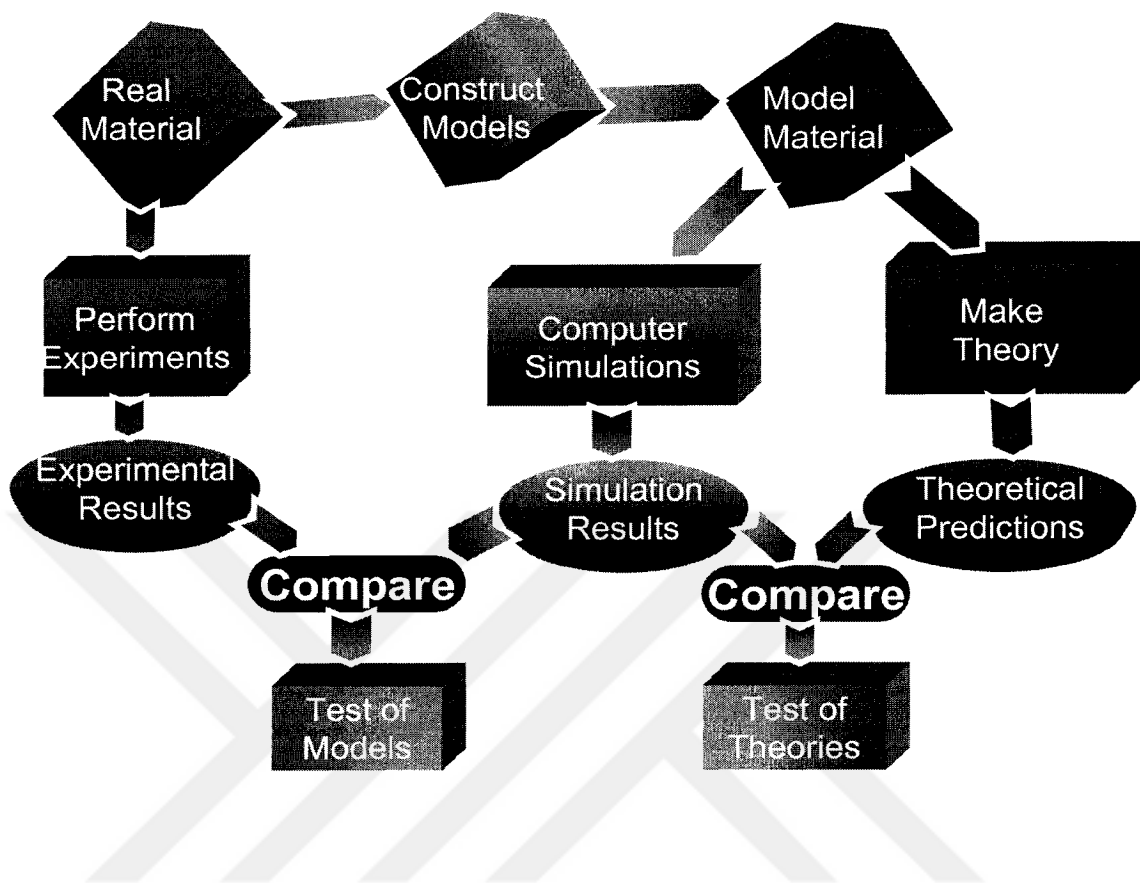


**Fig. 1.2** Schematic diagram of how simulations work.

### 1.3.1 Molecular Dynamics

MD simulations are used to investigate the structure, dynamics and thermodynamics of the materials. The obvious advantage of MD over MC is that it gives a route to dynamical properties of the system: transport coefficients, time-dependent responses to perturbations, rheological properties and spectra [4].

The molecular dynamics method was first introduced by Alder and Wainwright [5] in the late 1950's to study the interactions between hard spheres. The behaviour of simple liquids is understood from their studies such as fluid solid phase transitions. In 1964, Rahman [6] carried out the first simulation using a realistic potential for liquid

argon. The first molecular dynamics simulation of a realistic system was done by Rahman and Stillinger [7] in their simulation of liquid water in 1974. They presented the analysis of fluctuations in density and in transverse currents occurring in a system of 216 water molecules using MD. The simulation techniques with increasing power of computers have greatly expanded, many specialized techniques can now be found for particular problems, including the mixed quantum mechanical - classical simulations. MD simulation techniques are also used in experimental procedures such as X-ray crystallography and nuclear magnetic resonance (NMR) spectroscopy for structure determination. We are now in the enviable position of being able to arrive at practical solutions to problems that we could once only imagine [8].

In practice, for a system of interest, a set of initial conditions (initial positions and velocities) are specified, and interaction potentials for deriving the forces among all particles are chosen, then solving a set of classical equations of motion for all particles in the system gives the evolution of the system in time. Equations of motions given by Newton:

$$m_i \vec{a}_i = \vec{F}_i, \text{ or } m_i \frac{d\vec{v}_i}{dt} = \vec{F}_i, \text{ or } m_i \frac{d^2\vec{r}_i}{dt^2} = \vec{F}_i \text{ for the } i\text{th particle} \quad (1.1)$$

where  $m$ ,  $\vec{v}$ , and  $\vec{a}$  are the mass, velocity, and acceleration of the particle and  $\vec{F}$  is the force acting on it.

### 1.3.2 Density Functional Theory

Basically, all of the information needed to calculate the dynamics of a system can be found from the potential energy function,  $V$ , of the system. The force on atom  $i$  in the system can then be determined from the equation:

$$F = -\nabla V \quad (1.2)$$

where  $\nabla$ , the gradient is the vector operator.

The Embedded Atom Method (EAM) potential is developed from density functional theory (DFT) calculations and its original idea was that each atom is embedded in a host electron gas created by its neighboring atoms.

The main objective of DFT is to replace the many-body electronic wave function with the electronic density as the basic quantity. Whereas the many-body wave function is dependent on  $3N$  variables, three spatial variables for each of the  $N$  electrons, the density is only a function of three variables and is a simpler quantity to deal with both conceptually and practically.

DFT describes the interaction between the electrons and nuclei of the system and is a successful approach for the description of ground state properties of metals, semiconductors, and insulators. Its aim is to find the ground state energy of the system as a function of the electron density.

Hohenberg and Kohn [9], developed a theory based on the electron density in 1964 and Kohn was awarded the Nobel Prize in 1998 for his pioneering work. Their theorem asserts that the density of any system determines all ground-state properties of

the system. In many cases DFT with the local-density approximation gives quite satisfactory results, for solid-state calculations [10].

### 1.3.3 Embedded Atom Method (EAM), Modified Embedded Atom Method (MEAM)

The choice of the potential energy function is very important for the accuracy of the trajectories of atoms obtained from the MD simulations. Because, in MD simulations, we need to consider the forces between the atoms and these forces are found using Eq. (1.2). Then the current positions and velocities can be calculated using Eq. (1.1). EAM and MEAM are the two important potential functions that are widely used for a large number of elements.

One of the principal techniques used in the MD simulations is the Modified Embedded-Atom Method (MEAM) with the Verlet integration algorithm. The Embedded-Atom Method (EAM) was improved by Daw and Baskes [11, 12] in the early 1980's. This method is based on density-functional theory [13] and was applied successfully to the fcc crystals. In 1989, Baskes, Nelson and Wright [14] developed the MEAM for the silicon-germanium system. Baskes [15] has extended the MEAM and showed its applicability to a large number of elements. Different from EAM, the angular dependence of the electron density is included in the MEAM.

The MEAM is a powerful tool for analyzing local interfacial failure mechanisms since the structure and/or strength of the interface need not be assumed a priori. Therefore, the MEAM simulations provide insight into the underlying physics of interfacial decohesion and fracture [16].

#### 1.4 Scope of this Thesis

The goal of this thesis is to understand the debonding and fracture mechanisms of Al-Si by modeling the interface using the MEAM in molecular dynamics simulations. Experimental studies showed that one of the most important aspects of composite materials is the understanding of the interface and interface structures. Therefore, a comprehensive understanding of the interface will facilitate the manufacture of materials with optimized properties.

The outline of this thesis is as follows. In the next Chapter, Al-Si interface is introduced. In Chapter 3, the basic properties of the Molecular Dynamics will be described. In Chapter 4, the detailed description of the EAM and MEAM, which is used in this thesis on Al-Si system, are given. Chapter 5 is the review of the two important researches done by Gall and Needleman [16, 33]. Chapter 6 describes the details of the simulations on this project. In Chapter 7 the results and discussions are presented. The main conclusions of the results from the simulations and future work will be given in Chapter 8. Finally an appendix contains the force calculations from MEAM, followed by the list of references.

## CHAPTER II

### AL-SI INTERFACE

In this chapter, the description of an Al-Si interface is given and experimental and theoretical studies are explained in detail.

#### 2.1 Introduction

An interface is defined as the boundary between two non-miscible materials. A solid interface is also defined as a small number of atomic layers that separate two solids in intimate contact with one another, where the properties differ significantly from those of the bulk material it separates [18]. Fig. 2.1 is an example of aluminum-silicon interface about specific directions [16].

The goal of studying an interface is to facilitate the manufacture of technological materials with optimized properties. A comprehensive understanding of the atomic structure of interfaces helps to rationalize their influence on material processes. The parameters which govern interface structure and behaviour should be considered; in addition to the crystallographic and compositional variables that define a polycrystalline system. The external conditions, temperature, stress, electric/magnetic fields, radiation and chemical environment need to be taken into account. In this thesis it is not feasible to review the interface science in depth, and the detailed information can be found on the text by Sutton and Balluffi [19].

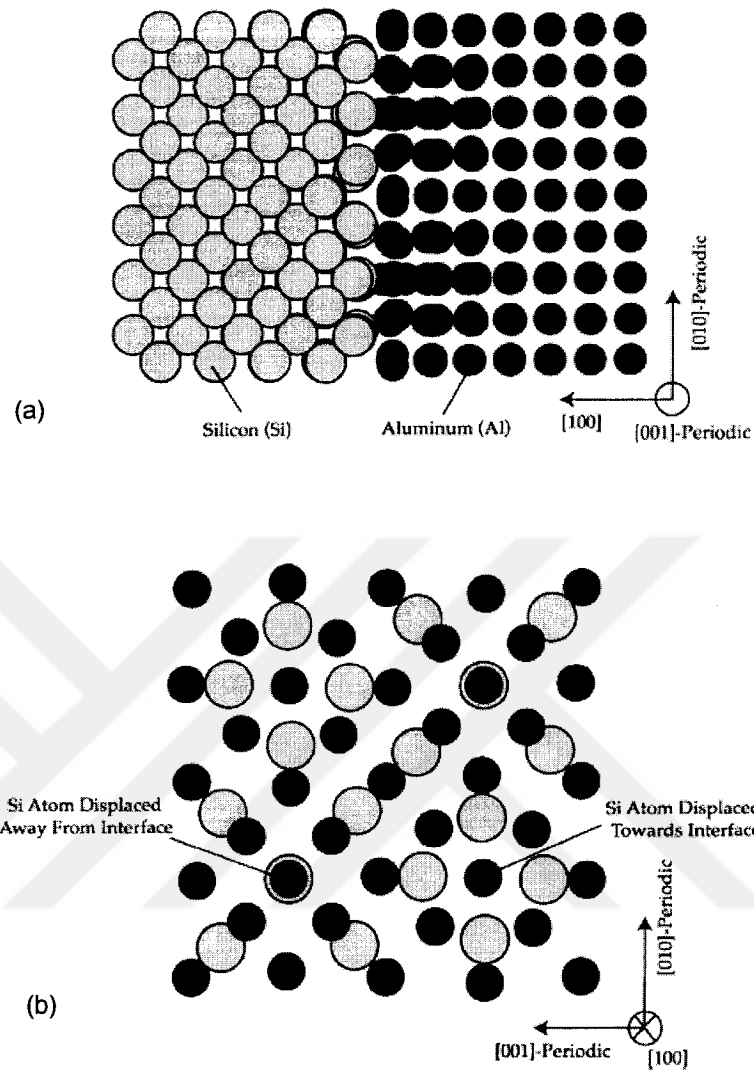


**Fig. 2.1** The relaxed structure (total energy minimized through a static simulation at 0 K) of the aluminum-silicon interface where  $[100]_{\text{Si}} \parallel [100]_{\text{Al}}$ . The model is periodic in the  $[010]$  and  $[001]$  directions, the viewing direction is the (a)  $[001]$  direction and the (b)  $[100]$  direction [16].

Thermodynamic considerations of interfaces are based on the method introduced by Gibbs [19]. According to Gibbs, interfaces are not thermodynamically free regions, i.e. should not be viewed as independent phases existing in equilibrium with surrounding

material. Instead, their influence on polycrystals is treated as a perturbation of the system and is expressed in terms of excess thermodynamic quantities. This formulation emphasizes the complex interactions that may occur between material at the interfacial region and in the bulk of the adjacent crystals. For example, impurities may segregate to an interface at lower temperatures, and desegregate at higher ones. In general, the contribution of the excess free-energy due to the presence of interfaces to the total free energy of a polycrystalline aggregate depends on all of the internal degrees of freedom of the system and the environmental conditions mentioned above. Moreover, its significance may change as a microstructure evolves during manufacture or service.

## 2.2 Experimental Studies

Interfaces, which are buried structures, are more problematic to investigate than free surfaces. For example, scanning electron microscopy (SEM) has been used to study mechanical phenomena such as relative grain motions in polycrystals, electrical features like carrier depletion regions, and chemical concentrations of interfaces. Another technique is the use of electron back-scatter diffraction (EBSD) which enables phase identification and grain orientation determination. Two other techniques that provide valuable chemical information, X-ray photoelectron and Auger spectroscopy, are applied to exposed surfaces following intergranular fracture induced in high vacuum. The performance of the atom-probe field-ion microscope has continued to be refined, and is capable of revealing structural and chemical information at the atomic level by sequential removal and analysis of the surface layers of a needle-like specimen [20]. Transmission electron microscopy (TEM) is the most effective technique for directly revealing the structure and chemistry of interfaces. The principal imaging modes are diffraction

contrast (DC) and high-resolution (HR). Crystallographic information can be obtained using diffraction. Chemical information can be carried out by analysis of emitted characteristic X-rays. A small number of *in situ* studies of interfacial processes have been published, for example penetration of interfaces in Al by liquid Ga, and phase transformations.

Investigations using DC imaging have revealed much about the defect structure of interfaces. In addition, very precise measurements of the relative position of adjacent crystals have been made. HR imaging has elucidated the structure of interfaces in a wide range of materials, and the recent introduction of the z-contrast method enables chemical species to be differentiated [21].

In this section, some experimental studies on Al-Si alloys will be presented. Al-Si interface is an incoherent interface because of the large second phase particles (Si) embedded in a matrix material (Al). The interface is generally the weakest link for failure.

The nucleation of voids from inclusions and second phase particles is very important in limiting the ductility and toughness of solids. The voids initiate by two ways: i) inclusion cracking or ii) decohesion of the interface.

The general behaviour of the particle cracking can be presented briefly [22]:

- (a) the stress needed for particle cracking decreases as particle size increases;
- (b) the cracking of particles happens rarely before yielding, but it occurs after the beginning of plastic deformation,
- (c) the number of cracked particles increases as the strain or stress increases;
- (d) most of the cleavage planes are perpendicular to the tensile axis; and

(e) long particles crack more easily than spherical particles.

The models for the crack initiation theory can be divided to three categories: i) stress criterion, ii) strain criterion, and iii) energy criterion.

Gurland and Plateau [23], in 1963, showed the role of inclusions in ductile fracture experimentally and theoretically. Microscopic observations showed that inclusions or precipitates are mostly the source of cracks that lead to fracture. They suggested three different stages for this type of ductile fracture: i) formation of cracks at inclusions; ii) growth of the cracks; iii) failure.

Gangulee and Gurland [24] expressed the fracture probability by a relation of the type:

$$P = k_p \sigma \cdot d^{1/2} / f^{1/2} - k_0 \quad (2.1)$$

where  $\sigma$  is the applied true stress,  $d$  is the average diameter and  $f$  is the volume fraction of the particles. They also showed that the larger particles break preferentially.

Alpas, Hu and Zhang [25] have researched experimentally the plastic deformation and damage accumulation below the worn surfaces. They showed that the flow stress and strains at the subsurface regions obeyed a Voce type exponential constitutive equation. Perrin and Rainforth [26] also found the same relation for Al-Cu and Al-Si alloys and studied the work hardening regimes for these alloys. Alpas and Embury [27] indicated that high amount of strain under the contact surface causes stress localization in ductile materials, which in turn leads into crack initiation and propagation through the shear bands.

As indicated in Chapter 1, Alpas and Zhang [2] studied the importance of damage accumulation events in delamination wear and modeled the delamination wear

by applying void growth theories of ductile fracture. They showed that in Fig. 2.2 void and crack nucleation around the Si particles. They reached a conclusion that the particle/aluminum interfaces are the preferential void nucleation sites.

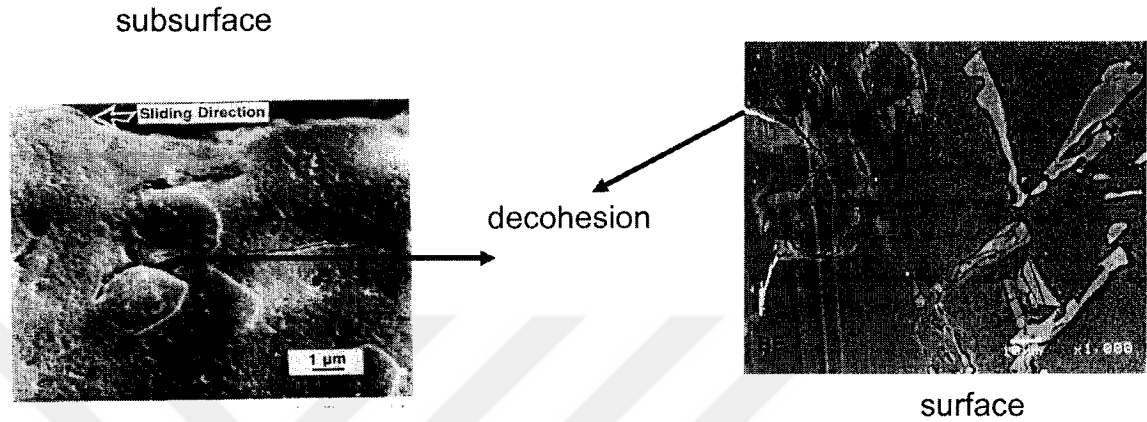


**Fig. 2.2** Void and crack nucleation around the silicon particles under the contact surface and on the surface (polished, unetched) [2].

Gall et al. studied the fracture in A356-T6 Al alloy and Fig. 2.3 shows the fractured and debonded Si particles for this alloy subjected to cyclic loading conditions [28].

### 2.3 Computer Simulations

Atomic scale modeling of interfacial structure and processes using computer simulation techniques has provided stimulating insights. The reader is referred to chapter 1 and 3 for a review of methods and achievements. Here, some studies on Al-Si alloys are reviewed.

Multiscale modeling [29], which has been used to understand the microstructural evolution or some process such as crack propagation in a polycrystal, is a valuable research tool. These models are based on thermodynamics with order parameters and interfacial energies included in the input data. Crack propagation studies involve the

consideration of events at the atomic scale, as well as microscopic modeling of plasticity at the crack tip and also longer range elastic stresses and processes such as diffusion. Deformation of polycrystals with grain sizes ranging from millimeters down to the nanoscale has been studied. These works have indicated that deformation occurs primarily at the interfaces in nanomaterials, and the Hall-Petch relationship between yield stress and grain size breaks down [19]. Such multiscale investigations are very promising.

Baskes et al. examined the interface between a silicon substrate and a thin overlayer of nickel by using MEAM [30]. In general, they determined the structure and adhesion energy of a thin layer of Ni on a Si substrate. However, such MEAM studies on Ni-Si interfaces have not considered the effects of different MEAM models on the strength of the interface.

Baskes et al. [16] used the semi-empirical MEAM to model the Al-Si interface under imposed tensile boundary conditions. They studied the stress-strain and traction-displacement responses of Al and Si blocks of various sizes. They also investigated the effect of randomly dispersed point vacancy defects on the strength of the interface and the effect of crack-like vacancy defect size on the competing failure mechanisms of Al-Si.

In Gall et al. [31], used finite element calculations to obtain the evolution of local stress and strain distributions with respect to the far-field boundary conditions on the second phase particles fracture or debonding. One consideration in the finite element modeling of interface debonding, and crack propagation in general, is modeling the generation of free surfaces. Needleman [32] used a cohesive zone model for describing the process of void nucleation from initial debonding through complete decohesion. He

also studied the tensile decohesion along an interface and decohesion along an imperfect interface using the cohesive zone type interface model by taking full account of finite geometry changes [33, 34].

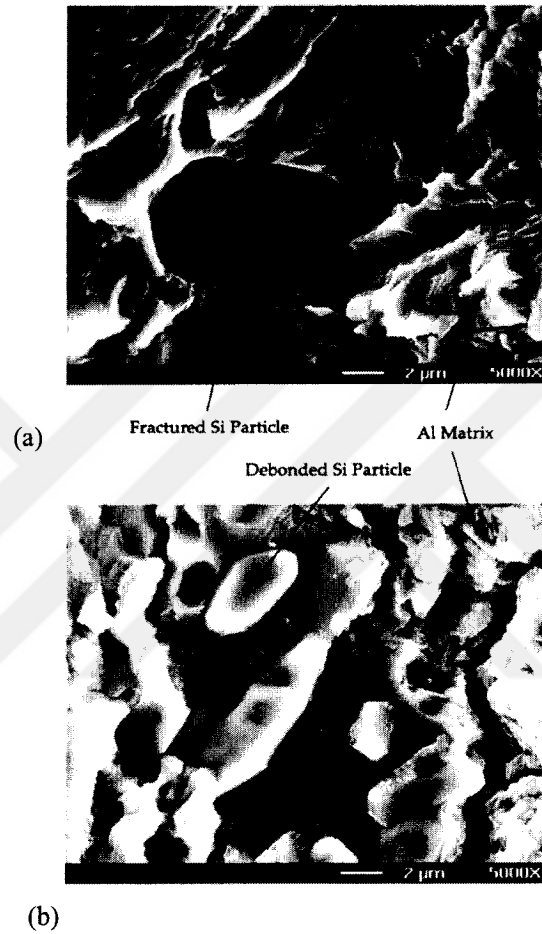


**Fig. 2.3** Scanning electron microscope (SEM) images of the fracture surface of a cast A356-T6 Al alloy subjected to cyclic loading conditions. The images demonstrate that pure silicon inclusions are observed to both (a) fracture and (b) debond [28].

Yamakov and coworkers [35] simulated the atomic level deformation for nanocrystalline Al microstructure and showed that mechanical twinning may play an important role in the deformation behaviour of nanocrystalline Al. The same group [36]

also proposed a two dimensional stress-grain size deformation-mechanism map for the mechanical behaviour of nanocrystalline metals at low temperature. This map showed the change in the deformation mechanism and the related mechanical behaviour with decreasing grain size and its dependence on the stacking-fault energy, the elastic properties of the material and the magnitude of the applied stress.

Fig. 2.4 shows the results from extended finite element method (XFEM) simulations of the crack propagation pattern in multi inclusion system with three crack nuclei. In this figure,  $F$  represents the traction force and  $L$  is the length of the sample. Due to the assumptions of continues displacement along the matrix inclusion interfaces; no delamination has been observed [37].

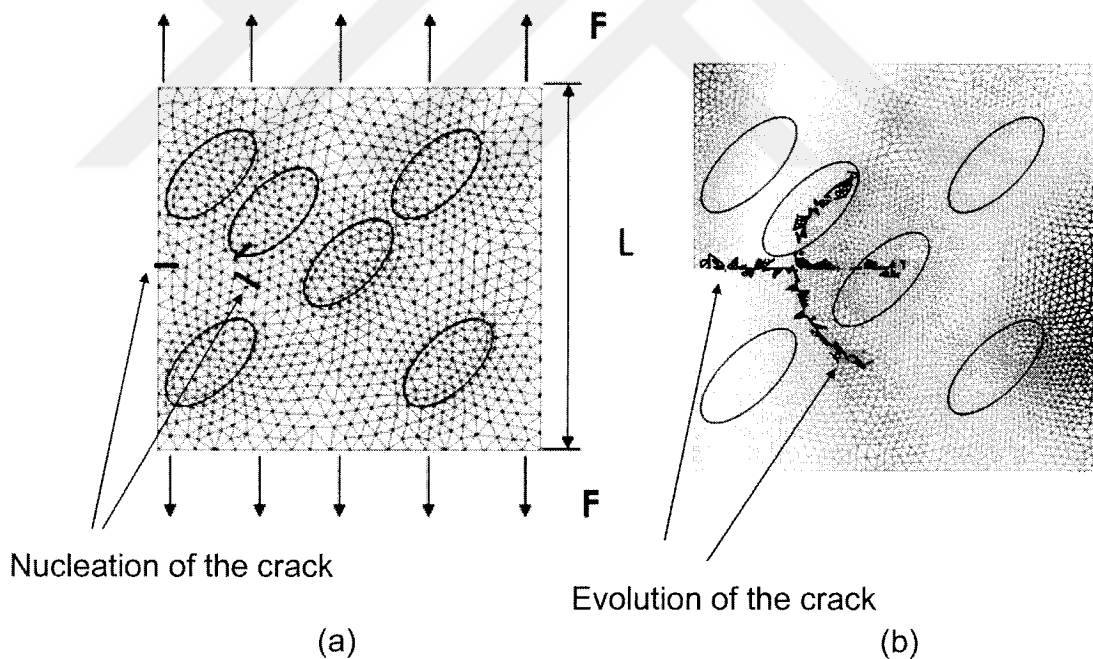


**Fig. 2.4** XFEM simulations of crack propagation in Al-Si: (a) nucleation of the crack, (b) evolution of the crack [37]

It is necessary to determine how continuum-based traction versus displacement laws compare with full-scale atomistic simulations, which are based on similar atomic potentials. A direct comparison between continuum models and the predictions of atomistic simulations further motivates the use of such continuum approaches and helps to quantify their range of applicability [16].

Finally, experimental studies and computer simulations allow us to understand of the interfaces. Therefore, an atomistic model with reliable potential is necessary to comprehend the mechanical properties of Al-Si interfaces.

## CHAPTER III

### MOLECULAR DYNAMICS

#### 3.1 Introduction

In this chapter, first, the general principles of the Molecular Dynamics (MD) method are discussed, and in the following sections, more details are given and special techniques are considered.

Today, extensive experimental work is undertaken in many different alloys to understand their interface properties and to find the optimum conditions; however, doing experiments on each conditions and analyzing them are extremely costly and time consuming, also it is not possible carry out experiments in every condition. Therefore, there is a need for an alternative method to understand these materials better by decreasing experimental effort and cost. At this point, MD plays very important role in the analysis of the behaviour of materials at an atomistic level that can not be obtained either by other theoretical methods or by experiments [38].

Starting from late 1950's, especially with the help of powerful computers, MD has become a very popular simulation method to understand material properties. With the exception of the Monte Carlo method, which is a statistical probabilistic approach, MD represents a deterministic technique that allows predicting the time evolution of a system consisting of interacting particles. It is summarized well by Laplace [3,39]: 'Given for one instant an intelligence which could comprehend all the forces by which nature is animated and the respective situation of the beings who compose it –an intelligence sufficiently vast submit these data to analysis – it would embrace in the same formula the

movements of the greatest bodies of the universe and those of lightest atom; for it, nothing would be uncertain and the future, as the past, would be present to its eyes’.

Basically, MD simulation is a commonly used tool in the materials science for modeling solids and liquids at the atomic level. MD simulation is the numerical solution of Newton’s equations of motion for an ensemble of atoms. These equations of motion are integrated using several methods such as Verlet algorithm for very short time intervals (2-3 fs). Thus, for a system of interacting particles equations of motion is given by

$$m \frac{d^2 \vec{r}_i}{dt^2} = \frac{d(m\vec{v}_i)}{dt} = \frac{d\vec{p}_i}{dt} = \vec{F}_i \quad (3.1)$$

where  $m$  is the mass of the particle and  $\vec{r}_i, \vec{v}_i, \vec{p}_i, \vec{F}_i$  are the position, velocity, momentum and force exerted on atom respectively. Therefore, given the position  $r$  and velocity  $v$  of each particle in the system at time  $t_0$ , the subsequent position  $r(t_0 + \Delta t)$  and velocity  $v(t_0 + \Delta t)$  of a particle is calculated using Eq. (3.1).

A basic MD code is summarized by Fig. 3.1.

Equations of motion have different forms such as Newtonian, Lagrangian and Hamiltonian. In this research a Newtonian approach was used; however Lagrangian and Hamiltonian equations of motion can also be used for MD simulations. Here, a summary of these formulations is given.

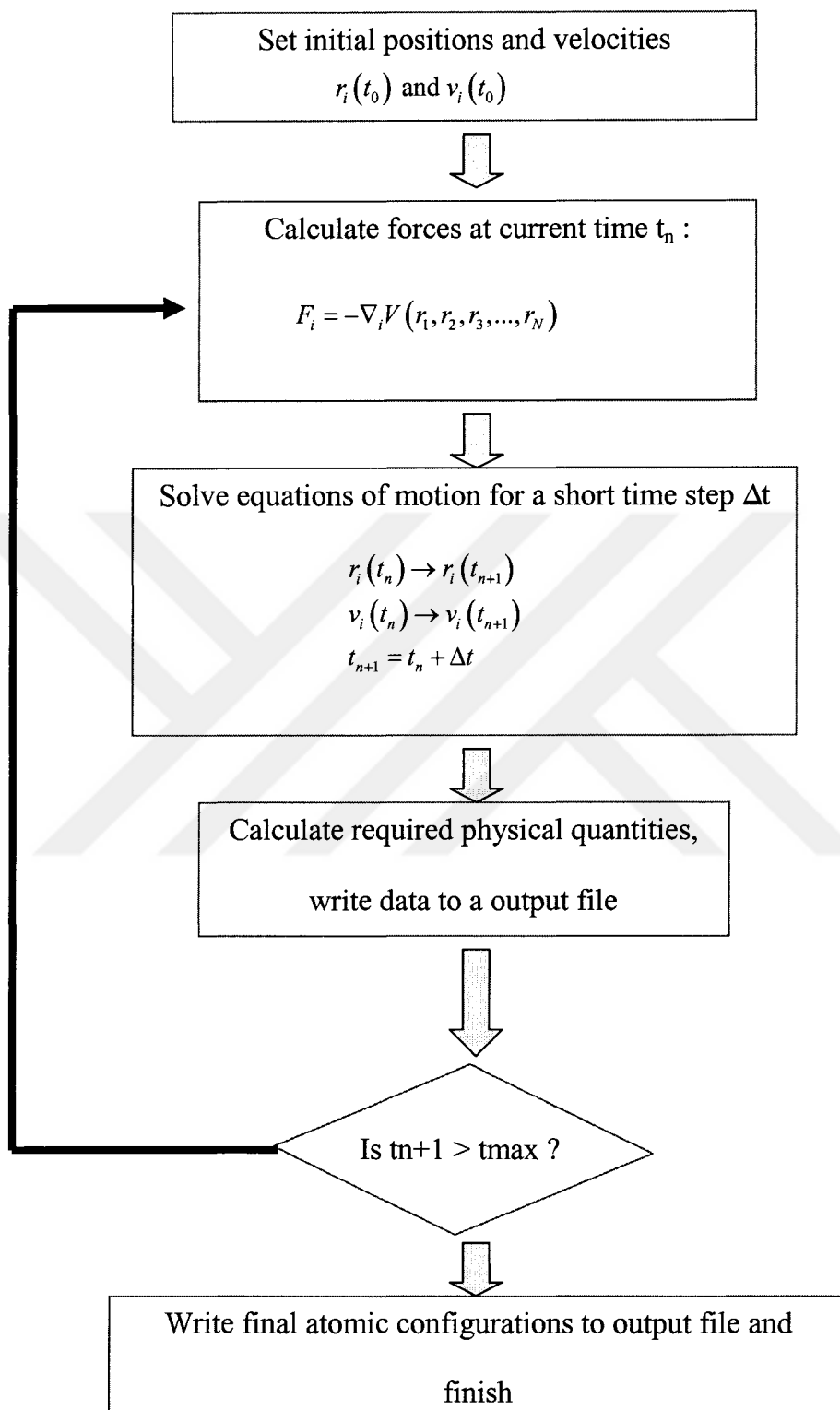


**Fig. 3.1** Schematic diagram of a basic MD code.

A set of generalized coordinates,  $q_j$ , and their time derivatives, as well as generalized velocities,  $\dot{q}_j$  are defined. The position vector,  $r$ , is related to the generalized coordinates by the transformation equation

$$r = r(q_i, q_j, q_k, t) \quad (3.2)$$

where  $t$  is the time.

Consider an arbitrary displacement  $\delta r$  of the particle. The work,  $W$ , done by the applied force  $F$  is  $\delta W = F \cdot \delta r$ . Using Newton's second law

$$F \delta r = m \ddot{r} \delta r \quad (3.3)$$

Since work is a physical scalar quantity, rewriting this equation in terms of the generalized coordinates and velocities gives

$$\begin{aligned} F \delta r &= -\nabla V \sum_i \frac{\partial r}{\partial q_i} \delta q_i = -\sum_{i,j} \frac{\partial V}{\partial r_j} \frac{\partial r_j}{\partial q_i} \delta q_i \\ &= -\sum_i \frac{\partial V}{\partial q_i} \delta q_i \end{aligned} \quad (3.4)$$

The right hand side is difficult to solve, but after some rearranging it can be written:

$$m \ddot{r} \delta r = \sum_i \left[ \frac{d}{dt} \frac{\partial K}{\partial \dot{q}_i} - \frac{\partial K}{\partial q_i} \right] \delta q_i \quad (3.5)$$

where  $K$  is the kinetic energy of the particle. The equation of motion for the work done becomes

$$\sum_i \left[ \frac{d}{dt} \frac{\partial K}{\partial \dot{q}_i} - \frac{\partial(K-V)}{\partial q_i} \right] \delta q_i = 0 \quad (3.6)$$

However, this must be true for any set of generalized displacements  $\delta q_i$ , so we must have

$$\left[ \frac{d}{dt} \frac{\partial K}{\partial \dot{q}_i} - \frac{\partial(K-V)}{\partial q_i} \right] = 0 \quad (3.7)$$

for each generalized coordinate  $\delta q_i$ . Further simplification can be done by noting that  $V$  is a function of only  $r$  and  $t$ , and  $r$  is a function of the generalized coordinates and  $t$ . Therefore,  $V$  is independent of the generalized velocities. Using this into the preceding equation and substituting  $L = K - V$ , Lagrange's equations are obtained

$$\frac{\partial L}{\partial q_i} = \frac{d}{dt} \frac{\partial L}{\partial \dot{q}_i} \quad (3.8)$$

Hamiltonian mechanics aims to replace the generalized velocity variables with generalized momentum variables, also known as conjugate momenta. By doing so, it is possible to handle certain systems, such as aspects of quantum mechanics that would otherwise be even more complicated.

For each generalized velocity, there is one corresponding conjugate momentum, defined as

$$p_j = \frac{\partial L}{\partial \dot{q}_j} \quad (3.9)$$

In Cartesian coordinates, the generalized momenta are precisely the physical linear momenta. In circular polar coordinates, the generalized momentum corresponding to the angular velocity is the physical angular momentum.

The Hamiltonian is the Legendre transform of the Lagrangian

$$H(q_j, p_j, t) = \sum_i \dot{q}_i p_i - L(q_j, \dot{q}_j, t) \quad (3.10)$$

If the transformation equations defining the generalized coordinates are independent of  $t$ , it can be shown that  $H$  is equal to the total energy  $E = K + V$ .

Each side in the definition of  $H$  produces a differential

$$\begin{aligned} dH &= \sum_i \left[ \left( \frac{\partial H}{\partial q_i} \right) dq_i + \left( \frac{\partial H}{\partial p_i} \right) dp_i \right] + \left( \frac{\partial H}{\partial t} \right) dt \\ &= \sum_i \left[ \dot{q}_i dp_i + p_i d\dot{q}_i - \left( \frac{\partial L}{\partial q_i} \right) dq_i - \left( \frac{\partial L}{\partial \dot{q}_i} \right) d\dot{q}_i \right] - \left( \frac{\partial L}{\partial t} \right) dt \end{aligned} \quad (3.11)$$

Substituting the previous definition of the conjugate momenta into this equation and matching coefficients, we obtain the equations of motion of Hamiltonian mechanics, known as the canonical equations of Hamilton

$$\frac{\partial H}{\partial q_j} = -\dot{p}_j, \quad \frac{\partial H}{\partial p_j} = \dot{q}_j, \quad \frac{\partial H}{\partial t} = -\frac{\partial L}{\partial t} \quad (3.12)$$

Hamilton's equations are first-order differential equations, and thus easier to solve than Lagrange's equations, which are second-order [40].

The Lagrangian for classical mechanics is taken to be the difference between the kinetic energy and the potential energy. This considerably simplifies many physical problems. For example, consider a bead on a hoop. To calculate the motion of the bead using Newtonian mechanics, the forces that the hoop exerts on the bead at each moment should be taken into account. This creates a complicated set of equations. However, the same problem using Lagrangian mechanics is much simpler. Lagrangian finds the solution mathematically, one which minimizes the action. There are fewer equations since one is not directly calculating the influence of the hoop on the bead at a given moment.

### 3.2 Interaction Potential

The force acting on the  $i$ th atom at a given time can be obtained from the interatomic potential  $V(r_1, r_2, r_3, \dots, r_N)$  that, in general, is a function of the positions of all the atoms

$$F_i = -\nabla_i V(r_1, r_2, r_3, \dots, r_N) \quad (3.13)$$

where  $N$  is the number of atoms.

Once the initial conditions and the interaction potential are defined, the equations of motion can be solved numerically. The results of the solution are the positions,  $r_i(t)$ , and velocities,  $v_i(t)$ , of all the atoms as a function of time.

The choice of the appropriate potential energy affects the accuracy of the trajectories of atoms from MD simulations. Therefore, the potential energy is very important and plays a main role in MD simulations. There are different potentials that are developed for different class of materials due to the different interacting forces, and

research is in progress for other materials. Generally, there are four main approaches to obtain interaction potentials [41]:

1. Energies obtained from self consistent or semi-approximative quantum mechanical electronic structure calculations.
2. Classical potential based on ad hoc functional forms and assumptions (empirical potentials)
3. Potentials with analytical forms derived from quantum mechanical based bonding ideas
4. Potentials with both parameters and analytical forms fitted from an extensive input data set

As an example, Lennard-Jones potential, which is originally proposed for liquid argon [42], is given by for a pair of atoms  $i$  and  $j$

$$V(r_{ij}) = 4\epsilon \left[ \left( \frac{\sigma}{r_{ij}} \right)^{12} - \left( \frac{\sigma}{r_{ij}} \right)^6 \right] \quad (3.14)$$

where  $r_i$  and  $r_j$  are the positions of the atoms, and  $r_{ij} = |r_i - r_j|$ . The parameter  $\epsilon$  governs the strength of the interaction while the parameter  $\sigma$  defines a length scale that the interaction repels at close range, and then attracts.

Potentials that we used in the MD simulations are Embedded Atom Potential (EAM) and Modified Embedded Atom Potential (MEAM) and they are explained in details in Chapter 4.

Table 3.1 gives a summary of established concepts for different potential energy functions. [41]

### 3.3 Integration Methods

Many numerical algorithms, such as Verlet algorithm, leap-frog algorithm and predictor-corrector algorithm have been developed to integrate the equations of motion in MD simulations [43]. In choosing which algorithm to use, three important rules should be considered: (1) the algorithm should conserve energy and momentum; (2) it should be computationally efficient, (3) it should permit a long time step for integration; (4) it should be simple in form and easy to program.

Table 3.1 Established concepts for potential energy functions

Potential	Application	Advantage	Drawbacks
Pair Potentials			
Lenard-Jones	VDW Interaction	Easy	Poor for solids
Morse	Dimers	Easy, efficient	Poor repulsive part
Coulomb	Ionic systems	Easy	No charge transfer
Cluster Potentials			
Mechanical Force-Fields	Bonding interaction in organic molecules	Accurate	Must pre-choose bondings
Keating Type	Covalent solids	Accurate	Only one structure
Stillinger-W.	Covalent solids	Fast, reactive	Poor for non solid str.
Pair Functionals			
EAM	Metals and alloys	Bond-order	No angularity
Cluster Functionals			
Tersoff-Abell	Covalent systems	Bond-order, angularity	Overbinding
Brenner (REBOP)	Covalent systems	Bond-order, angularity	Only for hydrocarbons
MEAM	Metals and alloys	EAM + angularity	Many parameters
EDIP	Covalent systems	Bond-order+Keating	?

### 3.3.1 Verlet Algorithm

In all integration algorithms the positions, velocities and accelerations can be approximated by a Taylor series expansion about time  $t$  [3]:

$$\begin{aligned}r^p(t + \delta t) &= r(t) + \delta t v(t) + \frac{1}{2} \delta t^2 a(t) + \frac{1}{6} \delta t^3 b(t) + \dots \\v^p(t + \delta t) &= v(t) + \delta t a(t) + \frac{1}{2} \delta t^2 b(t) + \dots \\a^p(t + \delta t) &= a(t) + \delta t b(t) + \dots \\b^p(t + \delta t) &= b(t) + \dots\end{aligned}\tag{3.15}$$

where  $b$  is the third time derivative of the  $r$ . To derive the Verlet algorithm one can write

$$r(t + \delta t) = r(t) + \delta t v(t) + \frac{1}{2} \delta t^2 a(t)\tag{3.16}$$

$$r(t - \delta t) = r(t) - \delta t v(t) + \frac{1}{2} \delta t^2 a(t)\tag{3.17}$$

Summing these two equations gives

$$r(t + \delta t) = 2r(t) - r(t - \delta t) + \delta t^2 a(t)\tag{3.18}$$

Velocities can be calculated by the formula

$$v(t) = \frac{r(t + \delta t) - r(t - \delta t)}{2\delta t}\tag{3.19}$$

The Verlet algorithm uses positions and accelerations at time  $t$  and the positions from time  $t - \delta t$  to calculate new positions at time  $t + \delta t$ . The Verlet algorithm uses no explicit velocities. The advantages of the Verlet algorithm are, *i*) it is straightforward, and *ii*) the storage requirements are modest, *iii*) it is time reversible. The disadvantage is that the algorithm is of moderate precision.

The leap-frog algorithm is a modified version of the Verlet algorithm. To obtain more accurate velocities, the leapfrog algorithm is used. The velocities at half time step are given by

$$v\left(t + \frac{1}{2}\delta t\right) = v\left(t - \frac{1}{2}\delta t\right) + \delta ta(t) \quad (3.20)$$

The leapfrog algorithm is computationally less expensive than the Predictor-Corrector approach for example, and requires less storage. This is an important advantage in the case of large scale calculations. Moreover, the conservation of energy is respected, even at large time steps. Therefore, the computation time could be greatly decreased when this algorithm is used. However, when more accurate velocities and positions are needed, another algorithm should be implemented, like the Predictor-Corrector algorithm [3].

#### 3.4 Periodic Boundary Conditions and Cut off Radius

How large must the relatively small system be to yield results that come close the behaviour of the real system? There is no unique answer for this question. A system constructed using periodic boundary conditions (PBC) may be used to correlate the properties of the small system to those of the real one. The introduction of periodic boundaries is equivalent to considering an infinite, space-filling array of identical copies of the simulation region [44]. Fig. 3.2 shows a two dimensional view of a simulation cell, here, using PBC, when an atom leaves the central box, its images in the neighbouring boxes move in a similar fashion.

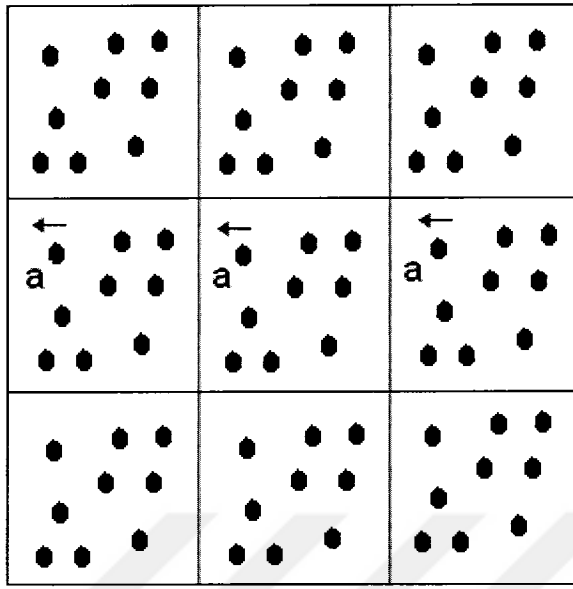


**Fig. 3.2** Two dimensional view of a MD simulations cell using periodic boundary conditions.

The system is made infinite in extent using periodic boundary conditions. In particular, the minimum image rule supposes that each atom  $i$  in the cell interacts with the closest image of all atoms  $j$ . Therefore, the minimum image convention must be taken into account in both the integration of the equations and the interaction potentials. After each integration step, if an atom is found to have moved outside the region its coordinates must be adjusted to bring it back inside. The interaction potentials have an infinite range. In practical applications, it is customary to establish a cutoff radius  $r_c$  and disregard the interactions between atoms separated by more than  $r_c$ . This results in simpler programs and enormous savings of computer resources, because the number of atomic pairs separated by a distance  $r$  grows as  $r^2$  and becomes quickly huge [44].

### 3.5 Neighbour List

In MD simulations, only the atoms that are separated by distances smaller than the cut off radius are considered for the calculations of the interaction potentials and forces. Verlet [43] suggested a method to improve the speed using a list of neighbours of a particular atom and this list is updated at intervals. This is depicted in Fig. 3.3 where  $r_c$  is the cutoff in the potential,  $r_v$  is the cutoff in the Verlet neighbour list and  $r_{diff} = r_v - r_c$ .

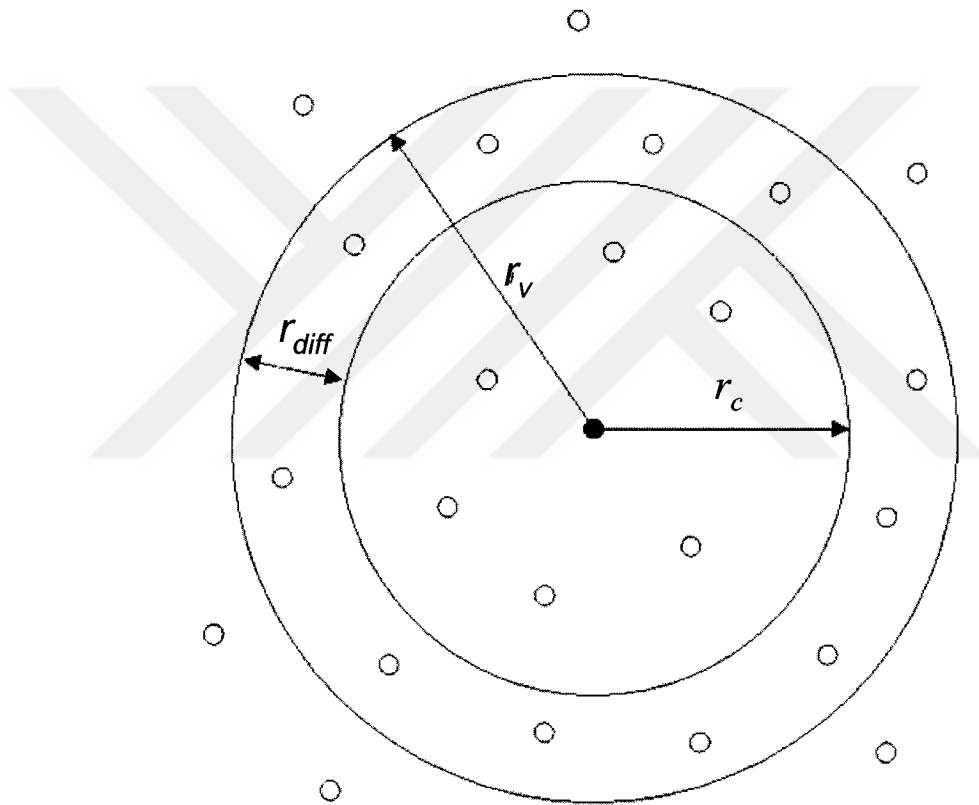


**Fig. 3.3** Cutoff radius and Verlet radius for Verlet neighbour list

As  $r_v$  is larger than the cutoff in the potential, it is only necessary to update this array periodically. When an atom has moved a distance of  $0.5 r_{diff}$  then it is necessary to update the list.

## CHAPTER IV

### THE MODIFIED EMBEDDED ATOM METHOD

In this Chapter, the theoretical background of the Embedded Atom Method and Modified Embedded-Atom Method are described, and the derivations of the MEAM's parameters are explained.

#### 4.1 General Formulation of Embedded Atom Method (EAM)

In EAM, [11, 12] each atom can be viewed as an embedded in a host lattice consisting of other atoms. This method permits calculations using an electron density, which is always definable and makes possible realistic treatment of impurities in structures. EAM is not more complicated than pair potential methods and it is also able of describing more complex situations. Thus, it is a powerful method for MD simulations.

Stott and Zaremba [13] stated that the embedding energy,  $E$ , of an impurity in a host matrix is a functional of the electron density without impurity. It is of the form

$$E = E_{Z,R} [\rho_H] \quad (4.1)$$

where  $\rho_H$  is the electron density of the host without impurity,  $Z$  is the atomic number and  $R$  is the position of the impurity.

The total energy is given by

$$E_{tot} = \sum_i F_i(\rho_{h,i}) + \frac{1}{2} \sum_{\substack{i,j \\ i \neq j}} \phi_{ij}(R_{ij}) \quad (4.2)$$

where  $i$  refers to the atom in question,  $j$  is the neighboring atom,  $R_{ij}$  is the distance between atoms  $i$  and  $j$ ,  $\rho_{h,i}$  is the host electron density (it is approximately the sum of the atomic densities  $\rho^a$ ),  $F_i$  is the embedding function which is the required energy to embed

an atom into the background electron density and  $\phi_{ij}$  is the short range pair potential (core-core repulsion).

The functions  $F$  and  $\phi$  can be determined empirically from the physical properties of the solid. Daw and Baskes [12] have determined these functions using the lattice constants, elastic constants, vacancy formation energy and sublimation energies for fcc and bcc crystals. In these structures, all atoms are equivalent, therefore  $F = F_i$ ,  $\phi = \phi_{ij}$  and  $\rho = \rho_j^a$ . Then the lattice constant is given by the equilibrium constant

$$\begin{aligned} E'_{tot} &= 0 \\ A_{ij} + F'(\bar{\rho})V_{ij} &= 0 \end{aligned} \quad (4.3)$$

where

$$\begin{aligned} A_{ij} &= \frac{1}{2} \sum_m \phi'_m \frac{a_i^m a_j^m}{a^m} \\ V_{ij} &= \sum_m \rho'_m \frac{a_i^m a_j^m}{a^m} \end{aligned} \quad (4.4)$$

and where  $a^m$  is the distance between the neighbours,  $\bar{\rho} = \sum_m \rho(a^m)$  is the electron density at equilibrium and  $\bar{\phi}$  is defined by  $\bar{\phi} = \sum_m \phi(a^m)$ ,  $a_i^m$  is the  $i$ th component of the position vector to the  $m$ th neighbor. Also  $\phi'_m = \left( \frac{d\phi(r)}{dr} \right)_{r=a^m}$  and  $\rho'_m = \left( \frac{d\rho(r)}{dr} \right)_{r=a^m}$

Calculation of elastic constants at equilibrium requires calculation of the second derivative of the total energy, and is given by

$$C_{ijkl} = \left( \frac{B_{ijkl} + F'(\bar{\rho})W_{ijkl} + F''(\bar{\rho})V_{ij}V_{kl}}{\Omega_0} \right) \quad (4.5)$$

where

$$\begin{aligned}
 B_{ijkl} &= \frac{1}{2} \sum_m \left( \phi_m'' - \frac{\phi_m'}{a^m} \right) \frac{a_i^m a_j^m a_k^m a_l^m}{(a^m)^2} \\
 W_{ijkl} &= \frac{1}{2} \sum_m \left( \rho_m'' - \frac{\rho_m'}{a^m} \right) \frac{a_i^m a_j^m a_k^m a_l^m}{(a^m)^2}
 \end{aligned} \tag{4.6}$$

$\Omega_0$  is the undeformed atomic volume,  $\rho''$  and  $\phi''$  represent the second derivatives with respect to  $r$ .

For cubic crystals there are three independent elastic constants

$$\begin{aligned}
 C_{11} &= \left[ B_{11} + F'(\bar{\rho})W_{11} + F''(\bar{\rho})(V_{11})^2 \right] / \Omega_0 \\
 C_{12} &= \left[ B_{12} + F'(\bar{\rho})W_{12} + F''(\bar{\rho})(V_{11})^2 \right] / \Omega_0 \\
 C_{44} &= \left[ B_{12} + F'(\bar{\rho})W_{12} \right] / \Omega_0
 \end{aligned} \tag{4.7}$$

The sublimation energy,  $E_s$ , is given by

$$E_s = - \left[ F(\bar{\rho}) + \frac{1}{2} \bar{\phi} \right] \tag{4.8}$$

The Vacancy formation energy,  $E_v^F$  is

$$E_v^F = -\frac{1}{2} \bar{\phi} + \sum_m \left[ F(\bar{\rho} - \rho_m) - F(\bar{\rho}) \right] + E_{relax}. \tag{4.9}$$

where  $E_{relax}$  is the lattice relaxation energy around the vacancy.

The repulsive pair potentials  $\phi_{ij}$  can be given in a coulombic potential form

$$\phi_{ij} = \frac{Z_i(r)Z_j(r)}{r} \tag{4.10}$$

where  $Z_i$  is the effective charge and  $r$  is the position. Generally, for each element,  $F(\rho)$  and  $Z(r)$  has to be found. Daw and Baskes [12] determined these two functions for Ni and Pd.

Table 4.1 Quantities used for determination of the functions  $F(\rho)$  and  $Z(r)$  for Ni and Pd, and their fitted values. Lattice constant  $a_0$  in  $\text{\AA}$ ; elastic constants  $C_{11}$ ,  $C_{12}$  and  $C_{44}$  in  $10^{12}$  dyn/cm<sup>2</sup>; sublimation energy  $E_s$  in eV; vacancy formation energy  $E_{1V}^F$  in eV; and the energy difference between bcc and fcc phases in eV [12].

	Nickel		Palladium	
	Expt.	Fit	Expt.	Fit
$a_0$	3.52	3.52	3.89	3.89
$C_{11}$	2.465	2.438	2.341	2.305
$C_{12}$	1.473	1.506	1.761	1.803
$C_{44}$	1.247	1.278	0.712	0.755
$E_s$	4.45	4.45	3.91	3.91
$E_{1V}^F$	1.4	1.4	1.4	1.4
$E_{bcc} - E_{fcc}$	0.06	0.07	0.06	0.05

Baskes, Daw and Foiles [45] assumed a simple parameterized form for  $Z(r)$

$$Z(r) = Z_0 (1 + \beta R^\nu) e^{-\alpha R} \quad (4.11)$$

where  $Z_0$  is the number of outer electrons of the atom,  $\alpha$ ,  $\beta$  and  $\nu$  are the parameters.

They found empirically  $\nu = 1$  for Ni, Pd, and Pt,  $\nu = 2$  for Cu, Ag and Au. The values of

$\alpha, \beta$  are determined by the shear moduli of the pure materials and the vacancy formation energy.

For the calculation of the embedding function  $F(\rho)$ , the atomic electron density needs to be found. It is calculated from Hartre-Fock theory as follows [17, 45]

$$\rho^a(R) = n_s \rho_s(R) + n_d \rho_d(R) \quad (4.12)$$

where  $n_s$  and  $n_d$  are the number of s and d electrons at the outer shell and  $\rho_s$  and  $\rho_d$  are the densities for s and d wave functions. Clementi and Roetti [46] calculated the atomic electron densities for s and d electrons

$$\rho_s^a(r) = \frac{\left| \sum_i C_i R_i(r) \right|^2}{4\pi} \quad (4.13)$$

$$R_i(r) = \frac{(2\zeta_i)^{n_i+1/2}}{[(2n_i)!]^{1/2}} r^{n_i-1} e^{-\zeta_i r}$$

where  $n_i, C_i$  and  $\zeta_i$  are the parameters to calculate these densities.

#### 4.2 General Formulation of the Modified Embedded Atom Method (MEAM)

In 1989, Baskes, Nelson and Wright [14] developed the MEAM for the silicon-germanium system. Baskes [15] has extended the MEAM and showed its applicability to a large number of other systems. Different from the EAM, the angular dependence of the electron density is included in the MEAM. Therefore the EAM is limited to early transition metals and covalent systems.

Baskes [17] used the semi-empirical modified embedded-atom method (MEAM) to model the Al-Si interface under imposed tensile boundary conditions. He studied the

stress-strain and traction-displacement responses of Al and Si blocks of various sizes. He also investigated the effect of randomly dispersed point vacancy defects on the strength of the interface and the effect of crack-like vacancy defect size on the competing failure mechanisms of Al-Si.

The modified embedded-atom method (MEAM) is one of the principal techniques used in the MD simulations. The total energy for the MEAM potentials is given by

$$E_{tot} = \sum_i \left[ F_i(\bar{\rho}_i) + \frac{1}{2} \sum_{j \neq i} S_{ij} \phi_{ij}(r_{ij}) \right] \quad (4.14)$$

where the sums are over the atoms  $i$  and  $j$ ,  $r_{ij}$  is the distance between atoms  $i$  and  $j$ , and  $\bar{\rho}_i$  is the host electron density at site  $i$ .  $F_i$  is the embedding function defined as the required energy to place an atom into the electron environment defined by  $\bar{\rho}_i$ ,  $\phi_{ij}$  is the pair interaction between atoms  $i$  and  $j$ , and  $S_{ij}$  is the screening function.

The contribution to the energy from the  $i$ th atom can be written in the form

$$E_i = F_i(\bar{\rho}_i) + \frac{1}{2} \sum_{j \neq i} S_{ij} \phi_{ij}(r_{ij}) \quad (4.15)$$

Considering the case of a homogeneous monatomic solid with interactions limited to first neighbours only [14], the energy per atom of this reference structure as a function of nearest neighbour distance can be given by

$$E_i^u(r_{ij}) = F_i(\bar{\rho}_i^0(r_{ij})) + \frac{Z_i}{2} \phi_{ii}(r_{ij}) \quad (4.16)$$

where  $r_{ij}$  is the nearest neighbour distance,  $\bar{\rho}_i^0$  is the background electron density for this reference structure,  $Z_i$  is the number of a nearest neighbours in the reference structure of a type- $i$  atom and  $E_i^u(r_{ij})$  is the energy of an element in the reference structure. Assuming

that  $E_i^u(r_{ij})$  is known, the pair interaction for type- $i$  atoms can be calculated using Eq.(4.16)

$$\phi_{ii}(r_{ij}) = \frac{2}{Z_i} \left[ E_i^u(r_{ij}) - F_i(\bar{\rho}_i^0(r_{ij})) \right] \quad (4.17)$$

Using this equation, the Eq. (4.15) becomes

$$E_i = \left[ F_i(\bar{\rho}_i) + \frac{1}{Z_i} \sum_{j \neq i} S_{ij} \left( E_i^u(r_{ij}) - F_i(\bar{\rho}_i^0(r_{ij})) \right) \right] \quad (4.18)$$

The energy per atom as a function of nearest neighbor distance is described by the universal equation of state [47]:

$$E_i^u(r_{ij}) = -E_c (1 + a^*) \exp(-a^*) \quad (4.19)$$

with  $a^* = \alpha \left( \frac{r_{ij}}{r_e} - 1 \right)$  and  $\alpha^2 = \frac{9\Omega B}{E_c}$

where  $E_c$  is the cohesive energy which defined as the energy required to break the atoms of the solid into isolated atomic species,  $r_e$  is the nearest neighbor distance,  $\Omega$  is the atomic volume, and  $B$  is the bulk modulus.

In the MEAM, the embedding energy can be given by:

$$F(\bar{\rho}_i) = AE_c \frac{\bar{\rho}_i}{\rho_0} \ln \frac{\bar{\rho}_i}{\rho_0} \quad (4.20)$$

where  $A$  is the adjustable parameter, and  $\rho_0$  is the density scaling parameter.  $\bar{\rho}_i$  is the function of partial electron densities and is given by:

$$\bar{\rho}_i = \frac{2\rho_i^{(0)}}{1 + \exp \left( - \sum_{s=1}^3 t_i^{(s)} \left( \frac{\rho_i^{(s)}}{\rho_i^{(0)}} \right)^2 \right)} \quad (4.21)$$

where  $t_i^{(s)}$  are the weight factors (see appendix),  $\rho_i^{(s)}$  ( $s=0,\dots,3$ ) are the partial electron densities.

The partial electron densities are defined by:

$$\left(\rho_i^{(s)}\right)^2 = \sum_{j,k \neq i} \rho_i^{a(s)}(r_{ij}) \rho_i^{a(s)}(r_{ik}) L^{(s)}(\cos \theta_{jik}) \quad (4.22)$$

with atomic electron densities which decrease exponentially

$$\rho_j^{a(s)}(r_{ij}) = S_{ij} f_c(r_{ij}) f_j^0 \exp\left(-\beta_j^{(s)} \left(\frac{r_{ij}}{r_e} - 1\right)\right) \quad (4.23)$$

where  $\beta^{(h)}$  are the decay lengths (see appendix),  $L^{(s)}$  are the Legendre polynomials, and  $s = 0, 1, 2, 3$ .  $f_c(r_{ij})$  is the cut off function (see the appendix for details),  $S_{ij}$  is the screening function and  $f_j^0$  is the parameter.

The Legendre polynomials for these  $s$  values are:

$$L^{(0)}(z) = 1, \quad L^{(1)}(z) = z, \quad L^{(2)}(z) = \frac{1}{2}\left(z^2 - \frac{1}{3}\right), \quad \text{and} \quad L^{(3)}(z) = \frac{1}{2}\left(z^3 - \frac{3}{5}z\right)$$

The electron densities and the pair potential are multiplied by the screening function, and their definitions are as follows [48]:

$$S_{ik} = \prod_{j \neq i,k} S_{ijk} \quad (4.24)$$

A simple elliptical geometry (Fig. 4.1) is used to calculate the  $S_{ijk}$ . The equation of ellipse is

$$x^2 + \frac{1}{C} y^2 = \left(\frac{1}{2} r_{ik}\right)^2 \quad (4.25)$$

where  $C$  is the parameter and given by:

$$C = \frac{2(X_{ij} + X_{jk}) - (X_{ij} - X_{jk})^2 - 1}{1 - (X_{ij} - X_{jk})^2} \quad (4.26)$$

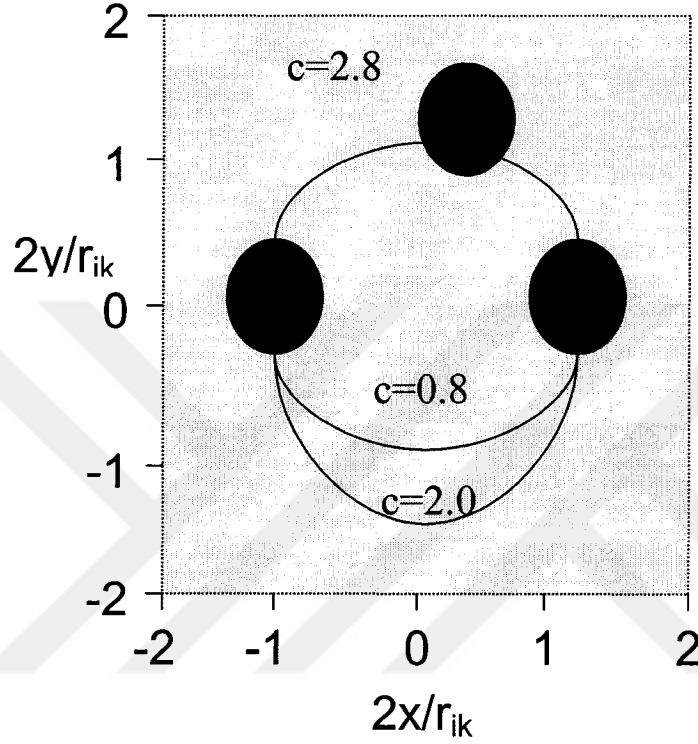


**Fig. 4.1** Ellipse geometry for calculating screening parameter,  $S_{ijk}$ .

where  $X_{ij} = (r_{ij} / r_{ik})^2$  and  $X_{jk} = (r_{jk} / r_{ik})^2$ . Then the screening function can be given by:

$$S_{ijk} = f_c \left[ \frac{C - C_{\min}}{C_{\max} - C_{\min}} \right] \quad (4.27)$$

where  $C_{\max}$  and  $C_{\min}$  are the limiting values of  $C$  (see Fig. 4.1). The cutoff function  $f_c$  is given by:

$$f_c(x) = \begin{cases} 1 & x \geq 1 \\ (1 - (1 - x)^4)^2 & 0 < x < 1 \\ 0 & x \leq 0 \end{cases} \quad (4.28)$$

The radial cutoff function which is used in the electron densities is equal to:

$$f_c(r_{ij}) = f_c\left(\frac{r_c - r_{ij}}{\Delta r_{ij}}\right) \quad (4.29)$$

where  $r_c$  is the cutoff distance and  $\Delta r_{ij}$  is the cutoff region.

In order to use this potential in MD simulations we need to find the forces. The gradient of a scalar is defined as:

$$\nabla f = \frac{\partial f}{\partial x} i + \frac{\partial f}{\partial y} j + \frac{\partial f}{\partial z} k \quad \text{or} \quad \nabla = \sum_{m=1}^3 i_m \frac{\partial}{\partial x_m} \quad (4.30)$$

$$\vec{F}_i = -\vec{\nabla} E_{tot} \quad (4.31)$$

The force can be calculated using the following equation:

$$\vec{F}_i = -\sum_i \left[ \sum_{m=1}^3 i_m \left( \frac{\partial F_i}{\partial \bar{\rho}_i} \frac{\partial \bar{\rho}_i}{\partial r_{ij}} \frac{\partial r_{ij}}{\partial x_m} + \frac{1}{2} \sum_{j \neq i} \left( S_{ij} \frac{\partial \phi(r_{ij})}{\partial r_{ij}} \frac{\partial r_{ij}}{\partial x_m} \right) \right) \right] \quad (4.32)$$

The derivation of the forces is given in Appendix A.

Eq. (4.32) is used to calculate the forces between the atoms, and as explained Chapter 3, then the new positions and velocities of each atom derived from the these forces. This equation is implemented into our MD program.

## CHAPTER V

### PREVIOUS WORK

#### 5.1 Introduction

In this chapter two important studies which are significant for the work presented in this thesis are reviewed in details.

First, the work of Gall et al. [16], titled “Atomistic simulations on the tensile debonding of an aluminum–silicon interface.” is summarized. Their paper presented a MEAM simulation of the deformation and fracture characteristics of an incoherent interface between the pure FCC aluminum and diamond cubic silicon. Their simulations showed that the relaxed interface possesses a rippled structure, instead of a planar atomic interface, and such ripples act as local stress concentrators and initiation sites for interfacial failure. The stress–strain (traction–displacement) relationship of aluminum and silicon blocks on the interface depends on the distance from the interface at which the boundary conditions are applied, i.e. the size of the atomic blocks, and the location of the measured opening displacement. They also investigated the point vacancy defects near the interface and they found out that the point vacancy defects decrease the maximum normal tensile stress that the interface can support at a rate almost linearly proportional to the number fraction of the dispersed defects. Finally, a crack-like vacancy defect in the bulk aluminum or silicon is simulated, it must reach an area fraction (projected to the surface normal to the tensile axis) of about 50 or 30%, respectively, in order to shift the failure from the interface to the bulk materials.

Then, a Needleman [34] is reviewed. In this paper, a cohesive zone type interface model, that takes full account of finite geometry changes, is used to study the decohesion of a viscoplastic block from a rigid substrate.

## 5.2 Atomistic Simulations on the Tensile Debonding of an Aluminum–Silicon Interface

In this paper, Gall et al.[16] considers the stress–strain and traction–displacement responses of Al and Si blocks of various sizes, subjected to tensile boundary conditions applied parallel to the plane normal to the interface. The effect of randomly dispersed point vacancy defects on the strength of the interface was also investigated. Then, the effect of a crack-like vacancy defect on the Al–Si interface debonding versus isolated fracture in the Al or Si has been considered. Different locations for measuring opening displacement in the framework of a continuum-based cohesive zone approach have been discussed.

The following parameters remained constant throughout the investigation:

1. The model was periodic in the [010] and [001] crystallographic directions, and it contained free surfaces perpendicular to the [100] direction (Fig. 5.1);
2. The constant temperature molecular dynamics simulations were conducted at 300K, and the static simulations were conducted at 0 K;
3. The cubic axis for the FCC aluminum and the diamond cubic silicon blocks were aligned, i.e.  $[100]_{\text{Al}} \parallel [100]_{\text{Si}}$ ,  $[010]_{\text{Al}} \parallel [010]_{\text{Si}}$ ,  $[001]_{\text{Al}} \parallel [001]_{\text{Si}}$ , and the interface normal was parallel to the [100] direction;
4. The two complimentary atomic planes farthest from, and parallel to the interface, were displaced at velocities of  $1 \text{ \AA}^\circ / \text{ps}$  along the [100] and  $[\bar{1}00]$  crystallographic

directions. Atoms in the displaced planes were fixed from moving in the [010] and [001] directions.

The velocity was chosen arbitrarily, and its effects on simulation results are not studied systematically. However, one extremely high strain rate (dynamic simulation with velocity of  $1\text{\AA}/\text{ps}$ ) and one extremely low strain rate (static simulation) have been used. The results show that the influence is small compared to other significant effects.

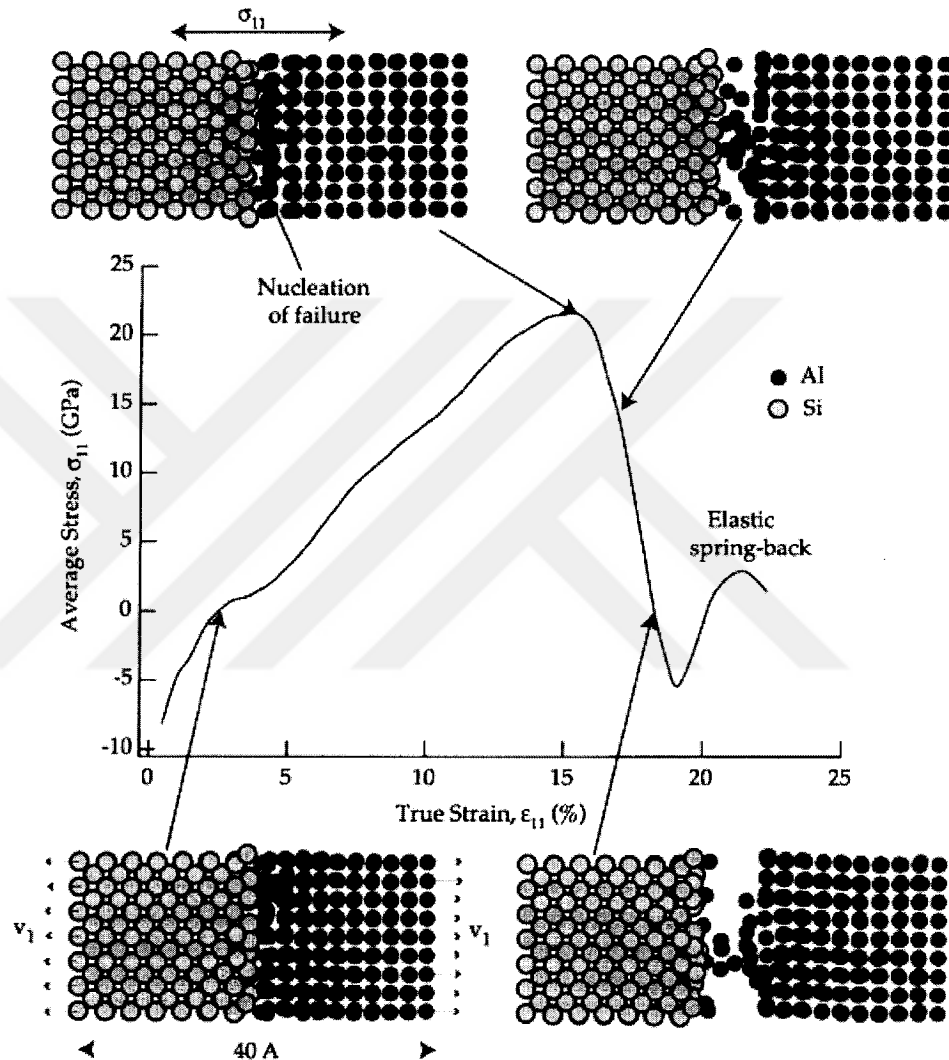
The interface is clearly incoherent and possesses a rippled appearance, i.e. some atoms are displaced towards a perfect interface plane and some are displaced away. The rippled appearance is caused by the strong interaction of neighboring Al and Si atoms located in the two different crystal lattice structures. If a Si or Al atom near the interface sees a void in the adjacent material, the atom will be drawn toward that void. Conversely, if a Si or Al atom near the interface is placed directly next to an atom in the adjacent material, the atom will be pushed away from that atom.

Fig. 5.2 shows the response of the interface model to applied far-field velocity boundary conditions and the center figure is a plot of the average uniaxial stress versus the true uniaxial strain. The average stress is calculated using Eq. (6.8) for the entire aggregate of atoms, while the true strain is determined from Eq. (6.10). The average axial stress in the model is compressive (negative) for the initial application of the end velocities caused by the attempted contraction of the Al and Si due to the presence of the free surfaces. Then, the average axial stresses become tensile, and the stresses continue increasing until a critical stress level is reached. At this level, the failure of the interface between the Al and the Si atoms begins to nucleate. The interfacial failure starts at the location where the Al and Si atoms are displaced (rippled) in the relaxed and undeformed

state. Actually, one of the reasons that the interface is weak compared to the pristine bulk material is the rippled nature of the interface. This property makes local stress concentrations and failure through local damage nucleation. As the interface debonds, the average stresses in the model decrease over a finite strain increment. Then, the average stress in the block reaches approximately 0 GPa, the interfacial separation is complete and several Al atoms are still attached to the Si. After this, the two blocks undergo elastic springback as indicated in Fig. 5.1. In this study, the predicted debonding stress levels is around 20 GPa and the ultimate tensile strength is around 200 MPa [49,50]. The high attainable stress levels are caused by the defect and impurity free crystal structure of the interface, relatively thin and periodic nature of the interface model, and the dynamic loading conditions. Another reason for this is the size scale effect, which is the basis of strain gradient plasticity. The size scale effect will also cause the local stresses to be much higher than experimental observations on large scale samples [51].

To check whether the results do not have a strong sensitivity to the boundary velocity conditions or periodic lengths in the transverse directions, several MEAM interface models were deformed under varying conditions. Fig. 5.2 shows the average-stress versus true-strain response of the MEAM interface models to the selected conditions. These simulations showed that applying a velocity at both ends versus fixing one end and moving the other has no effect on the model response. They also showed that applying a velocity exclusively to the end atoms creates conditions for the propagation of an elastic shock wave and this can be eliminated by giving the atoms within the model a spatially linear initial velocity distribution with a zero value at the interface and the same maximum value at the displaced far-field end. Relaxing the interface through a static

calculation at 0 K, before applying the external boundary velocities, showed that the interface quickly reaches an equivalent deformed state under the imposed boundary velocities as evidenced from the similarity in the stress–strain responses in Fig. 5.2.



**Fig. 5.1** Representative average-stress versus true-strain response of the  $[100]_{\text{Si}}|[100]_{\text{Al}}$  interface model to boundary velocities,  $v_1$ , at the far ends of the blocks in the  $[100]$  and  $[-100]$  directions. The model is periodic in the  $[010]$  and  $[001]$  directions [16].

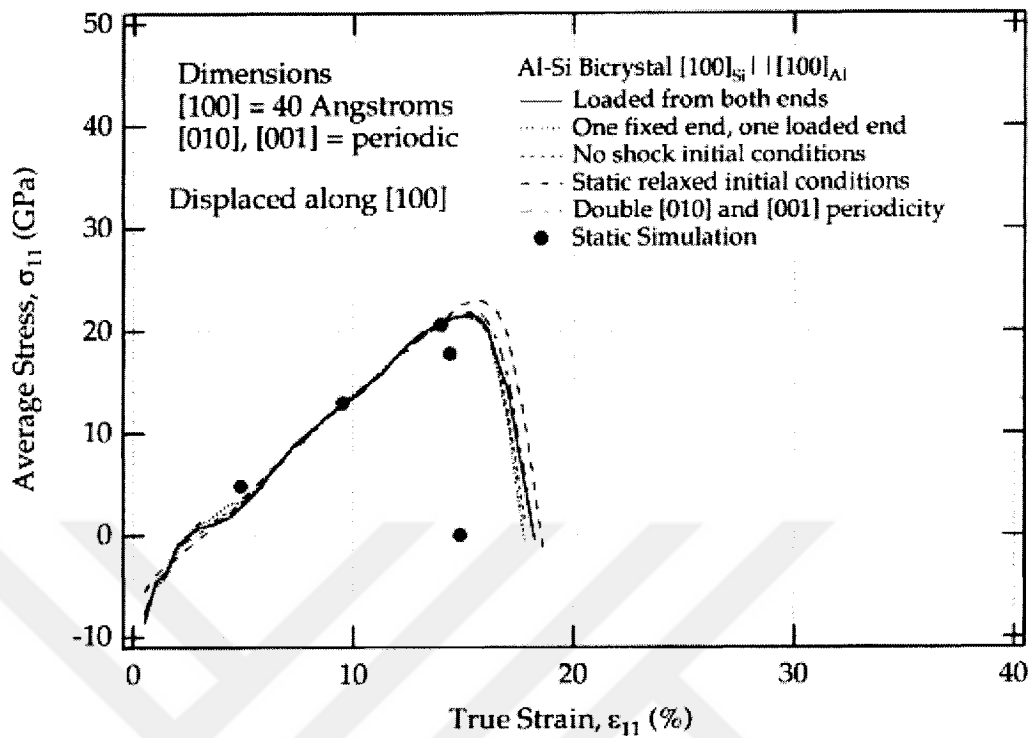


**Fig. 5.2** The average-stress versus true-strain response of the  $[100]_{\text{Si}}||[100]_{\text{Al}}$  interface model under various conditions. The model is periodic in the  $[010]$  and  $[001]$  directions [16].

As can be seen from Fig. 5.2, the response of the model under static and dynamic conditions is essentially the same. Finally, periodic lengths along the  $[010]$  and  $[001]$  directions were doubled, and this had a negligible effect on the predicted stress-strain response (initially four aluminum unit cells and three silicon unit cells, i.e.  $16.2 \text{ \AA}$ ).

Fig. 5.3 shows the results of the average stress-strain response of the MEAM interface model and equivalent MEAM models containing only silicon or aluminum. Fig. 5.3 also shows that the fracture of the pure silicon is more abrupt compared to the aluminum and the Al-Si interface models. This brittle nature of pure silicon is also observed experimentally. Furthermore, the Al-Si interface is weaker than either the pure

Al or pure Si materials; however the interfacial fracture resembles failure characteristics in pure Al.

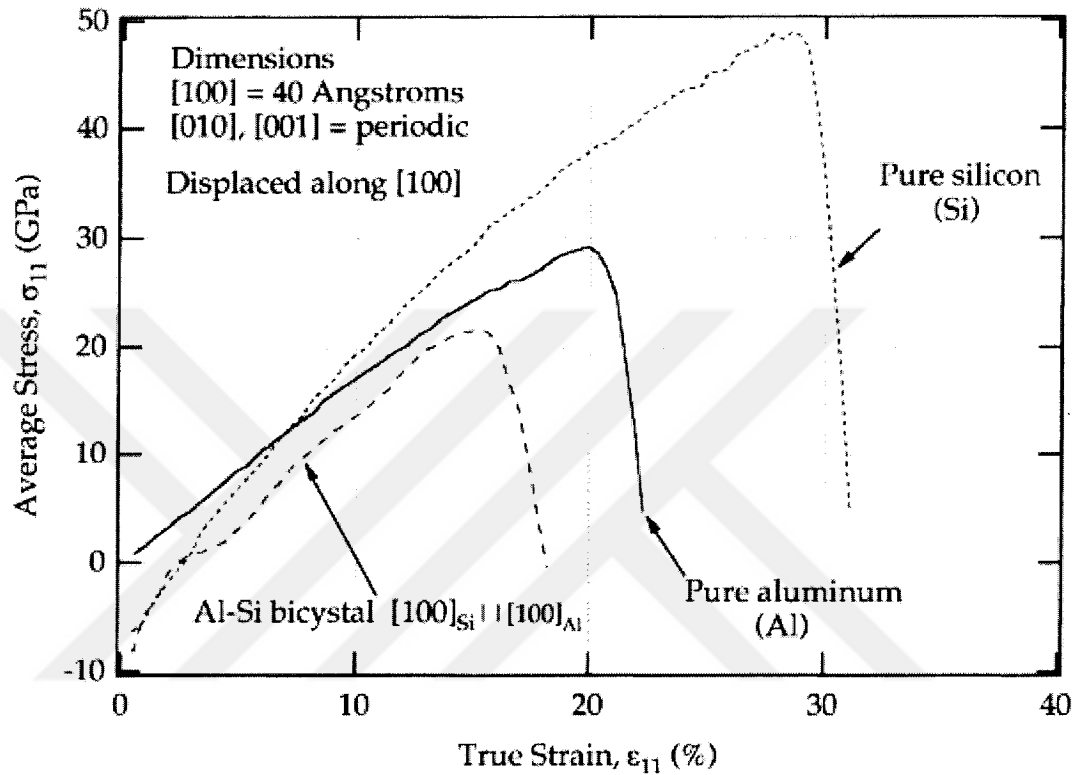


**Fig. 5.3** The average-stress versus true-strain response of the  $[100]_{\text{Si}}|[100]_{\text{Al}}$  interface model compared to pure silicon and aluminum MEAM models with the same dimensions loaded under identical conditions. All three models are periodic in the  $[010]$  and  $[001]$  directions [16].

Fig. 5.4 shows the following: (a) the average-stress versus true strain response; (b) the average-stress versus far-field displacement response; and (c) the average-stress versus local displacement response of the MEAM interface model with four different block sizes. The block sizes are 10Å, 20Å, 40Å and 80Å, and the sizes here indicate the

entire model length. The respective MEAM models are used to calculate the far-field opening displacements and true strains from the velocities at the far ends. The local opening displacements are calculated as the displacement difference during the simulation between the atomic planes initially at  $\pm 3$  planes (approximately  $\pm 5\text{\AA}$ ) from the interface.

The results in Fig. 5.4a indicate that the average stress–strain response exhibits a relatively strong dependence on the block size in the [100] direction and converges since the interaction of the interface atoms with the displaced surface atoms diminishes. Because of the localization phenomenon, the average stress–strain response is not the most appropriate approach for studying the interface debonding. Therefore stress versus displacement curves are plotted in Fig. 5.4b and Fig. 5.4c. As the block size is increased, the average-stress versus far-field displacement response in Fig. 5.4b diverges since the applied end displacement is dispersed over a larger MEAM model length. However, Fig. 5.4c illustrates the average-stress versus local-displacement curves are far less sensitive to the block size. The most suitable block size for MEAM modeling is one that minimizes the interaction between the displaced far-field surfaces and the interface atoms. Fig. 5.4a shows that the average-stress versus true-strain response used as a measure of the interaction between the interface atoms and the displaced free surfaces converges towards a nominal response centered at the origin. Based on the curves in Fig. 5.4, the differences in the responses of the 40 and 80 $\text{\AA}$  models are minimal, whereas models below 20 $\text{\AA}$  show significant deviations from the responses of the larger blocks. Due to the excessive computation time for the 80 $\text{\AA}$  model, the 40 $\text{\AA}$  model is the most appropriate for the MEAM simulation of interface debonding for a pristine Al–Si interface.

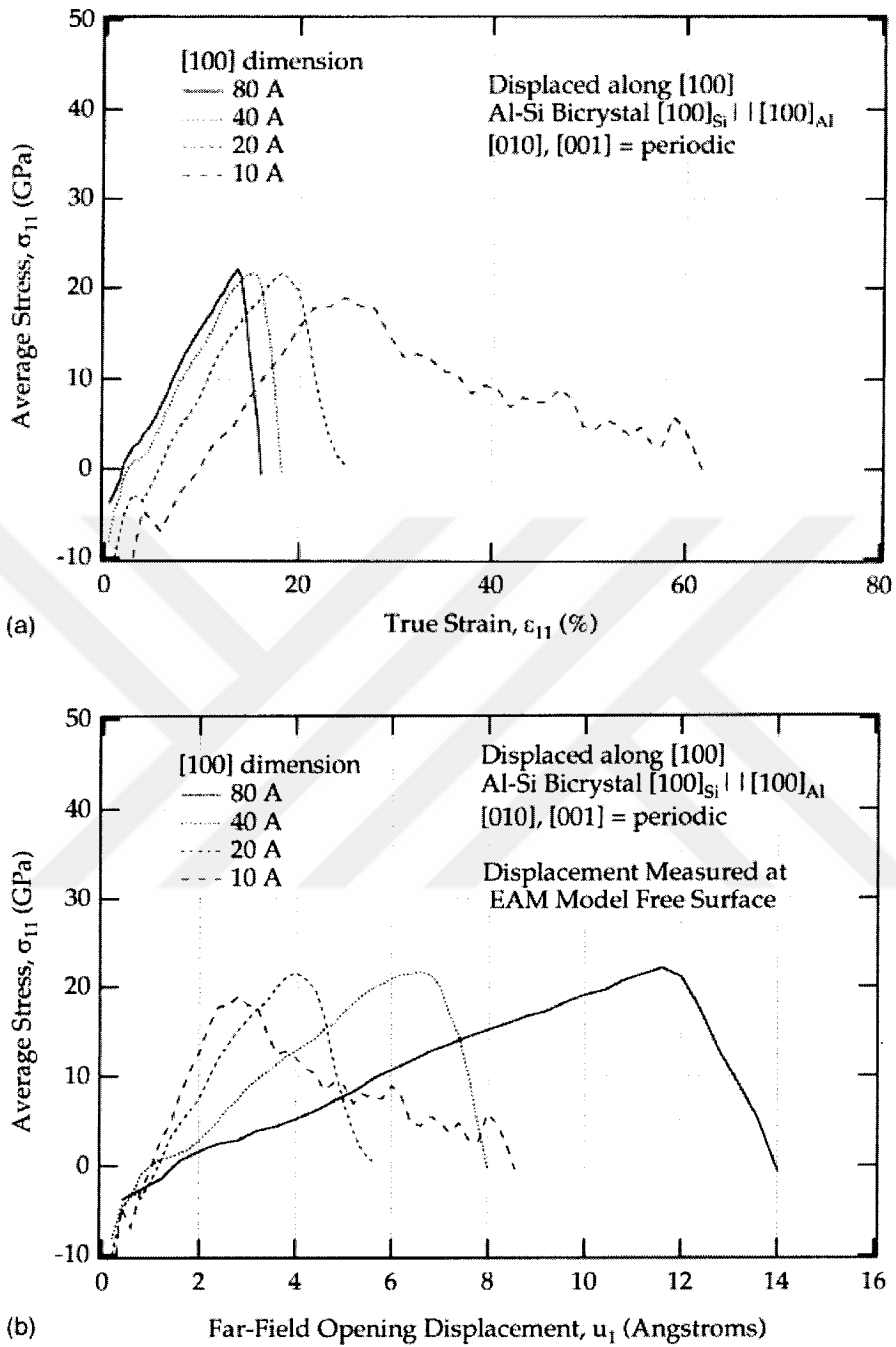


**Fig. 5.4** (a) Average-stress versus true-strain; (b) average-stress versus far-field displacement; and (c) average-stress versus local displacement for the  $[100]_{\text{Si}} || [100]_{\text{Al}}$  interface model for different lengths in the [100] direction. The model is periodic in the [010] and [001] directions [16].

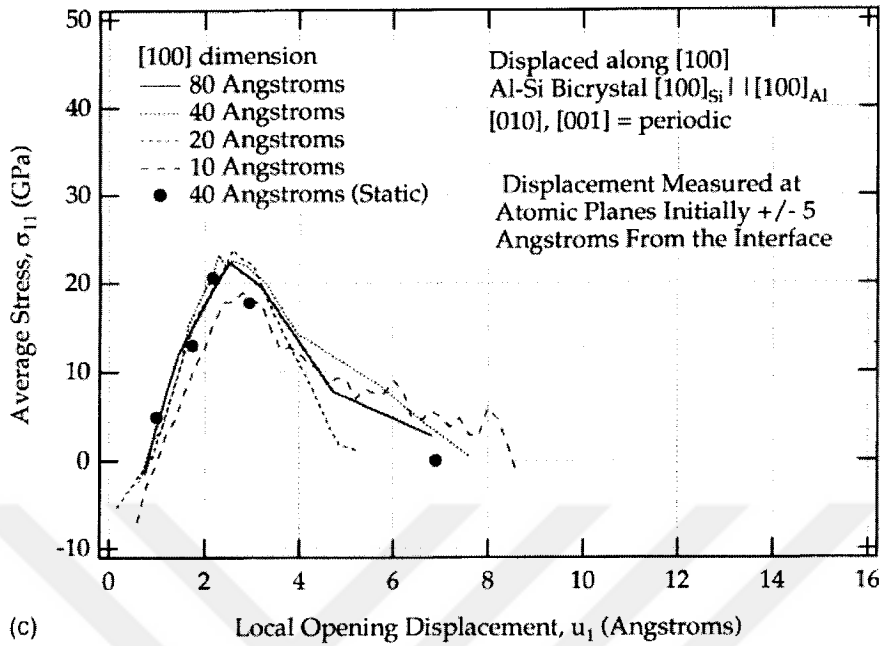


**Fig. 5.4 (Continued)**

Fig. 5.5 illustrates four average stress–strain curves from the 80Å Al–Si interface model. The average stress–strain response is determined by decreasing the bounds systematically. The averaging bounds for the 80Å model in Fig. 5.5 were chosen to match the different MEAM model sizes studied in Fig. 5.4. This study shows that the overall shapes of the curves in Fig. 5.4 are independent of the averaging volume even if the atoms exclusively near the interface are considered. Therefore, the locality in macroscale continuum mechanics is valid even at these size scales when developing an interfacial debonding damage criterion under pure tension. On the other hand, when the averaging volume becomes very small the response demonstrates significant local fluctuations due to the smaller number of atoms sampled. Furthermore, this simulations show that the differences in the curves in Fig. 5.4 cannot be ascribed to differences in the averaging volume for different size.

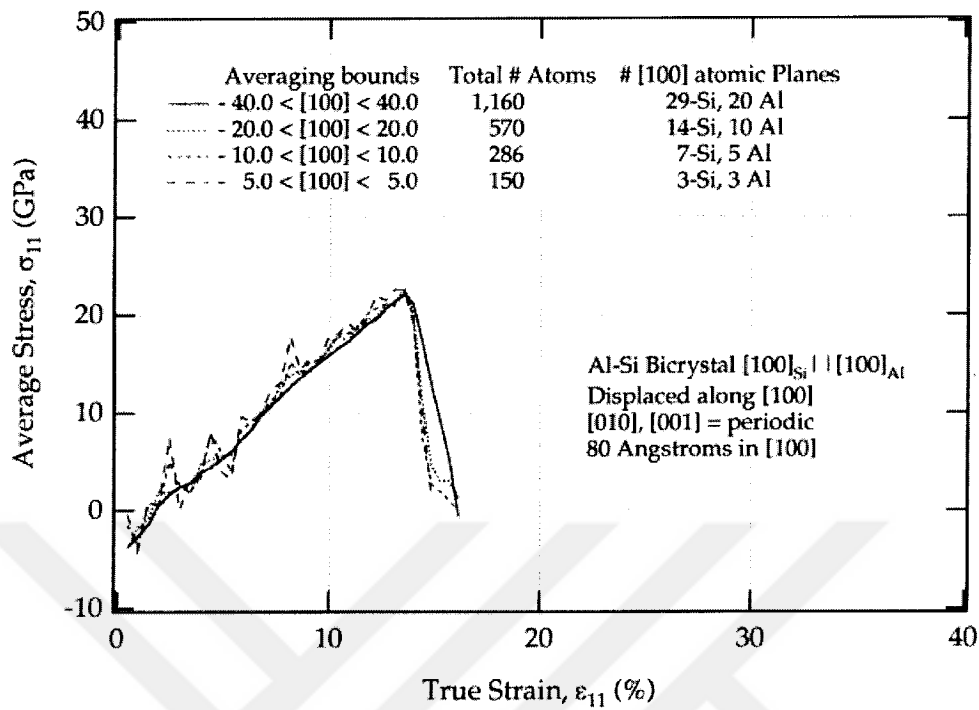


**Fig. 5.5** Effect of averaging volume on the average-stress versus true-strain response of the 80Å [100]<sub>Si</sub>||[100]<sub>Al</sub> interface model. The model is periodic in the [010] and [001] directions [16].

Fig. 5.6 represents a distribution of average uniaxial stresses just before interfacial failure (14% strain in Fig. 5.2). The stress distributions across the interface provide insight into the local failure mechanisms. The stresses were averaged in the [010] and [001] directions and the average stress in the entire volume is also indicated in Fig. 5.6 as a straight line. Furthermore, Fig. 5.6 shows the distributions predicted by both the molecular dynamics and static simulations. Very close to the interface, the stresses in both materials are higher than the nominal values away from the interface, under both static and dynamic loading conditions. The rippled nature of the interface causes the magnification of stresses. In other words, some atoms cannot interact strongly with immediate neighbors across the interface due to the different crystal structures and lattice

parameters of the two phases. The low interaction force levels between certain atoms promote high forces between other atoms which are attempting to keep the interface intact. Thus, extremely close to the interface, several atoms are equilibrated under relatively higher forces. This microscopic disturbance of stresses near the interface facilitates the nucleation and propagation of debonding failure.

They also investigated the role of vacancy type defects on interface debonding. The point vacancy defects in the simulations are distributed randomly throughout the two atomic planes adjacent to the interface in: (a) just the Al; (b) just the Si; and (c) both the Al and Si. In all three situations the vacancy defects at the interface lowers the fracture strength of the interface. Then, they studied the role of microscopic crack-like defects in the bulk materials on the competing mechanisms of fracture in the pure Al, pure Si, or at the Al-Si interface. Before simulations, atomic rows along the [001] direction were removed to create a crack-like vacancy defect in the silicon or aluminum. As the initial flaw size is increased in both materials, failure in the pure materials is favored over interfacial failure. When the flaw area projected onto a plane normal to the tensile axis is nearly 30%, flaws in the Si distract the failure from occurring at the interface. Flaws in the Al are even less effective since it takes a larger flaw area projected on a plane normal to the tensile axis (about 50%) to accomplish bulk failure in the Al versus the interface.

Finally the continuum based model was compared with the atomistic simulations. Continuum-based decohesion models use a traction versus opening-displacement relationship dictated by closed-form equations. There are several different versions of the equations used by Needleman [32-34], and Tvergaard and Hutchinson [52]. The equations of Needleman are given below:

$$\frac{\sigma_{11}}{\sigma_{\max}} = \frac{27}{4} \frac{u_1}{u_{\max}} \left[ 1 - \frac{u_1}{u_{\max}} \right]^2 \quad (5.1)$$

$$\frac{\sigma_{11}}{\sigma_{\max}} = 13.136 \frac{u_1}{u_{\max}} \exp \left[ -4.833 \frac{u_1}{u_{\max}} \right] \quad (5.2)$$

where  $\sigma_{11}$  and  $\sigma_{\max}$  are the instantaneous traction normal to the interface and the maximum traction normal to the interface, respectively. Similarly,  $u_1$  and  $u_{\max}$  are the instantaneous normal opening displacement and maximum normal opening displacement, respectively. The pure normal traction forms are used for comparison to the present MEAM results ignoring the coupling to shear stresses across the interface [32-34] between Eqs. (5.1) and (5.2). When  $u_1$  approaches  $u_{\max}$ ,  $\sigma_{11}$  approaches zero and the interface is considered to be separated. Fig. 5.7b also illustrates the model of Tvergaard and Hutchinson [52] uses a tri-linear approximation with similar  $\sigma_{\max}$  and  $u_{\max}$  parameters and their model also includes adjustable shape parameters which alter the positions of the intercepts between the stress plateau at  $\sigma_{\max}$  and the loading and unloading lines. Furthermore, Fig. 5.7b represents the graphical versions of Eqs. (5.1) and (5.2). The adjustable shape parameters in the linear model have been chosen to fit one of the MEAM results. In Fig. 5.7b, three traction versus displacement relationships from the 40A° MEAM simulations are included and Fig. 5.7a indicates the locations of the different reference planes for the measurement of the model displacements. They calculated the displacements during the simulation by averaging the difference between the positions of the atoms initially in corresponding planes indicated in Fig. 5.7a. When the relative opening displacement is measured from reference planes farther from the interface, the simulations predict that the location of the stress drop is shifted to a larger

normalized displacement value. However, in the end, the interface failure is governed by individual atomic separations through a cohesive type relationship.

Whereas the opening displacement is measured farther from the interface, the stretching of the bulk materials away from the interface is the reason for a significant fraction of the total displacement. Fig. 5.7b demonstrates that the location of the stress peak on the normalized displacement axis is shifted to a larger normalized displacement. The MEAM results using opening displacements near  $\sim 10 \text{ \AA}$  of the interface demonstrate strong quantitative agreement with all continuum-based traction–displacement relationships.

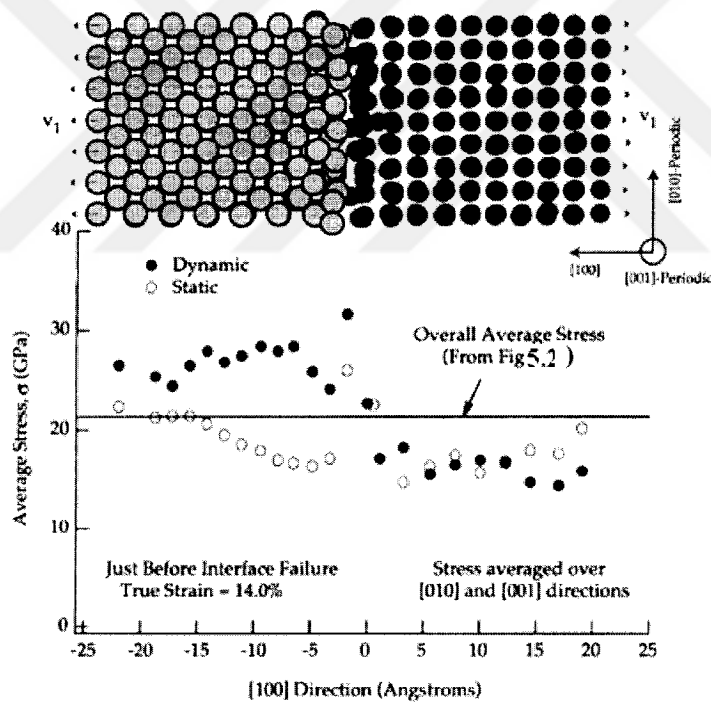


**Fig. 5.6** Stress distribution along the [100] direction for the [100]Si|[100]Al interface model. The atomistic image corresponds directly to the different positions indicated along the lower axis of the plot. The model is periodic in the [010] and [001] directions and the stresses are averaged in these directions [16].

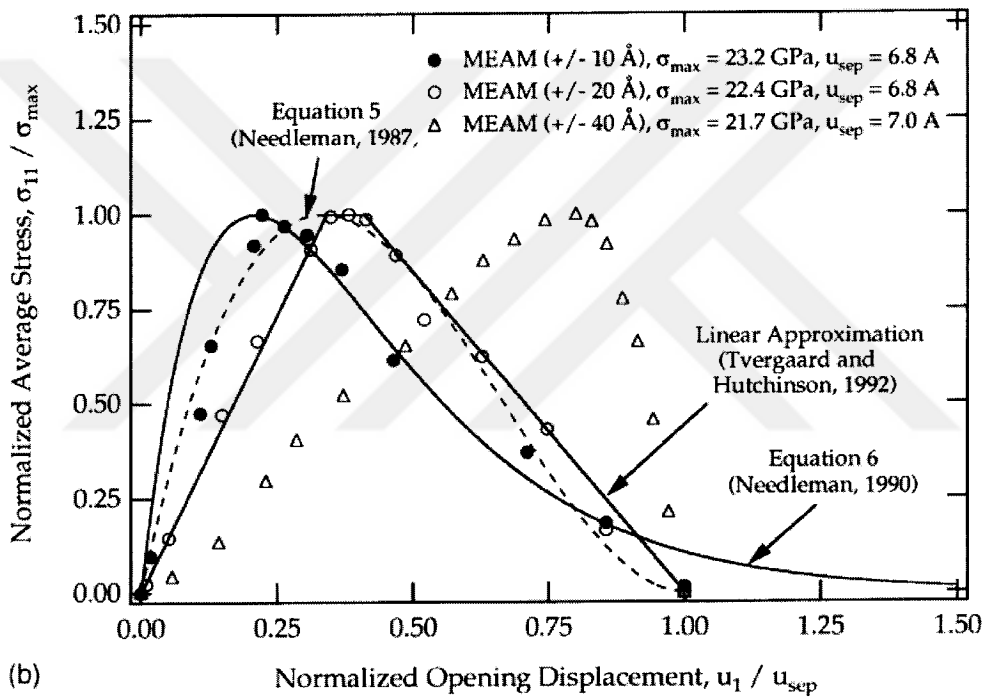
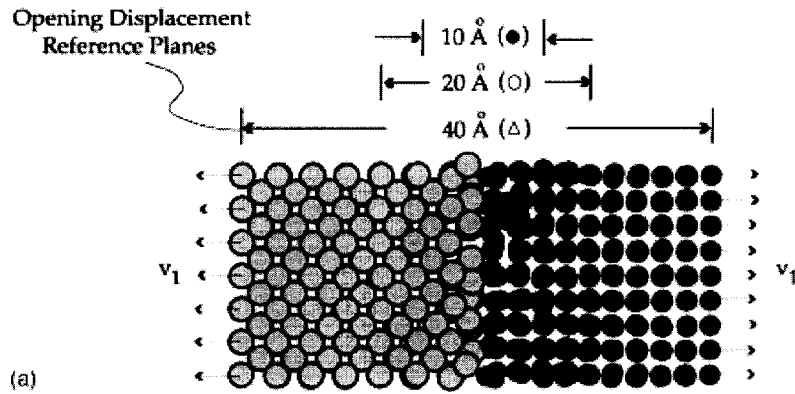


**Fig. 5.7** (a) Schematic of the three different reference planes used to calculate the opening displacement in the MEAM simulations. (b) Traction–displacement curves for the 40 Å MEAM model and different continuum-based cohesive laws [16].

### 5.3 An Analysis of Decohesion along an Imperfect Interface

In order to analyze interface decohesion phenomena, Needleman [34], made a theoretical study, which describes the evolution from initial debonding through complete separation and subsequent void growth. He used a finite strain, cohesive zone type

interface model and formulated the constitutive relations that are specified independently for the materials and the interface. The constitutive equation proposed can be described as with increasing interfacial separation, the traction across the interface reaches a maximum, decreases and eventually vanishes, letting complete decohesion to occur. In this formulation a characteristic length is introduced for dimensional considerations, so that the mechanical response of the interface can be specified in terms of both a critical interfacial strength and the work of separation per unit area. Therefore this model leads to the prediction of interfacial decohesion without the necessity of introducing some additional failure criterion.

An imperfect interface that considers the specific boundary value problem with the plane strain deformation of an elastic-viscoplastic block on a rigid substrate subject to overall uniaxial straining was investigated. The interfacial strength vanishes over one segment of the interface and then increases abruptly, but smoothly, to a prescribed value along the bond line to make the imperfection. The interface is elastic and characterized by a potential [32]. The boundary value problem formulation contains a characteristic length and the course of decohesion depends on the size of the block (and imperfection) relative to this characteristic length. The interface model differs from traditional cohesive zone models in several significant respects; full account is taken of finite geometry changes and the interfacial constitutive relation is specified along the entire interface that is no cohesive zone size needs to be determined by the analysis.

Needleman [32], in 1987, described the interface based on the continuum model for interfacial decohesion. Here, he defined an interface supporting a nominal traction

field  $\mathbf{T}$  which has both normal and shearing components. The displacement of a matrix material point initially along the interface is written as:

$$u_n = \mathbf{n} \cdot \mathbf{u}, \quad u_t = \mathbf{t} \cdot \mathbf{u} \quad (5.3)$$

and

$$T_n = \mathbf{n} \cdot \mathbf{T}, \quad T_t = \mathbf{t} \cdot \mathbf{T} \quad (5.4)$$

where  $\mathbf{n}$  is a unit normal vector parallel to the  $x^2$ -direction and  $\mathbf{t}$  is a unit tangent vector parallel to the  $x^1$ -direction.

An elastic constitutive relation is defined for the interface from a potential that depends only on the displacement difference across the interface and the rigid substrate is restricted from undergoing a rigid body motion so that  $u_n$ , and  $u_t$  are components of the displacement difference across the interface. Positive  $u$  is for an increasing interfacial separation and negative  $u$  is for a decreasing interfacial separation. To complete separation, first, the magnitude of the tractions increases, achieves a maximum and then falls to zero. He constructed a potential which exhibits this behaviour in the form:

$$\begin{aligned} \phi(u_n, u_t) = & \frac{27}{4} \sigma_{\max} \delta \left\{ \frac{1}{2} \left( \frac{u_n}{\delta} \right)^2 \left[ 1 - \frac{4}{3} \left( \frac{u_n}{\delta} \right) + \frac{1}{2} \left( \frac{u_n}{\delta} \right)^2 \right] \right. \\ & \left. + \frac{1}{2} \alpha \left( \frac{u_t}{\delta} \right)^2 \left[ 1 - 2 \left( \frac{u_n}{\delta} \right) + \left( \frac{u_n}{\delta} \right)^2 \right] \right\} \end{aligned} \quad (5.5)$$

For  $u_n \leq \delta$ , where  $\sigma_{\max}$  is the maximum traction carried by the interface undergoing a purely normal separation ( $u_t = 0$ ),  $\delta$  is a characteristic length and  $\alpha$  specifies the ratio of shear to normal stiffness of the interface. When  $u_n > \delta$ ,  $\phi \equiv \phi_{sep}$ , where  $\phi_{sep}$  is the work of separation.

The interfacial tractions are obtained from (5.5) through  $T_n = -\partial\phi / \partial u_n$  and  $T_t = -\partial\phi / \partial u_t$ , to give

$$T_n = \frac{-27}{4} \sigma_{\max} \left\{ \left( \frac{u_n}{\delta} \right) \left[ 1 - 2 \left( \frac{u_n}{\delta} \right) + \left( \frac{u_n}{\delta} \right)^2 \right] + \alpha \left( \frac{u_t}{\delta} \right)^2 \left[ \left( \frac{u_n}{\delta} \right) - 1 \right] \right\} \quad (5.6)$$

$$T_t = \frac{-27}{4} \sigma_{\max} \left\{ \alpha \left( \frac{u_t}{\delta} \right) \left[ 1 - 2 \left( \frac{u_n}{\delta} \right) + \left( \frac{u_n}{\delta} \right)^2 \right] \right\} \quad (5.7)$$

for  $u_n \leq \delta$  and  $T_n \equiv T_t \equiv 0$  when  $u_n > \delta$ .

The work of separation is independent of the separation path due to the existence of a potential. It is given by:

$$\phi_{sep} = \frac{9}{16} \sigma_{\max} \delta \quad (5.8)$$

The exponential potential is specified only for the case of purely normal separation.

Using the same linear shear dependence as in (5.5) and taking  $\phi(0,0) = 0$  with  $\phi \rightarrow \phi_{sep}$

as  $u_n \rightarrow \infty$  the exponential potential can be written in the form

$$\phi(u_n, u_t) = \frac{9}{16} \sigma_{\max} \delta \left\{ 1 - \left[ 1 + z \left( \frac{u_n}{\delta} \right) - \frac{1}{2} \alpha z^2 \left( \frac{u_t}{\delta} \right)^2 \right] \exp \left[ -z \left( \frac{u_n}{\delta} \right) \right] \right\} \quad (5.9)$$

where  $z = 16e/9$ , with  $e = \exp(1)$ .

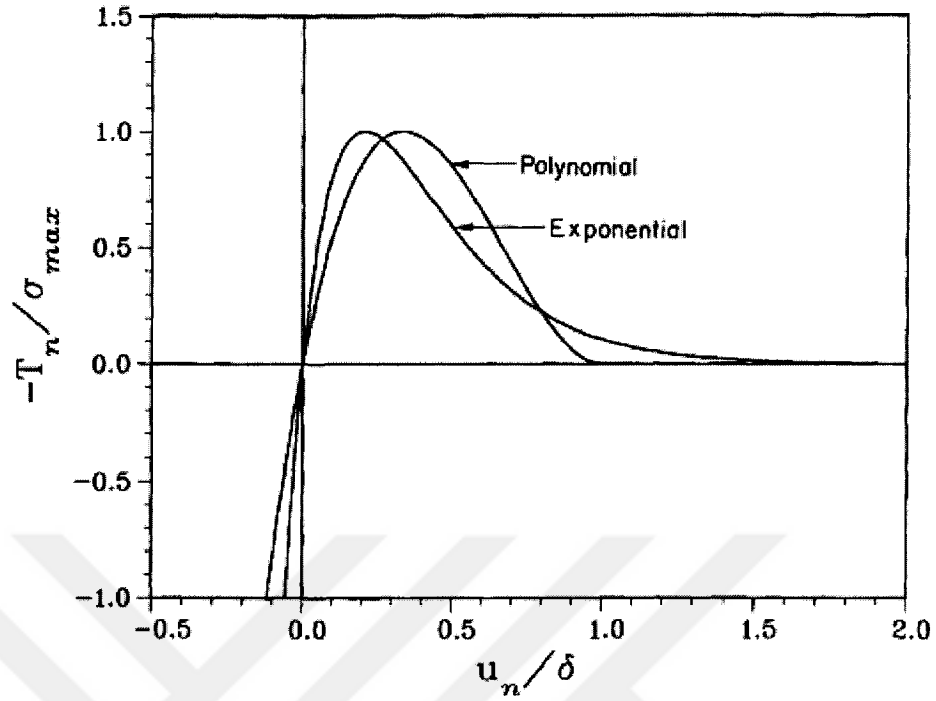


**Fig. 5.8** Normal traction across the interface as a function of  $u$ , with  $u_t = 0$  for both the polynomial potential (5.5) and the exponential potential (5.9) [34].

$$T_n = -\sigma_{max} e^{\left\{ z \left( \frac{u_n}{\delta} \right) - \frac{1}{2} \alpha z^2 \left( \frac{u_t}{\delta} \right)^2 \right\}} \exp \left[ -z \left( \frac{u_n}{\delta} \right) \right] \quad (5.10)$$

$$T_t = -\sigma_{max} e^{\left\{ \alpha z \left( \frac{u_t}{\delta} \right) \right\}} \exp \left[ -z \left( \frac{u_n}{\delta} \right) \right] \quad (5.11)$$

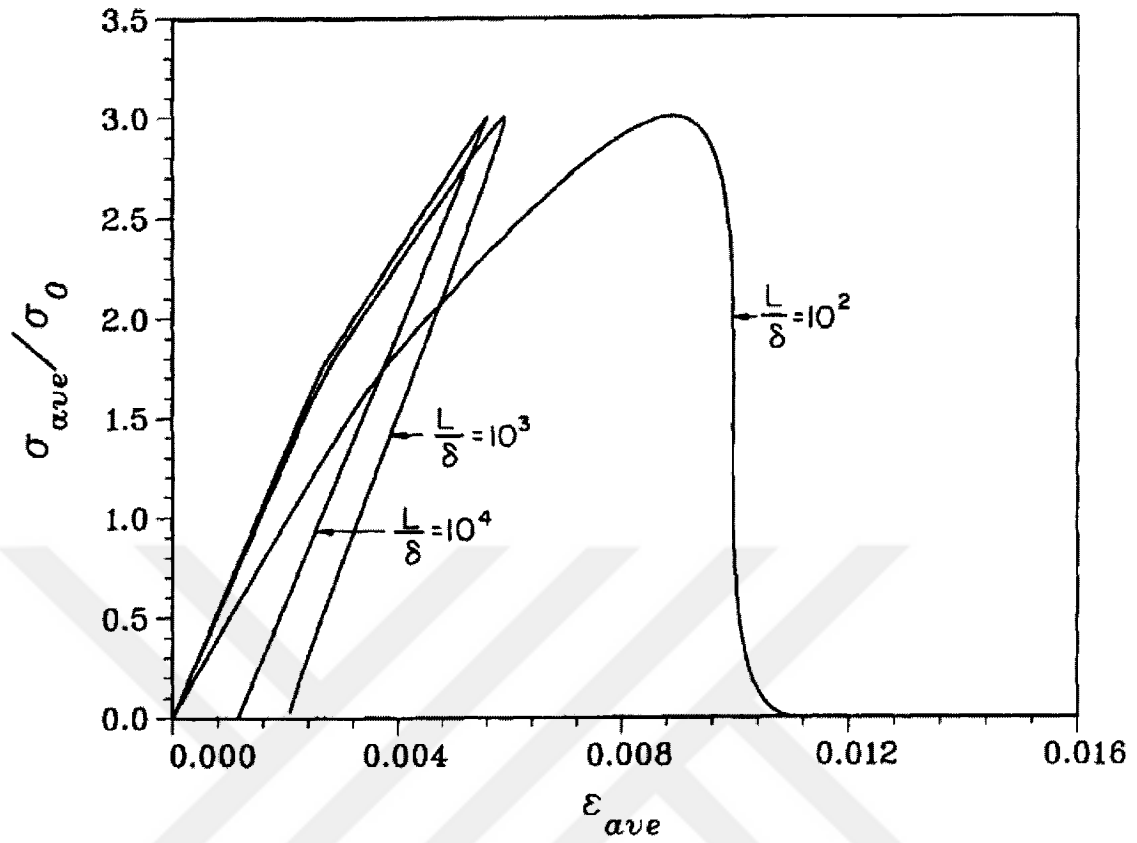
The parameters characterizing the exponential potential are chosen so that  $\phi_{sep}$  is given by (5.8) and the maximum absolute value of  $T_n$ , for purely normal separation is  $\sigma_{max}$ .

Fig. 5.8 shows the normal traction across the interface,  $T_n$  as a function of  $u_n$ , with  $u_t \equiv 0$  for both the polynomial and exponential potentials. The polynomial potential causes separation at  $u_n = \delta$  so that  $T_n = 0$  for  $u_n \geq \delta$ . However, the exponential potential gives a continually decaying normal traction that only vanishes in the limit  $u_n \rightarrow \infty$ . However, the work done between  $u_n = 0$  and  $u_n = \delta$  is about  $0.95 \phi_{sep}$ .

Decohesion of perfect block was studied and for  $L/\delta = 10^2$ , (L is the specimen dimension) decohesion takes place in a ductile manner, although on the falling side of the stress strain curve, the average strain reaches a local maximum at 0.0096 and decreases slightly before increasing again. On the other hand for  $L/\delta = 10^3$  and  $L/\delta = 10^4$ , decohesion takes place in a "brittle" manner and there is no explicit unloading behaviour for the viscoplastic constitutive relation employed (Fig. 5.9)

In conclusion, the interface model provides a unified framework for analyzing the initiation and development of decohesion along interfaces without the necessity of introducing some additional failure criterion.

These two research papers allow understanding some aspects of the interfaces, but it is still necessary to understand how the continuum-based traction versus displacement laws compares with the MD simulations. These studies provide a direct comparison between the predictions of atomistic simulations and the continuum models. Furthermore, the predictions of atomistic simulations motivate the use of such continuum approaches and help to quantify their range of applicability.



**Fig. 5.9** Stress-strain curves for a perfect interface,  $a/L = 0$ , for various values of  $L/\delta$  using the polynomial potential (5.5). The remaining interface parameters and the material properties are specified in the text [34].

## CHAPTER VI

### SIMULATION

#### 6.1 Introduction

In this chapter, simulations that are carried out for this project are explained in detail. The simulations are performed using the AlSi MD program provided by Dr. Stoilov. The original version of the program used the EAM with Lennard-Jones as a pair potential. Then we implemented the MEAM as described in Chapter 4.

The MD simulation was used to model Al-Si near-surface microstructures. The MEAM potential and the Verlet integration algorithm were the two methods used for our solution. The interface was modeled in three-dimensional structure, and MD simulations were carried out using about  $10^4$  atoms. The evolution of the subsurface microstructure of aluminum-silicon system was investigated to develop a constitutive relationship (stress-strain, traction-displacement) for the incoherent aluminum-silicon interfaces.

#### 6.2 Computational Aspects and MEAM Implementation

In this subsection we will show the outlines of an implementation of the MD algorithm with the MEAM.

The Modified Embedded Atom Method (MEAM) potential as defined in Chapter 4 is given by

$$E_{tot} = \sum_i \left[ F_i(\bar{\rho}_i) + \frac{1}{2} \sum_{j \neq i} S_{ij} \phi_{ij}(r_{ij}) \right] \quad (4.14)$$

where the sums are over the atoms  $i$  and  $j$ ,  $r_{ij}$  is the distance between atoms  $i$  and  $j$ , and  $\bar{\rho}_i$  is the host electron density at site  $i$ .  $F_i$  is the embedding function defined as the

required energy to place an atom into the electron environment defined by  $\bar{\rho}_i$ ,  $\phi_{ij}$  is the pair interaction between atoms  $i$  and  $j$ , and  $S_{ij}$  is the screening function.

The force on each atom can be calculated using the following equations:

$$\vec{F}_i = -\vec{\nabla} E_{tot} \quad (4.31)$$

$$\vec{F}_i = -\sum_i \left[ \sum_{m=1}^3 i_m \left( \frac{\partial F_i}{\partial \bar{\rho}_i} \frac{\partial \bar{\rho}_i}{\partial r_{ij}} \frac{\partial r_{ij}}{\partial x_m} + \frac{1}{2} \sum_{j \neq i} \left( S_{ij} \frac{\partial \phi(r_{ij})}{\partial r_{ij}} \frac{\partial r_{ij}}{\partial x_m} \right) \right) \right] \quad (4.32)$$

See Chapter 4 and Appendix A for detailed explanations.

Before starting the implementation of the MEAM, dimensionless units that are used in this program are explained in the following paragraphs.

Dimensional analysis is a mathematical tool used in science and engineering to simplify a problem by reducing the number of variables to the smallest number of basic parameters. Thus dimensional analysis is very valuable to the analysis of a wide range of problems. Dimensional analysis has broad applications. It is also the basis of modeling that helps modelers to establish equations and yield solutions. It plays an essential role for experimentalists from design of experiments to data analysis. It can also be misused, Cheng et al.[53] gives the following recipe for dimensional analysis:

1. Listing independent variables and parameters that the quantity of interest depends on. There should be a relationship for each dependent quantity.
2. Identifying independent variables and parameters with independent dimensions.

3. Forming dimensionless quantities and establishing relationships among dimensionless quantities. The number of relationships is equal to the number of dependent quantities.

There are several methods available for dimensional analysis. The Buckingham  $\pi$  theorem is an important theorem in dimensional analysis. According to this theorem, the functional dependence between a certain number (e.g.  $n$ ) of variables can be reduced by the number (e.g.  $k$ ) of independent dimensions occurring in those variables to give a set of  $p = n - k$  independent, dimensionless numbers. Different systems which share the same description by dimensionless numbers are equivalent. Most importantly, it provides a method for computing sets of dimensionless parameters from the given variables, even if the form of the equation is still unknown. However, the choice of dimensionless parameters is not unique: Buckingham's theorem only provides a way of generating sets of dimensionless parameters, and will not choose the most physically meaningful [53-55].

One of the reasons for using dimensionless units is the ability to work with numerical values that are approximately unity, instead of the extremely small values in the atomic scale. Another reason for using them is that the equations of motion are simplified because some of the parameters defining the model are absorbed into the units [44].

The none-dimensional units used in this study are:

$$\text{Time } \tilde{t} = \frac{t}{\sqrt{\frac{m\sigma^2}{\varepsilon}}} \quad (6.1)$$

$$\text{Length } \tilde{l} = \frac{l}{\sigma} \quad (6.2)$$

$$\text{Energy } \tilde{e} = \frac{e}{\varepsilon} \quad (6.3)$$

$$\text{Velocity } \tilde{V} = \frac{V}{\sqrt{\frac{\varepsilon}{m}}} \quad (6.4)$$

$$\text{Force } \tilde{F} = \frac{F}{\left(\frac{\varepsilon}{\sigma}\right)} \quad (6.5)$$

$$\text{Stress } \tilde{P} = \frac{P}{\left(\frac{\varepsilon}{\sigma^3}\right)} \quad (6.6)$$

The values of the used parameters are:

$$\sigma = 3.4 \text{ \AA},$$

$$m = 6.69 \times 10^{-26} \text{ kg}$$

$$\varepsilon = 1.656 \times 10^{-21} \text{ J}$$

### 6.2.1 Setting Geometry

In this subsection, the geometry settings used in the study are summarized.

Aluminum has a face-centered cubic lattice structure with a lattice constant of 4.05 Å. Fig. 6.1 shows the FCC structure created by Materials Studio software.

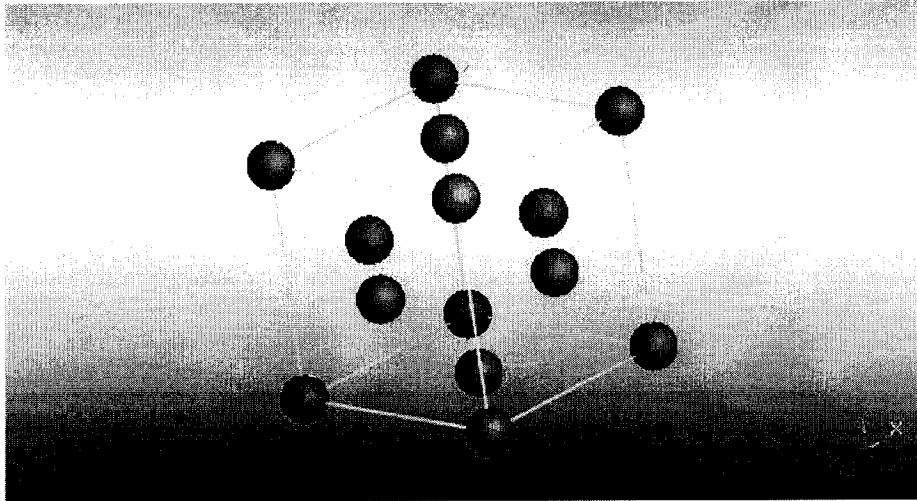


**Fig. 6.1** The Al FCC structure created by Materials Studio software

Silicon has a diamond lattice which consists of two interpenetrating face centered cubic Bravais lattices, displaced along the body diagonal of the cubic cell by one quarter the length of the diagonal. It can be regarded as a face centered cubic lattice with the two-point basis. The lattice constant of a silicon is  $5.4\text{\AA}$  and the conventional cubic cell of the diamond lattice is shown in Fig. 6.2.

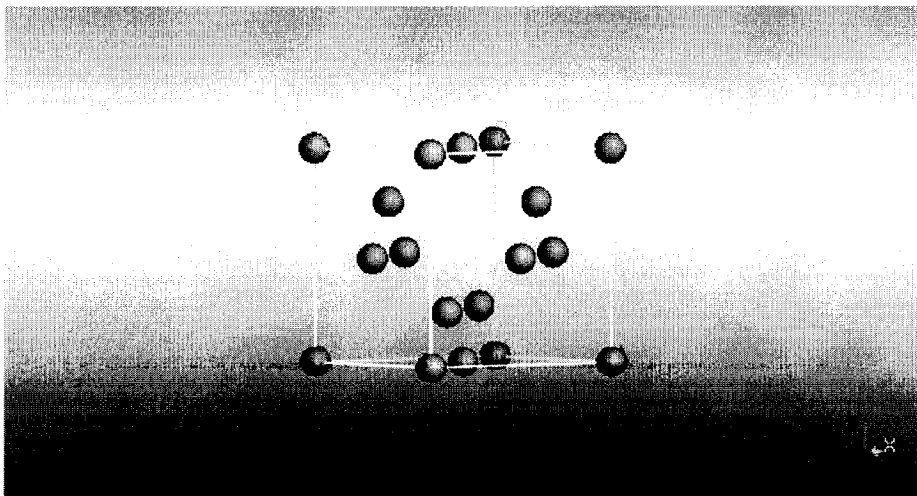
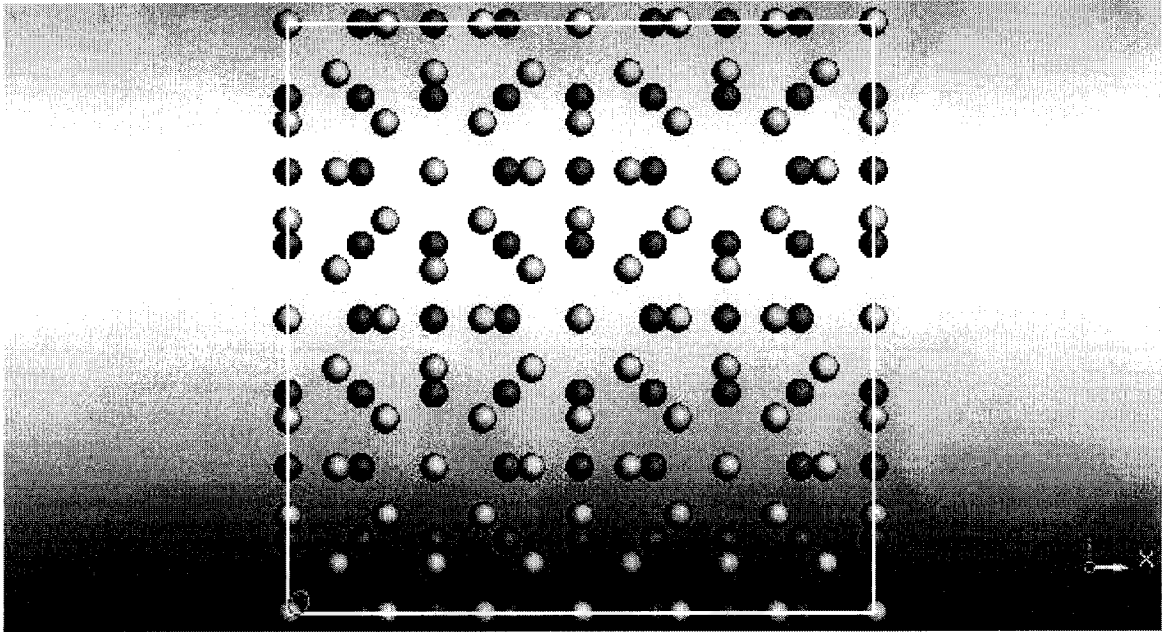
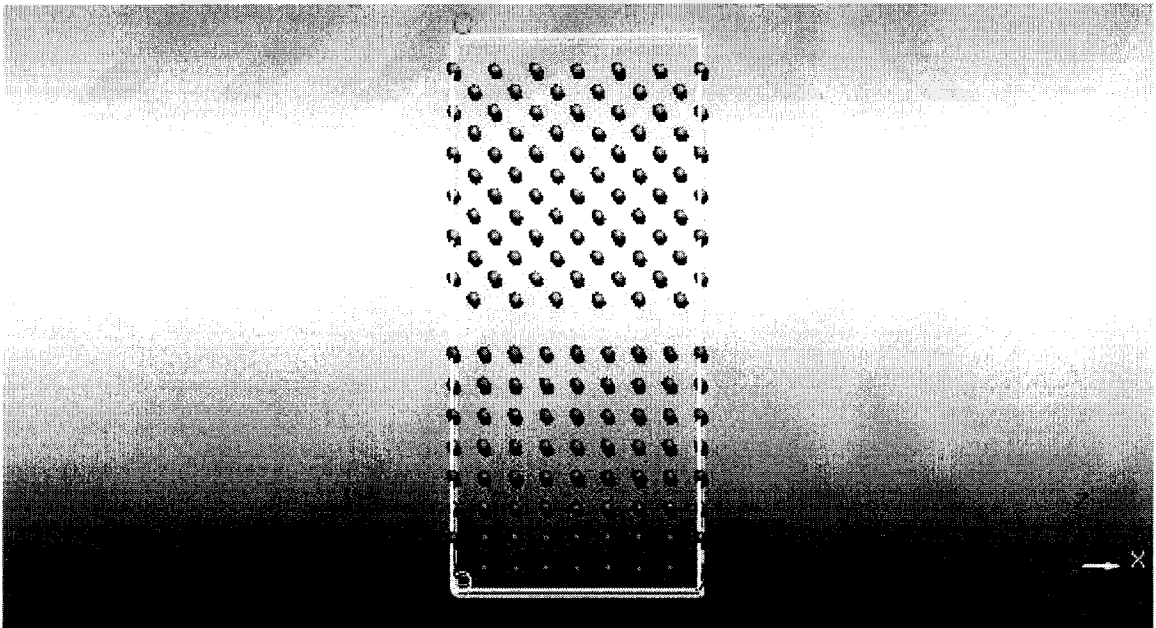


**Fig. 6.2** The Si diamond structure created by Materials Studio software

Three-dimensional figure of the Al-Si interface is given in Fig. 6.3 in.



a)



b)

**Fig. 6.3** Different viewing directions of Al-Si interface created by Materials Studio software.

### 6.2.2 Program Organization

The flow chart of main program of the MD code used in this thesis is given in Fig.

6.4.

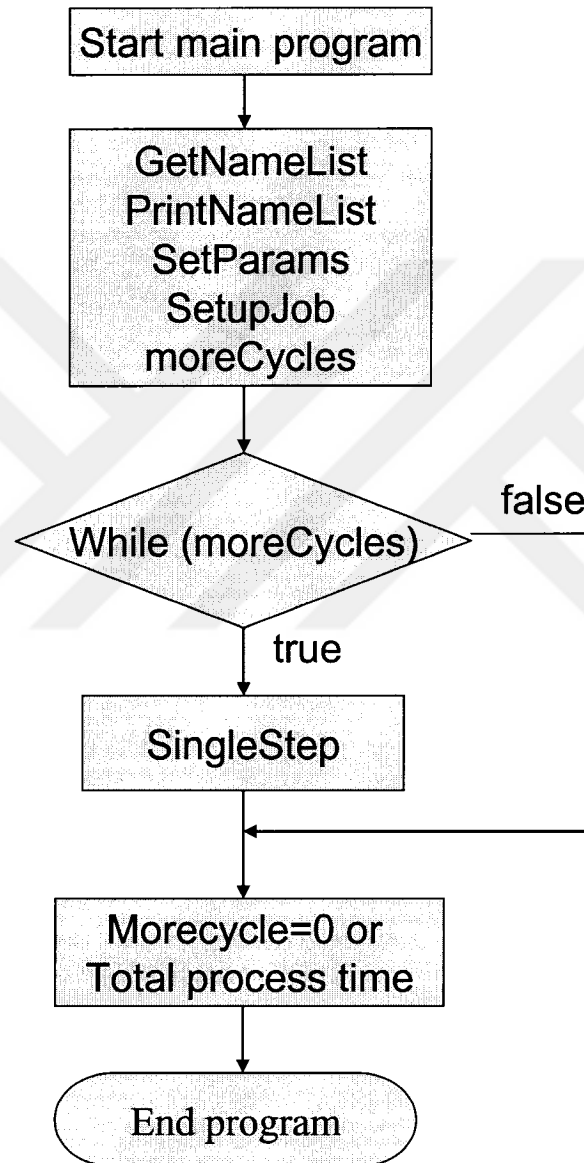


**Fig. 6.4** Flow chart of the main program

*GetNameList*, *SetParams* and *SetupJob* are the initialization phase in which parameters and other data are initialized and storage arrays allocated, the program enters loop. Each loop cycle advances the system by a single time step (*SingleStep*) and the loop terminates when *moreCycles* is set to zero or the total processing time exceeds a preset limit.

The variables required for the simulation are set by the function *SetParams* such as cutoff radius, and initial cell dimensions.

All the work needed for initializing the simulation is done by the function *SetupJob*. Initial atomic coordinates, velocities and accelerations are initialized by this function. Here, a fcc lattice cell is used for Al and diamond lattice cell for Si and the system is centered about the origin. The initial velocities are set to a fixed magnitude that depends on the temperature and after assigning random velocity directions the velocities are adjusted to ensure that the center of mass is stationary. The accelerations are initialized to zero.

*Singlestep* is the function that handles the processing for a single time step, including calls to the functions that deal with the force evaluation, integration of the equation of motion, adjustments required by periodic boundaries and property measurements. The flow chart of this function is shown in Fig. 6.5. As explained in Chapter 3, Verlet algorithm is used on the integration of the equation of motion and the periodic boundary conditions are applied. The MEAM potential summarized in Chapter 4 is used to calculate the forces on each atom (*ComputeForces*)

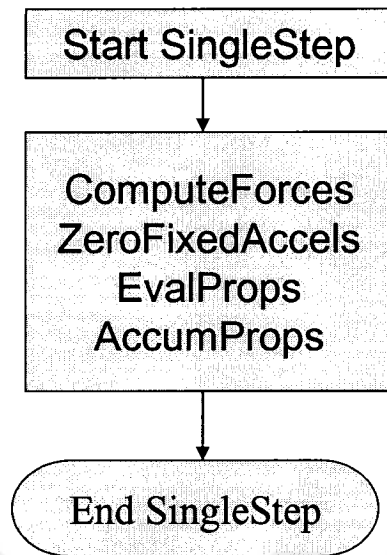


**Fig. 6.5** Flow chart of the SingleStep function

The input parameters are in non-dimensional values and can be characterized as follows:

deltaT - time step

rTopWallVel - velocity of the top wall

nebrTabFac - maximum number of closest neighbors (needed to reserve adequate amount of memory)

nMolWallTop - the width (in number of atomic layers) of the top wall

nMolWallBot - the width (in number of atomic layers) of the bottom wall

rNormalStress - normal stress applied to the top wall

rShearStress - shear stress applied to the top wall

rNebrShell - cutoff radius

runId - current run ID number

- stepAvg - number of time step after which the global variables are averaged
- stepLimit - maximum number of time steps
- stepSnap - frequency of recording the computed data

The values of the input parameters can be modified within an input file. The program allows the modification of the thickness of the top and bottom walls through the parameters nMolWallTop and nMolWallBot. The relative velocity, the normal and tangential stresses of the top wall can be varied by changing the magnitudes of rTopWallVel, rNormalStress and rShearStress.

After a successful run, the program generates two output files: The first one contains the evolution of the coordinates, velocities and the acceleration of each atom/molecule in the system that are recorded by interval determined by stepSnap (in the input file). The second file contains information for the system (current time, kinetic energy, number of atoms) at times determined by stepAvg.

In order to visualize the evolution of the atomic system “POV-Ray” software is used. Running the results within POV environment creates 3D snap shots of the current atomic configuration and saves them as consecutive bmp files. Then these bmp picture files are assembled in a movie using GIF Construction Set Professional software. Materials Studio program by Accelrys is also used for visualizing the structure of Al and Si and the interface.

### 6.3 Al-Si Interface and Parameters

In our MD simulations, we consider the following steps shown in Fig. 6.6:

1. An AlSi interface for FCC Al and diamond cubic silicon blocks that are aligned long  $[100]_{Al}||[100]_{Si}$ .

2. The normal vector at the interface is normal to the  $[100]_{\text{Al}}$ . The model is periodic in the  $[010]_{\text{Al}}$  direction.
3. The top Si plane farthest from interface has been displaced with constant velocity between  $0.1\text{-}0.9\text{\AA}/\text{ps}$  in the direction parallel to the interface.
4. The bottom Al plane is immobilized.
5. Local shear stress at the interface has been determined as a function of the  $[010]$  displacement.

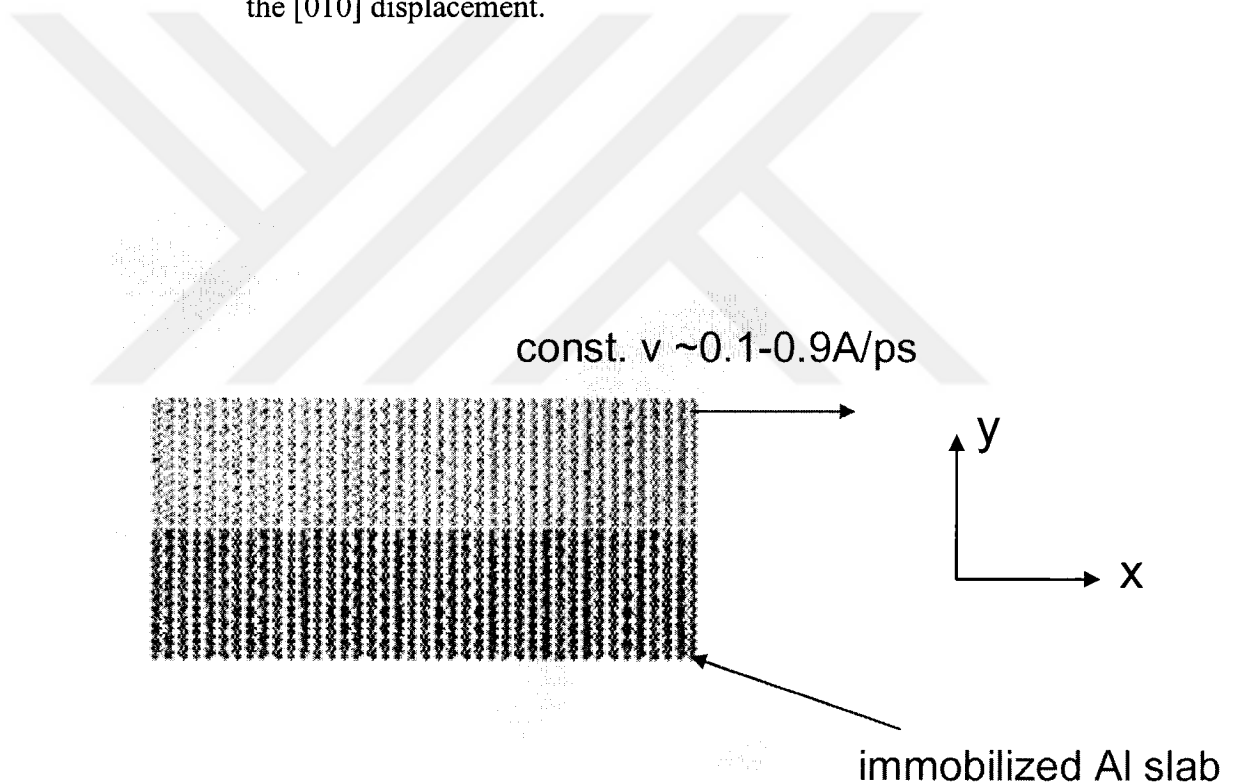


**Fig. 6.6** Al-Si interface created by POW-RAY software

A constant number of atoms, constant volume and constant temperature simulation (NTV) was performed with  $0.001\text{ ps}$  time step. Because straining via moving atomic planes adds considerable energy to the active atoms, a Nose-Hover thermostat

was used. The thermostat applies a damping or acceleration factor to the active atoms based on the difference between the current temperature and the desired temperature. Two surfaces are equilibrated at T=300K for 10ps. The two slabs (Al and Si) were brought into contact and equilibrated for another 10ps. A constant velocity was prescribed for top 4 planes of the top slab. The stress and strain tensors were determined by averaging over the initial  $\pm 3$  planes ( $\sim \pm 5 \text{ \AA}$ ) across the interface.

For each atom the dipole force tensor is given as [16]:

$$D_{km}^i = \frac{1}{\Omega_i} \sum_{j \neq i}^N f_k^i(r^{ij}) r_d^{ij}, \quad (6.7)$$

where i and j refer to the neighboring atoms,  $f_k$  is the kth component of the force between the atoms,  $r_d$  is the vector between the atoms, N is the number of the nearest neighbors, and  $\Omega_i$  is the atomic volume. Since the stress is a continuum quantity it should be defined as volume average over block of material ( $N^*$ ) as

$$\sigma_{mk} = \frac{1}{N^*} \sum_i^{N^*} D_{km}^i. \quad (6.8)$$

The local small strain tensor can be obtained from

$$\varepsilon_{ij} = \frac{1}{2} \left( \frac{\partial u_i}{\partial x_j} + \frac{\partial u_j}{\partial x_i} \right), \quad (6.9)$$

where  $u_i$  is the averaged displacements within volume  $N^*$

$$u_i = \frac{1}{N^*} \sum_i^{N^*} u_i(\vec{r}_i). \quad (6.10)$$

Table 6.1 shows the Al and Si parameters that are used in our simulations [16].

Table 6.1 Al and Si parameters. Values listed are the lattice constant  $a_0$  in Å, the sublimation energy  $E_0$  in eV, the exponential decay factor for the universal energy function  $\alpha$ , the scaling factor for the embedding energy  $A$ , the exponential decay factors for the atomic densities  $\beta_i$  and the weighting factors for the atomic densities  $t_i$

	$\alpha$	$\beta_0$	$\beta_1$	$\beta_2$	$\beta_3$	$a_0$	$\rho_0$
	$E_0$	$A$	$t_0$	$t_1$	$t_2$	$t_3$	
Al	4.61	2.21	2.20	6.0	2.20	4.05	0.6
	3.58	1.07	1.0	-1.78	-2.21	8.01	
Si	4.87	4.8	4.8	4.8	4.8	5.43	1.0
	4.63	1.0	1.0	3.30	5.105	-0.80	

CHAPTER VII  
RESULTS AND DISCUSSIONS

7.1 EAM Results

As explained in the Chapter 6, different input values are used in the simulations. In this section, we will present the simulation results for EAM with Lenard-Jones pair potential. As a first example, following input values are used.

Table 7.1 The input values for the first simulation (stresses are applied to the top wall)

deltaT (time step)	0.005
rTopWallVel (velocity)	0.02
rNormalStress (normal stress)	0.002
rShearStress (shear stress)	0.002
rNebrShell (cutoff radius)	0.4

For example, initial velocity of the top wall in dimensionless form is 0.02; using Eq. (6.7) , the velocity value is equal to

$$V = \tilde{V} \sqrt{\frac{\varepsilon}{m}} = 3.147 m/s$$

Using equations (6.4) through (6.9), the dimensional value of each input can be calculated.

The following table summaries these values

Table 7.2 Dimensional values of inputs

deltaT	$1.08 \times 10^{-14} s$
rTopWallVel	$3.147 m/s$
rNormalStress	$84.3 kPa$
rShearStress	$84.3 kPa$

Following figures show the evolution of the Al-Si near-surface microstructures for the first simulation.

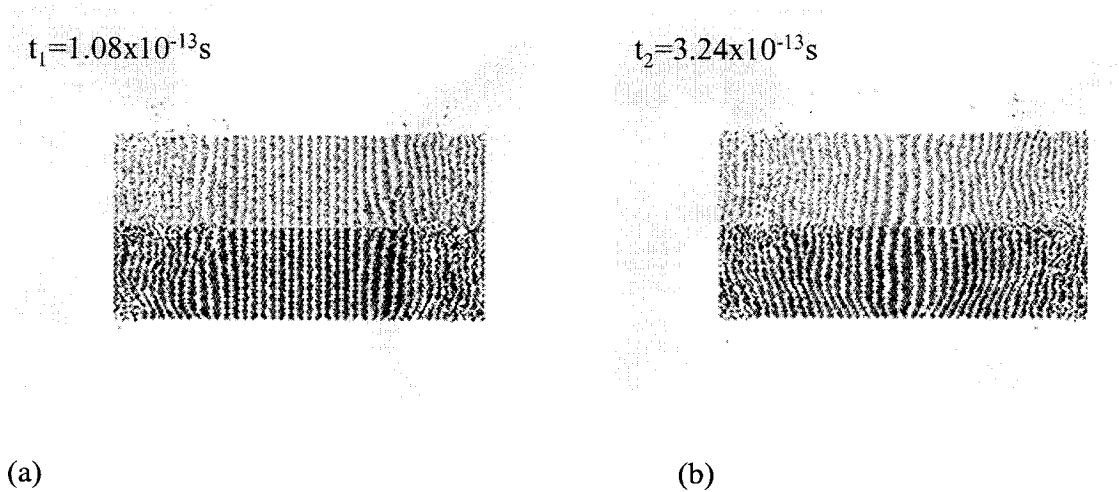
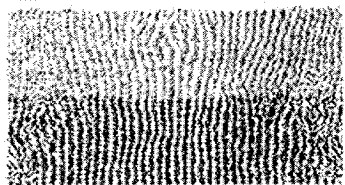


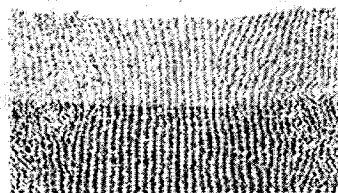
**Fig. 7.1** The evolution of the AlSi interface under shear stress applied to the top wall (40 Si and 40 Al layers)

$t_3=5.40 \times 10^{-13} \text{s}$



(c)

$t_4=7.56 \times 10^{-13} \text{s}$



(d)

**Fig. 7.1 (Continued)**

The results for this system as follows:

Table 7.3 Information for the system (current time, kinetic energy, number of atoms) at times determined by stepAvg

TimeNow (fs)	kinEnergy (J)	AveTemperature (K)	NumOfMolecules
10.0000	0.1573	18.876	14614
20.0000	0.1361	16.332	14614
30.0000	0.1276	15.312	14614
40.0000	0.1106	13.272	14614
50.0000	0.1082	12.984	14614
60.0000	0.1143	13.716	14614
70.0000	0.1191	14.292	14614

The average temperature of the system for each step is computed by using

$$E_k = \frac{i}{2} k_B T \quad (7.1)$$

where  $i=2$  for 2D system and  $k_B= 1.38 \times 10^{-23}$  J/K.

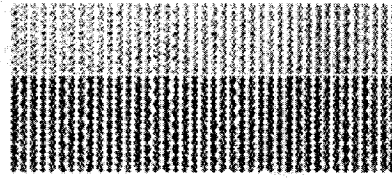
For the second example, the input values are:

Table 7.4 The input values for the second simulation (stresses are applied to the top wall)

deltaT (time step)	0.005
rTopWallVel (velocity)	0.02
rNormalStress (normal stress)	0.2
rShearStress (shear stress)	0.002
rNebrShell (cutoff radius)	0.4

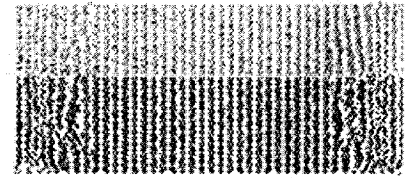
Following figures show the evolution of the Al-Si near-surface microstructures for the second simulation.

$$t_1 = 1.08 \times 10^{-13} \text{ s}$$



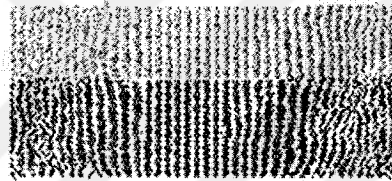
(a)

$$t_2 = 3.24 \times 10^{-13} \text{ s}$$



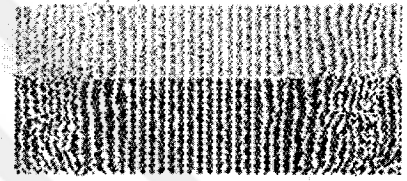
(b)

$$t_3 = 5.40 \times 10^{-13} \text{ s}$$



(c)

$$t_4 = 7.56 \times 10^{-13} \text{ s}$$



(d)

**Fig. 7.2** The evolution of the AlSi interface under normal and shear stress applied to the top wall (30 Si and 40 Al layers)

The results for this system are shown in Table 7.5.

All three examples clearly show the evolution of the AlSi interface under normal and shear stress applied to the top wall for different input values. A reduction in average temperature and kinetic energy was observed. Average temperatures are very low (approximately 20 K) and decrease with time. These preliminary results indicated that

EAM was not a suitable potential for Al-Si alloys. This finding was also noted by Baskes et al [14, 61]. Therefore MEAM was used to describe the interface.

Table 7.5 Information for the system (current time, kinetic energy, number of atoms) at times determined by stepAvg.

TimeNow (fs)	kinEnergy (J)	AveTemperature (K)	NumOfMolecules
10.0000	0.1712	20.544	12764
20.0000	0.1579	18.948	12764
30.0000	0.1538	18.456	12764
40.0000	0.1525	18.300	12764
50.0000	0.1496	17.952	12764
60.0000	0.1440	17.280	12764
70.0000	0.1376	16.512	12764

## 7.2 MEAM Results

In this subsection, we present the result from MD simulations using MEAM with Verlett integration algorithm.

The aim of this study was to understand the debonding and fracture mechanisms of the Al-Si alloys. Scientist who worked on aluminum alloys realized that one of the most important aspects of them is the understanding of interface and interface structures, because deformation characteristics of interface have a strong influence on the mechanical properties of these alloys. Furthermore, experimental and simulations on this subject clearly showed that the Al-Si interface is the weak link for the failure [2, 16, 23-28]. The current study using MD simulations with MEAM also proved that the interface is the primarily place for deformation.

The far-field opening displacements and true strains were calculated from the velocities at the far ends of MEAM model. The displacement difference during the simulation between the atomic planes initially at  $\pm 3$  planes (approximately  $\pm 5 \text{ \AA}$ ) from the interface is used to calculate the local opening displacements.

It has been observed [56] that stick-slip behaviour is followed by an intermittent stick slip and then by sliding as the shear rate increases. Stick-slip behaviour has also been seen in direct molecular dynamical simulations. Li et al. [57] investigated the stick-slip on an atomic scale by using the embedded atom method potential for Ni–Al. Their analysis of the dynamic features of the atoms in the sliding block clearly showed that the elastic deformation of the surface layers is the main cause for the stick-slip phenomenon, which is consistent with the macroscopic stick-slip. Landman et al. [58] simulated stick-slip behaviour by sliding a Si tip on a Si (111) substrate and a  $\text{CaF}_2$  tip on a  $\text{CaF}_2$  substrate. Bowden and Tabor [59] explained the stick slip behaviour by a simple model shown in Fig. 7.3.

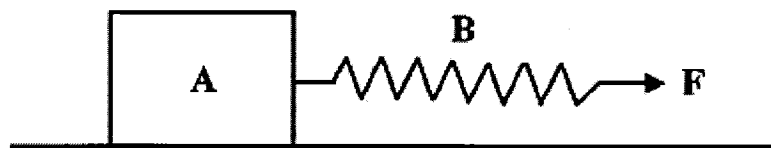


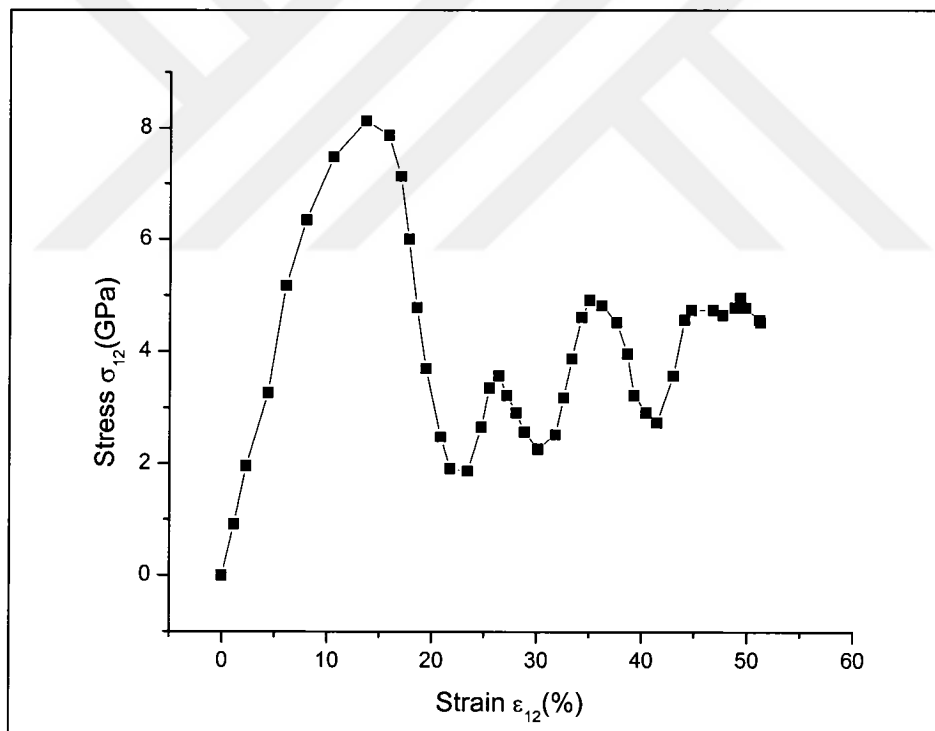
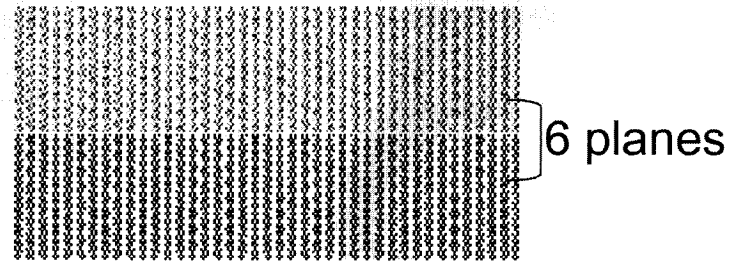
**Fig. 7.3** Spring model for macroscopic stick slip.

First, the body A and the spring B stand still. As the spring is stretched to a certain distance, an increasing force will be imposed on A. However, A will not move until the tension in the spring reaches the static friction value  $F_s$ . As soon as the static friction is exceeded, A will start to move. If the kinetic friction is much smaller than the

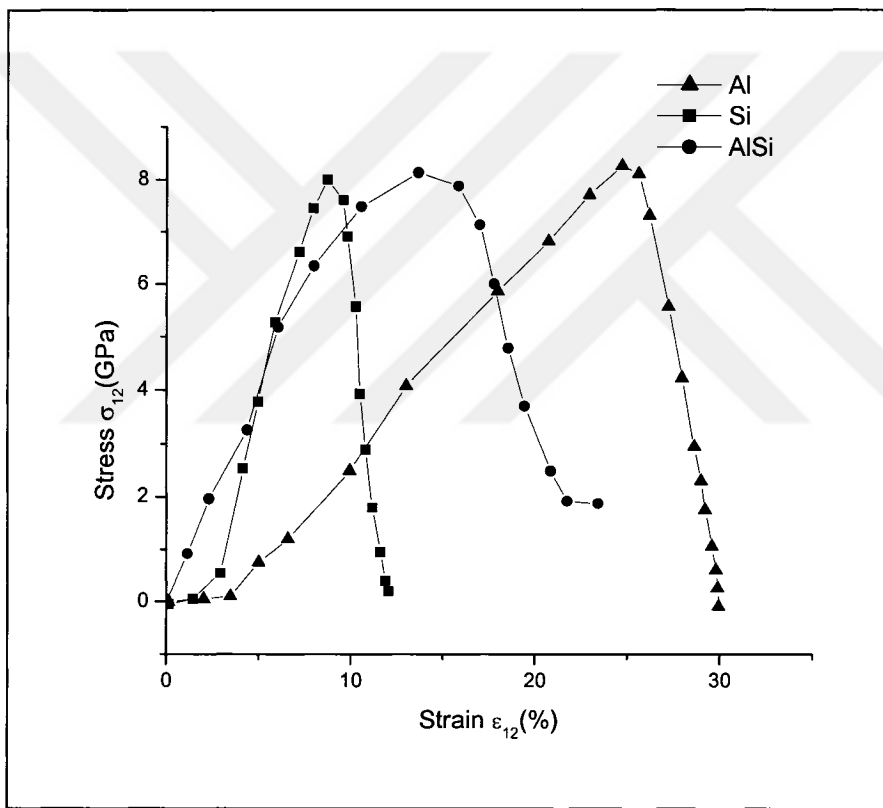
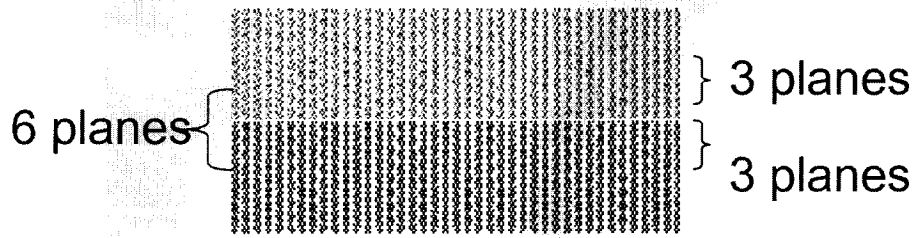
static, the spring will exert more force than is needed to maintain the body in motion. Then A will slide much more rapidly than the speed of B. This will restore the spring back to its unstretched state so that no force is being exerted on A. It therefore comes to rest. Then we shall have to pull the spring again and start the next cycle.

Fig. 7.4 represents the average shear stress against the average shear strain. Averaging is done across the initial  $\pm 3$  planes in both Al and Si slabs as shown in the same figure and a characteristic stick-slip behaviour is observed. After equilibration of the interface, shear applied to the top Si plane farthest from the interface. Therefore first it is needed higher shear value to slip the Si slab. However, after first slip we introduce some deformations to the interface, this caused the slip at lower shear value. Same behaviour is observed by Gall et al. [16] shown in Fig. 5.1 as a elastic spring-back.

The stress-strain relationships within each of the Al, Si and the interface Al-Si are presented in Fig 7.5. Here, the stress is evaluated by the Eq. (6.11) and strain calculated by Eq. (6.12). Three planes next to the interface are used for Al and Si to calculate the stress and strain, while six planes are used to represent the interface. The peak stress of silicon crystal is about 8GPa at the strain of 8%, and at the same stress, the interface has the strain of 14% while aluminum has the strain of 24%. As expected, Si is the harder material and the induced deformation at the interface is between the one induced in Si and Al. At 3GPa stress, the interface has larger stress values for same strains. This interesting behaviour may caused by the potential. The force depends on the deepness of the potential well and the slope of the well at small movements from the equilibrium position.



**Fig. 7.4** The averaged shear stress against the averaged shear strain



**Fig. 7.5** The stress-strain relationships within each of the Al, Si and the interface AlSi

The far field displacements are given in Fig. 7.6. They are calculated by averaging displacements at the top 3 atomic planes in the top slab. The peak stress is about 8GPa at

the far field displacement of 12Å. Gall et al. [16] observed the same behaviour shown in Fig. 5.4b.

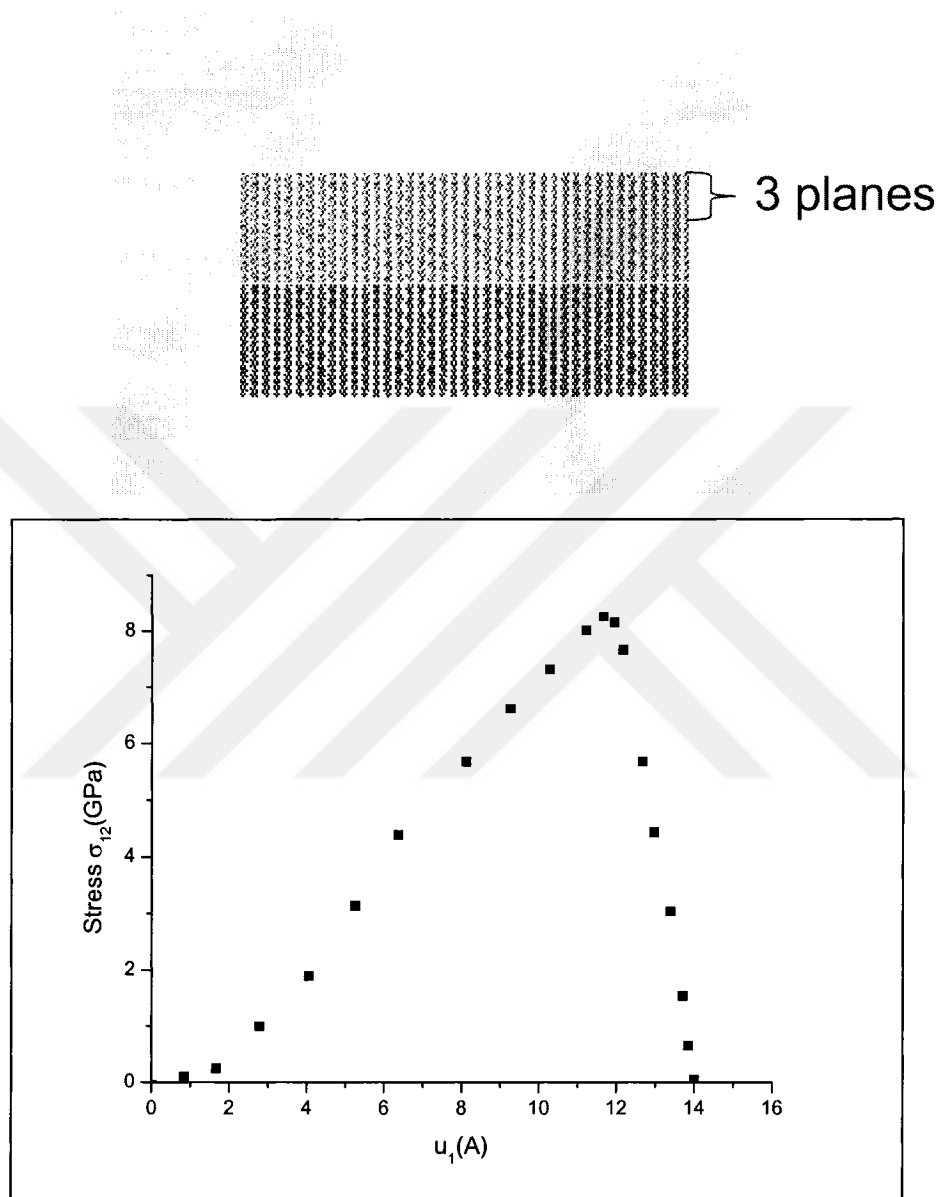


**Fig. 7.6** The far field displacements (average displacement at the top 3 atomic planes in the top slab)

The local displacements (averaged displacement at  $\pm 3$  planes atomic planes at the interface) are given in Fig. 7.7. Here, the 8 GPa peak stress observed at the local

displacement of  $3\text{\AA}$ , it was  $12\text{\AA}$  on the far field displacements. The result in Fig. 7.7 shows that local displacement measurements provide much different result than far-field displacement measurements. These two figures indicate that the interface is the weak link for failure.

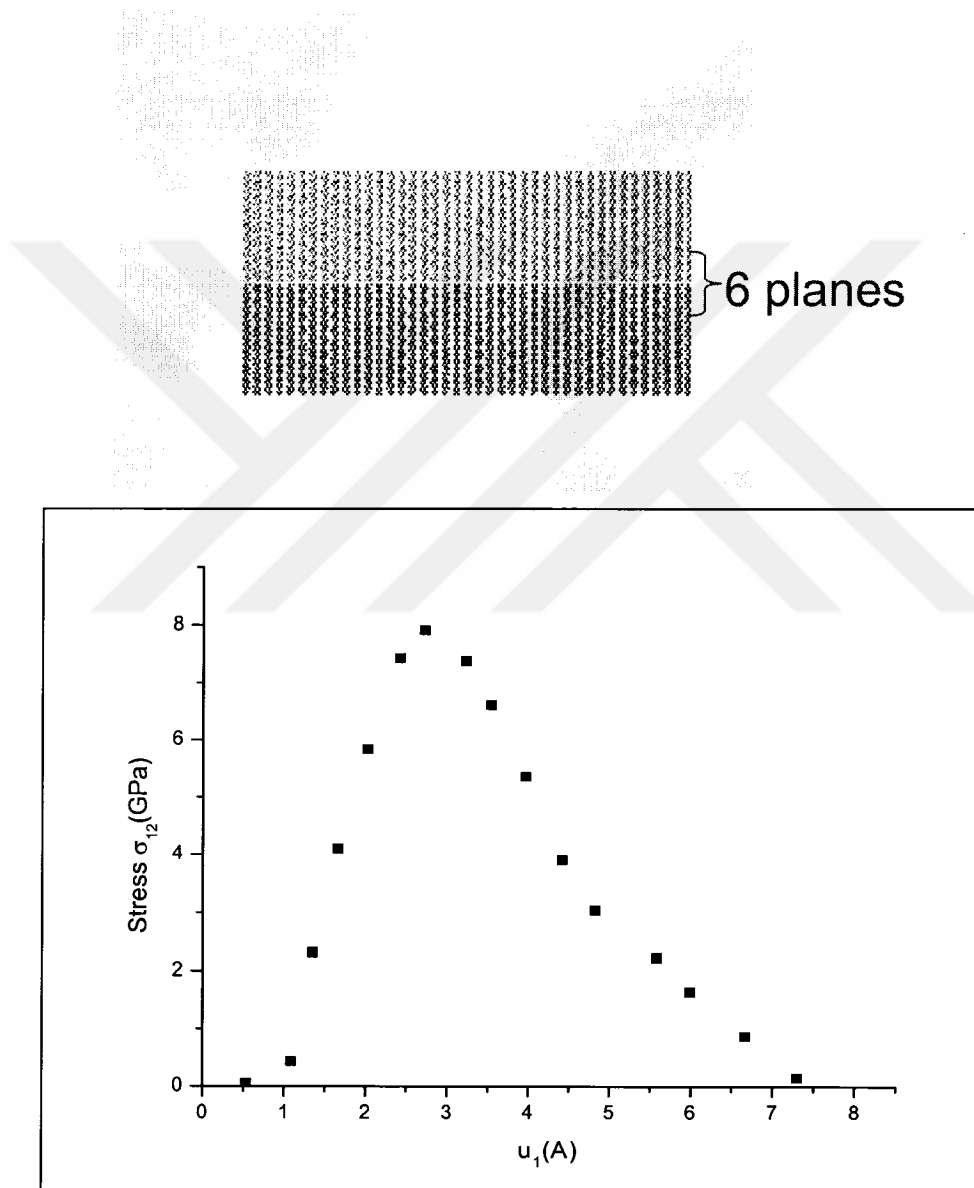


**Fig. 3** The local displacements (average displacement at  $\pm 3$  planes atomic planes at the interface)

Finally, comparison of the simulation results with the macro level experiment [32]

shown in Fig 7.8. Eq. (5.2) is used with different coefficient as following:

$$\frac{\sigma_{12}}{\sigma_{\max}} = 9.42 \frac{u_1}{u_{\max}} \exp \left[ -4.62 \frac{u_1}{u_{\max}} \right] \quad (7.2)$$

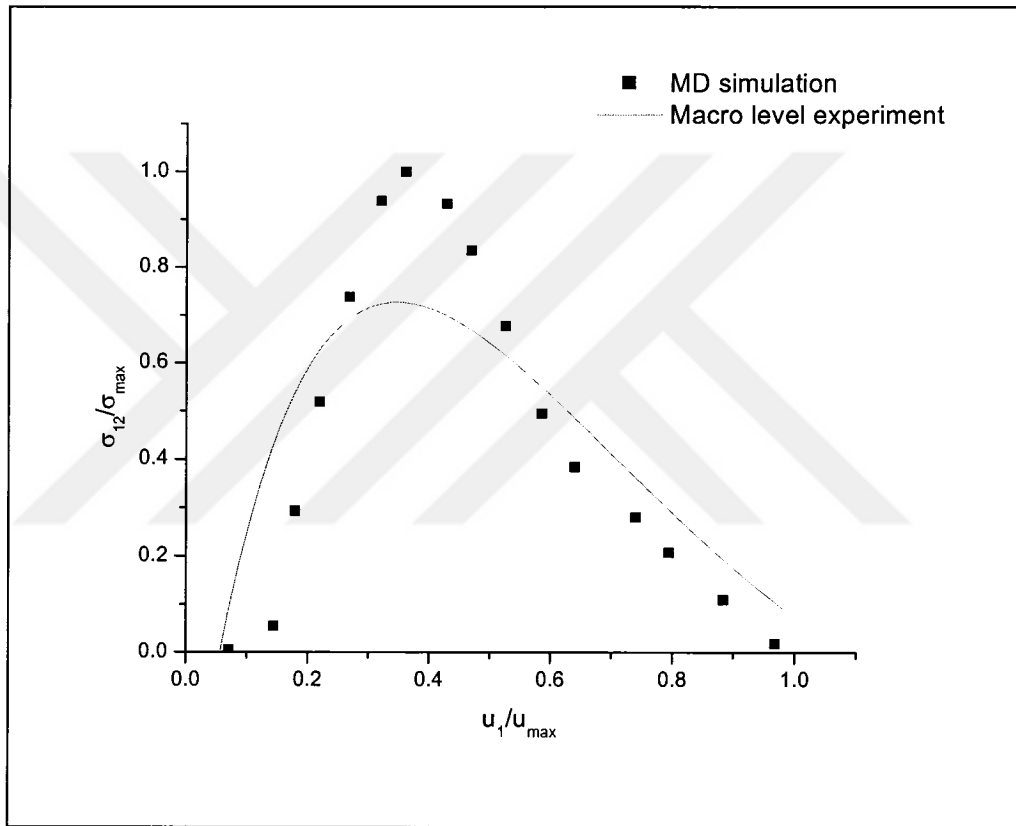


**Fig. 7.8** Comparison of the MD simulation results with the finite element method results

As explained in Chapter 5, the separation laws are contrived such that when  $u_1$  approaches  $u_{\max}$ ,  $\sigma_{12}$  approaches zero and the interface is considered to be separated.

In a continuum-based approach it is important to consider the distance over which atoms from the two materials near the interface interact with one another during the

debonding, this is called the physical cohesive zone size. Thus, the traction–displacement MEAM results with Eq. (7.1) are sufficient to represent the debonding character of the interface. It is not appropriate to measure the displacement within the bounds of the physical cohesive zone; we think that this is the reason for the inaccuracy of our result. Using planes within the cohesive zone to measure the opening displacement is inaccurate since the atoms do not remain in a planar structure, and atoms contributing to the debonding mechanism are discarded in the analysis [16]. Furthermore, another possible source of error may result from the implementation of the small strain formulation in the analysis software.

## CHAPTER VIII

### CONCLUSIONS AND FUTURE WORK

#### 8.1 Conclusions

Computer simulations help to provide progress towards comprehensive understanding of the influence of interfaces on material properties. As outlined in previous chapters, atomic-scale and multiscale computer modelling has provided valuable insights into the structure of interfaces.

The following summarizes the main points of this thesis:

1. It is proved that EAM was not a suitable method describing the Al-Si interface. Preliminary simulations showed that average temperatures were very low approximately 20 K and decreased with time.
2. The Modified Embedded Atom Method was successfully applied to aluminum-silicon alloys.
3. The average shear stress and the average shear strain are calculated across the initial  $\pm 3$  planes in both Al and Si slabs. A characteristic stick-slip behaviour was observed. The peak stress of the interface is about 8GPa (debonding at the interface) at the strain of 14%, after first slip, due to the introduced deformations the new peak stress is around 4GPa at the strain of 25%.
4. The stress-strain relationships for the interface are established. In the absence of defects like vacancies, dislocations, and impurities, the interfacial failure occurs over a finite strain increment. The interface failed at 8GPa stress with the strain of 14%.

5. The results demonstrate that MEAM predictions are consistent with the finite element method (FEM) results. At normalized small stress values the correlation between the MD simulation and the FEM is acceptable (around %20), but at higher stress levels it is not.

## 8.2 Future Work

Following suggestions can be made for future work:

1. Different crystals orientation

For given temperature, normal and shear load compute traction-displacement and stress-strain for:

- a) aligned Al and Si blocks  $[100]_{\text{Al}}[100]_{\text{Si}}$ ,  $[010]_{\text{Al}}[010]_{\text{Si}}$ ,  $[010]_{\text{Al}}[010]_{\text{Si}}$ , rotation of one of the block 0, 30, 45, 60, 90 about  $[001]$
- b)  $[111]_{\text{Al}}[111]_{\text{Si}}$  and rotation of the Si 0, 30, 45, 60, 90 about  $[001]$
- c)  $[111]_{\text{Al}}[100]_{\text{Si}}$  and rotation of the Si 0, 30, 45, 60, 90 about  $[001]$

2. Different temperature

For given normal and shear load compute traction-displacement and stress-strain for case 1. Suggested thermostat temperatures 0K, 150K, 300K, 450K, 600K

3. Different normal loads

For given shear load compute traction-displacement and stress-strain for case 2 at different normal loads.

4. Different shear loads

The shear loads can be specified either as tractions or velocities applied to the far field planes. For given shear load compute traction-displacement and stress-strain for

case 3. For the dynamic case the suggested velocities are 0.5Å/ps, 1Å/ps, 1.5Å/ps, 2Å/ps, 2.5Å/ps.

5. Increase the number of atoms in the simulation.



## APPENDICES

### APPENDIX A

#### The derivation of the forces

The force on each atom can be given by

$$\bar{F}_i = -\sum_i \left[ \sum_{m=1}^3 i_m \left( \frac{\partial F_i}{\partial \bar{\rho}_i} \frac{\partial \bar{\rho}_i}{\partial r_{ij}} \frac{\partial r_{ij}}{\partial x_m} + \frac{1}{2} \sum_{j \neq i} \left( S_{ij} \frac{\partial \phi(r_{ij})}{\partial r_{ij}} \frac{\partial r_{ij}}{\partial x_m} \right) \right) \right] \quad (1)$$

Now calculate the part  $\frac{\partial F_i}{\partial \bar{\rho}_i} \frac{\partial \bar{\rho}_i}{\partial r_{ij}} \frac{\partial r_{ij}}{\partial x_m}$ ,

First,

$$\frac{\partial F_i}{\partial \bar{\rho}_i} = AE_c \frac{1}{\rho_0} \left( \ln \frac{\bar{\rho}_i}{\rho_0} + 1 \right) \quad (2)$$

then find  $\frac{\partial \bar{\rho}_i}{\partial r_{ij}}$  using Eq. (4.21)

$$\frac{\partial \rho_i}{\partial r_{ij}} = \frac{2 \frac{\partial \rho_i^{(0)}}{\partial r_{ij}} \left( 1 + \exp \left( -\sum_{s=1}^3 t_i^{(s)} \left( \frac{\rho_i^{(s)}}{\rho_i^{(0)}} \right)^2 \right) \right) - 2 \rho_i^{(0)} \frac{\partial \left( \exp \left( -\sum_{s=1}^3 t_i^{(s)} \left( \frac{\rho_i^{(s)}}{\rho_i^{(0)}} \right)^2 \right) \right)}{\partial r_{ij}}}{\left( 1 + \exp \left( -\sum_{s=1}^3 t_i^{(s)} \left( \frac{\rho_i^{(s)}}{\rho_i^{(0)}} \right)^2 \right) \right)^2} \quad (3)$$

Define a new term , $T_1$ , as ( these terms are defined to make the calculations easier)

$$T_1 = \exp \left( -\sum_{s=1}^3 t_i^{(s)} \left( \frac{\rho_i^{(s)}}{\rho_i^{(0)}} \right)^2 \right) \quad (4)$$

$$\rho_i^{(0)} = \sum_j \rho_j^{a(0)}(r_{ij}) = \sum S_{ij} f_c(r_{ij}) f_j^0 \exp\left(-\beta_j^{(0)} \left(\frac{r_{ij}}{r_e} - 1\right)\right) \quad (5)$$

$$\frac{\partial \rho_i^{(0)}}{\partial r_{ij}} = \sum_j S_{ij} f_c(r_{ij}) f_j^0 \left(-\frac{\beta_j^{(0)}}{r_e}\right) \exp\left(-\beta_j^{(0)} \left(\frac{r_{ij}}{r_e} - 1\right)\right) \quad (6)$$

$$\frac{\partial T_1}{\partial r_{ij}} = \frac{\partial \exp\left(-t_i^{(1)} \left(\rho_i^{(1)} / \rho_i^{(0)}\right)^2 - t_i^{(2)} \left(\rho_i^{(21)} / \rho_i^{(0)}\right)^2 - t_i^{(3)} \left(\rho_i^{(3)} / \rho_i^{(0)}\right)^2\right)}{\partial r_{ij}} \quad (7)$$

$$\frac{\partial \left(\rho_i^{(1)} / \rho_i^{(0)}\right)^2}{\partial r_{ij}} = \frac{\frac{\partial \left(\rho_i^{(1)}\right)^2}{\partial r_{ij}} \left(\rho_i^{(0)}\right)^2 - \left(\rho_i^{(1)}\right)^2 \frac{\partial \left(\rho_i^{(0)}\right)^2}{\partial r_{ij}}}{\left(\rho_i^{(0)}\right)^4} \quad (8)$$

$$\left(\rho_i^{(1)}\right)^2 = \sum_{j,k \neq i} \rho_i^{a(1)}(r_{ij}) \rho_i^{a(1)}(r_{ik}) L^{(1)}(\cos \theta_{jik}) = \sum_{j,k \neq i} \rho_i^{a(1)}(r_{ij}) \rho_i^{a(1)}(r_{ik}) \cos \theta_{jik} \quad (9)$$

$\cos \theta_{jik}$  can be given using a triangle

$$\cos \theta_{jik} = \frac{r_{ij}^2 + r_{ik}^2 - r_{jk}^2}{2r_{ij}r_{ik}} = n \quad (10)$$

Derivative of this term

$$\frac{\partial \cos \theta_{jik}}{\partial r_{ij}} = \frac{r_{ij}^2 - r_{ik}^2 + r_{jk}^2}{2r_{ij}^2 r_{ik}} = n_1 \quad (11)$$

Using Eq. (9)

$$\left(\rho_i^{(1)}\right)^2 = \sum_{j,k \neq i} S_{ij} S_{ik} f_c(r_{ij}) f_c(r_{ik}) \left(f_j^0\right)^2 \exp\left(-\beta_j^{(1)} \left(\frac{r_{ij}}{r_e} - 1\right) - \left(-\beta_k^{(1)} \left(\frac{r_{ik}}{r_e} - 1\right)\right)\right) \left(\frac{r_{ij}^2 + r_{ik}^2 - r_{jk}^2}{2r_{ij}r_{ik}}\right) \quad (12)$$

Define  $m$  as

$$m = \exp\left(-\beta_j^{(1)}\left(\frac{r_{ij}}{r_e}-1\right)-\left(-\beta_k^{(1)}\left(\frac{r_{ik}}{r_e}-1\right)\right)\right) \quad (13)$$

$$\begin{aligned} \frac{\partial(\rho_i^{(1)})^2}{\partial r_{ij}} = \sum_{j,k \neq i} S_{ij} S_{ik} f_c(r_{ij}) f_c(r_{ik}) (f_j^0)^2 & \left\{ -\frac{\beta_j^{(1)}}{r_e} \exp\left(-\beta_j^{(1)}\left(\frac{r_{ij}}{r_e}-1\right)-\beta_k^{(1)}\left(\frac{r_{ik}}{r_e}-1\right)\right) \left(\frac{r_{ij}^2+r_{ik}^2-r_{jk}^2}{2r_{ij}r_{ik}}\right) \right. \\ & \left. + \exp\left(-\beta_j^{(1)}\left(\frac{r_{ij}}{r_e}-1\right)-\beta_k^{(1)}\left(\frac{r_{ik}}{r_e}-1\right)\right) \left(\frac{r_{ij}^2-r_{ik}^2+r_{jk}^2}{2r_{ij}r_{ik}}\right) \right\} \end{aligned} \quad (14)$$

$$\frac{\partial(\rho_i^{(1)})^2}{\partial r_{ij}} = \sum_{j,k \neq i} S_{ij} S_{ik} f_c(r_{ij}) f_c(r_{ik}) (f_j^0)^2 \left[ -\frac{\beta_j^{(1)}}{r_e} mn + mn_1 \right] \quad (15)$$

$$\frac{\partial(\rho_i^{(2)}/\rho_i^{(0)})^2}{\partial r_{ij}} = \frac{\frac{\partial(\rho_i^{(2)})^2}{\partial r_{ij}} (\rho_i^{(0)})^2 - (\rho_i^{(2)})^2 \frac{\partial(\rho_i^{(0)})^2}{\partial r_{ij}}}{(\rho_i^{(0)})^4} \quad (16)$$

$$(\rho_i^{(2)})^2 = \sum_{j,k \neq i} \rho_i^{a(2)}(r_{ij}) \rho_i^{a(2)}(r_{ik}) L^{(2)}(\cos \theta_{jik}) = \sum_{j,k \neq i} \rho_i^{a(2)}(r_{ij}) \rho_i^{a(2)}(r_{ik}) \left( \cos^2 \theta_{jik} - \frac{1}{3} \right) \frac{1}{2} \quad (17)$$

$$(\rho_i^{(2)})^2 = \sum_{j,k \neq i} S_{ij} S_{ik} f_c(r_{ij}) f_c(r_{ik}) (f_j^0)^2 \exp\left(-\beta_j^{(2)}\left(\frac{r_{ij}}{r_e}-1\right)-\beta_k^{(2)}\left(\frac{r_{ik}}{r_e}-1\right)\right) \left( n^2 - \frac{1}{3} \right) \frac{1}{2} \quad (18)$$

Define  $m_1$  as

$$m_1 = \exp\left(-\beta_j^{(2)}\left(\frac{r_{ij}}{r_e}-1\right)-\beta_k^{(2)}\left(\frac{r_{ik}}{r_e}-1\right)\right) \quad (19)$$

$$\frac{\partial(\rho_i^{(2)})^2}{\partial r_{ij}} = \sum_{j,k \neq i} S_{ij} S_{ik} f_c(r_{ij}) f_c(r_{ik}) (f_j^0)^2 \left[ -\frac{\beta_j^{(2)}}{r_e} m_1 \left( n^2 - \frac{1}{3} \right) \frac{1}{2} + m_1 n n_1 \right] \quad (20)$$

$$\frac{\partial(\rho_i^{(3)}/\rho_i^{(0)})^2}{\partial r_{ij}} = \frac{\frac{\partial(\rho_i^{(3)})^2}{\partial r_{ij}}(\rho_i^{(0)})^2 - (\rho_i^{(3)})^2 \frac{\partial(\rho_i^{(0)})^2}{\partial r_{ij}}}{(\rho_i^{(0)})^4} \quad (21)$$

$$(\rho_i^{(3)})^2 = \sum_{j,k \neq i} \rho_i^{a(3)}(r_{ij}) \rho_i^{a(3)}(r_{ik}) L^{(3)}(\cos \theta_{jik}) = \sum_{j,k \neq i} \rho_i^{a(3)}(r_{ij}) \rho_i^{a(3)}(r_{ik}) \left( \cos^3 \theta_{jik} - \frac{3}{5} \cos \theta_{jik} \right) \frac{1}{2} \quad (22)$$

$$(\rho_i^{(3)})^2 = \sum_{j,k \neq i} S_{ij} S_{ik} f_c(r_{ij}) f_c(r_{ik}) (f_j^0)^2 \exp\left(-\beta_j^{(3)} \left(\frac{r_{ij}}{r_e} - 1\right) - \beta_k^{(3)} \left(\frac{r_{ik}}{r_e} - 1\right)\right) \left(n^3 - \frac{3}{5}n\right) \frac{1}{2} \quad (23)$$

Define  $m_2$  as

$$m_2 = \exp\left(-\beta_j^{(3)} \left(\frac{r_{ij}}{r_e} - 1\right) - \beta_k^{(3)} \left(\frac{r_{ik}}{r_e} - 1\right)\right) \quad (24)$$

$$\frac{\partial(\rho_i^{(3)})^2}{\partial r_{ij}} = \sum_{j,k \neq i} S_{ij} S_{ik} f_c(r_{ij}) f_c(r_{ik}) (f_j^0)^2 \left[ -\frac{\beta_j^{(3)}}{r_e} m_2 \left(n^3 - \frac{3}{5}n\right) \frac{1}{2} + m_2 \left(\frac{3}{2}n^2 n_1 - \frac{3}{10}n_1\right) \right] \quad (25)$$

$$\frac{\partial r_{ij}}{\partial x_m} = \frac{x_m}{r_{ij}} \quad (26)$$

Using all these derivatives we get

$$\frac{\partial F_i}{\partial \rho_i} \frac{\partial \rho_i}{\partial r_{ij}} \frac{\partial r_{ij}}{\partial x_m} = Eq.(2) \left[ \frac{2Eq.(24)(1+T_1) - 2\rho_i^0 (t_i^{(1)} Eq.(6) + t_i^{(2)} Eq.(8) + t_i^{(3)} Eq.(21))}{(1+T_1)^2} \right] \frac{x_m}{r_{ij}} \quad (27)$$

The second part can be written in the following form by using Eq. (4.17):

$$\frac{1}{2} \sum_{j \neq i} \left( S_{ij} \frac{\partial \phi(r_{ij})}{\partial r_{ij}} \frac{\partial r_{ij}}{\partial x_m} \right) = \frac{1}{2} \sum_{j \neq i} \frac{2}{Z_i} \frac{\partial}{\partial r_{ij}} \left[ E_i^u(r_{ij}) - F_i(\rho_i^{(0)}(r_{ij})) \right] \frac{\partial r_{ij}}{\partial x_m} \quad (28)$$

The derivatives of the each term are calculated as

$$\frac{\partial E_i^u(r_{ij})}{\partial r_{ij}} = E_c \frac{\alpha^2}{r_e} \left( \frac{r_{ij}}{r_e} - 1 \right) \exp \left( -\alpha \left( \frac{r_{ij}}{r_e} - 1 \right) \right) \quad (29)$$

$$\frac{\partial F_i}{\partial \rho_i^{(0)}} = AE_c \frac{1}{\rho_0} \left( \ln \frac{\rho_i^{(0)}}{\rho_0} + 1 \right) \quad (30)$$

And  $\frac{\partial \rho_i^{(0)}}{\partial r_{ij}}$  is given by Eq.(8), so whole equation becomes

$$\begin{aligned} \frac{1}{2} \sum_{j \neq i} \left( S_{ij} \frac{\partial \phi(r_{ij})}{\partial r_{ij}} \frac{\partial r_{ij}}{\partial x_m} \right) &= \frac{1}{Z_i} \sum_{j \neq i} S_{ij} \left\{ E_c \left( -\frac{\alpha}{r_e} \right) \exp \left( -\alpha \left( \frac{r_{ij}}{r_e} - 1 \right) \right) \left( 1 + \alpha \left( \frac{r_{ij}}{r_e} - 1 \right) \right) \right. \\ &\quad \left. - AE_c \frac{1}{\rho_0} \left( \ln \frac{\rho_i^{(0)}}{\rho_0} + 1 \right) \sum_j S_{ij} f_c(r_{ij}) f_j^0 \left( -\frac{\beta_j^{(0)}}{r_e} \right) \exp \left( -\beta_j^{(0)} \left( \frac{r_{ij}}{r_e} - 1 \right) \right) \right\} \frac{x_m}{r_{ij}} \end{aligned} \quad (31)$$

Finally,

$$\bar{F}_i = \sum_i \sum_{m=1}^3 \hat{i}_m [Eq.(27) + Eq.(31)] \quad (32)$$

Calculation of Al-Si pair potential

$$\phi_{Al-Si}(r_{ij}) = \frac{2}{Z_i} \left[ E_i^u(r_{ij}) - F_{Al} \left( \frac{\bar{\rho}_{Si}}{12\rho_{Al}^{(0)}} \right) - F_{Si} \left( \frac{\bar{\rho}_{Al}}{4\rho_{Si}^{(0)}} \right) \right] \quad (33)$$

$$\bar{\rho}_{Si} = Z\rho_{Si}^{(0)}(r_{ij}) \quad (34)$$

$$\bar{\rho}_{Al} = Z\rho_{Al}^{(0)}(r_{ij}) \quad (35)$$

where  $Z=6$  is the nearest neighbor coordination number.

Next step is taking derivative of this potential

$$\frac{1}{2} \sum_{j \neq i} \left( S_{ij} \frac{\partial \phi(r_{ij})}{\partial r_{ij}} \frac{\partial r_{ij}}{\partial x_m} \right) = \frac{1}{Z_i} \sum_{j \neq i} S_{ij} \frac{\partial}{\partial r_{ij}} \left[ E_i^u(r_{ij}) - F_{Al} \left( \frac{\bar{\rho}_{Si}}{12\rho_{Al}^{(0)}} \right) - F_{Si} \left( \frac{\bar{\rho}_{Al}}{4\rho_{Si}^{(0)}} \right) \right] \frac{\partial r_{ij}}{\partial x_m} \quad (36)$$

$\frac{\partial E_i^u(r_{ij})}{\partial r_{ij}}$  is give by Eq. (29)

$$F_{Al} \left( \frac{\bar{\rho}_{Si}}{12\rho_{Al}^0} \right) = F_{Al} \left( \frac{Z\rho_{Si}^{(0)}}{12\rho_{Al}^0} \right) = AE_c \left( \frac{Z\rho_{Si}^{(0)}}{12\rho_{Al}^0} \right) \ln \left( \frac{Z\rho_{Si}^{(0)}}{12\rho_{Al}^0} \right) \quad (37)$$

$$F_{Si} \left( \frac{\bar{\rho}_{Al}}{4\rho_{Si}^0} \right) = F_{Si} \left( \frac{Z\rho_{Al}^{(0)}}{4\rho_{Si}^0} \right) = AE_c \left( \frac{Z\rho_{Al}^{(0)}}{4\rho_{Si}^0} \right) \ln \left( \frac{Z\rho_{Al}^{(0)}}{4\rho_{Si}^0} \right) \quad (38)$$

$$\frac{\partial F_{Si}}{\partial \rho_{Al}^{(0)}} = AE_c \left( \frac{Z}{4\rho_{Si}^0} \right) \left[ \ln \left( \frac{Z\rho_{Al}^{(0)}}{4\rho_{Si}^0} \right) + 1 \right] \quad (39)$$

$$\frac{\partial F_{Al}}{\partial \rho_{Si}^{(0)}} = AE_c \left( \frac{Z}{12\rho_{Al}^0} \right) \left[ \ln \left( \frac{Z\rho_{Si}^{(0)}}{12\rho_{Al}^0} \right) + 1 \right] \quad (40)$$

$$Q_1 = \frac{\partial \bar{\rho}_{Si}}{\partial r_{ij}} = \frac{\partial (Z\rho_{Si}^{(0)}(r_{ij}))}{\partial r_{ij}} = Z \sum_j S_{ij} f_c(r_{ij}) f_j \left( -\frac{\beta_{j(Si)}^{(0)}}{r_{e(Si)}} \right) \exp \left( -\beta_{j(Si)}^{(0)} \left( \frac{r_{ij}}{r_{e(Si)}} - 1 \right) \right) \quad (41)$$

$$Q_2 = \frac{\partial \bar{\rho}_{Al}}{\partial r_{ij}} = \frac{\partial (Z\rho_{Al}^{(0)}(r_{ij}))}{\partial r_{ij}} = Z \sum_j S_{ij} f_c(r_{ij}) f_j^0 \left( -\frac{\beta_{j(Al)}^{(0)}}{r_{e(Al)}} \right) \exp \left( -\beta_{j(Al)}^{(0)} \left( \frac{r_{ij}}{r_{e(Al)}} - 1 \right) \right) \quad (42)$$

Finally

$$\frac{1}{2} \sum_{j \neq i} \left( S_{ij} \frac{\partial \phi(r_{ij})}{\partial r_{ij}} \frac{\partial r_{ij}}{\partial x_m} \right) = \frac{1}{Z_i} \sum_{j \neq i} S_{ij} [Eq.(29) - Eq.(39)Q_2 - Eq.(40)Q_1] \frac{x_m}{r_{ij}} \quad (43)$$

$\beta$  decay lengths are given by

$$\beta_i^{(0)} = \left[ \frac{\alpha_i^2 - 2Z_i \gamma \Omega_i / E_i^0}{A_i} \right]^{1/2} \quad \text{for } \beta_i^{(2)} = 6 \quad (44)$$

$$\beta_i^{(0)} = \left[ \frac{\alpha_i^2 - 2Z_i \gamma \Omega_i / E_i^0}{A_i} \right]^{1/2} \text{ for } \beta_i^{(2)} = 2 \quad (45)$$

$$\beta_i^{(0)} = \left[ \frac{\alpha_i^2 - 2Z_i \gamma \Omega_i / 8E_i^0}{A_i} \right]^{1/2} \text{ for } \beta_i^{(2)} = 1 \quad (46)$$

Partial electron density weights are given by

$$t_i^{(2)} = \frac{(\gamma - 2\gamma') Z_i^2 \Omega_i}{2A_i E_i^0 (\beta_i^{(2)} - 2)^2} \text{ for } \beta_i^{(2)} = 6 \quad (47)$$

$$t_i^{(2)} = \frac{(2\gamma' - \gamma) Z_i^2 \Omega_i}{A_i E_i^0 (\beta_i^{(2)} - 6)^2} \text{ for } \beta_i^{(2)} = 2 \quad (48)$$

$$t_i^{(2)} = \frac{9\gamma' Z_i^2 \Omega_i}{256 A_i E_i^0} \text{ for bcc} \quad (49)$$

## REFERENCES

- [1] J.R. Davis, Ed., ASM Specialty Handbook: Aluminum and Aluminum Alloys, ASM International, p 485-706 (1993).
- [2] J. Zhang and A. T. Alpas, Mater. Sci. Eng. **A160**, p 25-35, (1993).
- [3] M. P. Allen and D. J. Tildesley, Computer Simulation of Liquids, Oxford University Press, New York, Ch 1, 1-30, Ch 3, 71-108(1990).
- [4] M. P. Allen, Computational Soft Matter: From Synthetic Polymers to Proteins, Lecture Notes, NIC Series, **23**, p 1-28, (2004)
- [5] B. J. Alder, and T. E. Wainwright, J. Chem. Phys. **27**, 1208, (1957)
- [6] A. Rahman, Physical Review, **A136**, 405, (1964)
- [7] F. H. Stillinger, and A. Rahman, J. Chem. Phys. **60**, 1545, (1974)
- [8] D. W. Rogers, Computational Chemistry using the PC, Wiley-Interscience, (2003).
- [9] P. Hohenberg and W. Kohn, Physical Review, **136**, 864, (1964)
- [10] R.G. Parr, and W. Yang, Density-Functional Theory of Atoms and Molecules, Oxford University Press, Ch. 3, 47-66 (1989)
- [11] M. S. Daw, and M. I. Baskes, Phys. Rev. Lett. **50**, 1285 (1983)
- [12] M. S. Daw, and M. I. Baskes, Phys. Rev. B **29**, 6443 (1984)
- [13] M. J. Scott and E. Zaremba, Phys. Rev. B **22**, 1564 (1980)
- [14] M. I. Baskes, J. S. Nelson, and A. F. Wright, Phys. Rev. B **40**, 6085 (1989)
- [15] M. I. Baskes, Phys. Rev. B **46**, 2727 (1992)
- [16] K. Gall, M.F. Horstemeyer, Mark Van Schilfgaarde and M. I. Baskes, J. Mech. Phys. Solids **48**, 2183 (2000)

- [17] J. M. Thijssen, Computational Physics, Cambridge University Press, Ch. 4, 45-94, Ch. 7, 175-242, Ch. 10, 271-299 (1999).
- [18] H. Luth, Surfaces and Interfaces of Solid Materials, 3rd Edition, 1-6, (1995)
- [19] A. P. Sutton and R. W. Balluffi, Interfaces in Crystalline Materials, Oxford Sci. Pub., Oxford, Ch. 1, 3-70, Ch. 5, 349-394 (1995).
- [20] D. N. Seidman, Experimental investigation of internal interfaces in solids, Material Interfaces, edited by D. Wolf and S. Yip, Ch. 2, 58-84, (1992)
- [21] R. C. Pond, Materials Phenomena, Ch. 5, 162-165, (2002).
- [22] Jien-Wei Yeh and Wen-Pin Liu, Metall. Trans. A **27A**, 3558-3568 (1996)
- [23] J. Gurland and J. Plateau, Trans. ASM **56**, 442-454, (1963)
- [24] A. Gangulee and J. Gurland, Trans. Am. Soc. Metals **239**, 269-272 (1967)
- [25] A. T. Alpas, H. Hu and J. Zhang, Wear **162-164**, 188-195 (1993)
- [26] C. Perrin and W. Rainforth, Wear **203**, 171-179 (1997)
- [27] A. T. Alpas and J. Embury, Wear **164**, 285-300 (1991)
- [28] K. Gall, N. Yang, M. Horstemeyer, D. McDowell and J. Fan, Metal. Mater. Trans., **30A**, 3079-88, (1999)
- [29] T. Diaz de la Rubia and V. V. Bulatov, MRS Bulletin, Materials Research Society, Warrendale, PA, USA, (2001).
- [30] M. I. Baskes, J. E. Angelo, C. L. Bison, Modell. Simul. Mater. Sci. Engng. **2**, 505-518, (1994).
- [31] K. Gall, M. F. Horstemeyer, D. L. McDowell, J. H. Fan, Mech. Mater., (2000)
- [32] A. Needleman, J. Appl. Mech. **54**, 525-531, (1987)
- [33] A. Needleman, J. Mech. Phys. Solids **38**, 289-324 (1990).

- [34] A. Needleman, *Int. J. Fract.* **42**, 21-40 (1990).
- [35] V. Yamakov, D. Wolf, S. R. Phillpot, A. K. Mukharjee and H. Gleiter, *Nature Materials* **1**, 1 (2002)
- [36] V. Yamakov, D. Wolf, S. R. Phillpot, A. K. Mukharjee and H. Gleiter, *Nature Materials* **3**, 43 (2002)
- [37] V. Stoilov, S. Tavoosfard, *Proceedings of European Atelier for Computational Sciences and Engineering, International Conference on CAE and Computational Technologies for Industry*, In Press, October 5-8, Lecce, Italy (2005).
- [38] D. Raabe, *Computational Material science*, Wiley-VCH, Ch. 7, 87-109 (1998)
- [39] J. M. Haile, *Molecular Dynamics Simulation*, Ch. 1, 1-50, Braun-Brum Field. Inc. New York, (1992)
- [40] [http://en.wikipedia.org/wiki/Hamiltonian\\_mechanics](http://en.wikipedia.org/wiki/Hamiltonian_mechanics), (2006)
- [41] K. Albe, J. Nord and K. H. Nordlund, *MEAM Workshop*, Eindhoven, (2002)
- [42] R. Komanduri, and L. M. Raff, *Proc. Instn. Mech. Engrs.*, **215**, 1639, (2001).
- [43] L. Verlet, *Phys. Rev.* **159**, 98, (1967)
- [44] D. Rapaport, *The Art of Molecular Dynamics Simulation - 2nd edn.*, Ch. 2, 2-44, Cambridge University Press (2004)
- [45] S. M. Foiles, M. I. Baskes and M. S. Daw, *Phys. Rev. B* **33**, 7983 (1986)
- [46] E. Clementi and C. Roetti. *At. Data Nucl. Data Tables*, **14**, 177 (1974)
- [47] J. H. Rose, J. R. Smith, F. Guinea and J. Ferrante, *Phys. Rev. B* **29**, 2963 (1984)
- [48] M. I. Baskes, *Mater. Chem. Phys.* **50**, 152-158 (1997)
- [49] M.D. Dighe, A.M. Gokhale, *Scripta Mater.* **37**, 1435–1440 (1997).
- [50] A.M. Samuel, F.H Samuel, *Metall. Mater. Trans.* **26A**, 2359–2372 (1995).

- [51] M.F Horstemeyer, M.I. Baskes, *J. Engng. Mater. Tech.* **121**, 114–119 (1999).
- [52] V. Tvergaard, J.W Hutchinson, *J. Mech. Phys. Solids* **40**, 1377–1397 (1992).
- [53] Y.T. Cheng and C.M Cheng, *Materials Science and Engineering Reports*, **44**, 91-149 (2004).
- [54] E. Buckingham, *Phys. Rev*, **4**, 345 (1914).
- [55] J. H Perry, *Trans. Am. Inst. Chem. Engrs.*, **40**, 251 (1944).
- [56] H. Yoshizawa, P. McGuiggan, and J. Israelachvili, *Science* **259**, 1305 (1993).
- [57] B. Li, P.C. Clapp, J.A. Rifkin and X.M. Zhang, *Journal of App. Phys.*,**90**, 3090 (2001).
- [58] U. Landman, W. D. Luedtke, and E. M. Ringer, *Wear* **153**, 3 (1992).
- [59] F. P. Bowden and D. Tabor, *Friction: An Introduction to Tribology*, Anchor/Doubleday, Garden City, NY, (1973).
- [60] B. L. Hammond, William A., Jr. Lester, Peter J. Reynolds, *Monte Carlo Methods in Ab Initio Quantum Chemistry*, Ch. 1, 1-45, World Scientific Pub. Co. (1994)
- [61] B.-J. Lee, J.-H. Shim, and M. I. Baskes, *Phys. Rev. B* **68**, 144112 (2003)

## VITA AUCTORIS

Levent Inci was born in Ankara, Turkey on January 3, 1975. He graduated from Ankara Gazi High School in 1992. He attended the Middle East Technical University where he obtained a B. Sc. in Physics in 2000 with a GPA 3.39. He entered the M.Sc. program in Physics at the University of Windsor in the fall of 2001 and graduated in the spring 2004. He is currently enrolled M. A. Sc. program at Engineering Materials of University of Windsor and expects to graduate in the summer of 2006

